Characterization and Mathematical Modeling of the Structure of Canadian Crude Asphalt binders by X-ray Diffraction

By

Ibrahim Abdulkarim Futheiz

A Thesis submitted to School of Graduate Studies in Partial fulfillment of the Requirements for the degree of

M.Eng.

Faculty of Engineering and Applied Science
Memorial University of Newfoundland

Sep 2017

St. John's, Newfoundland, Canada

Abstract

Eight samples of asphalt binder were retrieved from the provinces of Ontario and Alberta, Canada. Then they were pre-processed in thin film (1mm) on glass slides. X-ray diffraction (XRD) is used to perform profile fits, aromaticity and crystallite parameters in asphalt binder samples, and patterns were gotten by employing monochromatic Cu-K-a radiation (40kV and 40mA) using a Rigaku DMax 2200V-PC. Additionally, profile fitting was carried out by applying Pearson VII and Pseudo-Voigt functions from 5° to 35° as well as 60° to 110°= 2θ. The broadening of the diffraction line was simulated and analyzed using X-ray thin film. Outcome indicated a notable relationship between Pearson VII, Pseudo-Voigt, and Generalized Fermi Function (GFF). X-ray line broadening experiments using either the integral or full width at half maximum (FWHM) from diffraction lines are employed in order to simulate X-ray line profiles that emerged from the samples. For researchers as well as workers in the field, issues such as rutting of asphalt pavements in hot environments and cracking in cold ones are issues that not only persist but remain unresolved. Therefore, with the aim of enhancing asphalt pavement performance, it is worth examining compositional and structural characteristics in binders on a microscopic level.

.

Acknowledgements

First and foremost, I am grateful to Allah for the good health and well-being that were necessary to complete this research.

I would like to express my sincere gratitude and thanks to my supervisors, Dr. J. Shirokoff and Prof J. C. Lewis for the continuous support they provided for my MSc studies and related research, for their patience, motivation, immense knowledge and most importantly for their friendship. Their mentorship and guidance were invaluable.

I am also grateful to my parents and all my family members for the constant encouragement, support and attention they provided.

I would also like to express my gratitude to my friends, colleagues and everyone who directly or indirectly have lent their hands to this project.

I would like to gratefully acknowledge Ministry of Higher Education of Libya, which provided the scholarship that made continuing my Master's degree possible.

Table of Contents

List of Figures

Abbreviations

^{13}C NMR	Carbon-13 Nuclear Magnetic Resonance
^{1}H NMR	solution ^{1}H nuclear magnetic resonance
AASHTO	American Association of State Highway and Transportation
ASTM	American Society for Testing and Materials
BBR	Bending Beam Rheometer
CGSB	Canadian General Standards Board
CMA	Cold Mix Asphalt
DLCA	Diffusion-limited cluster aggregation
DSR	Dynamic Shear Rheometer
DTT	Direct Tension Test
FT-IR	Fourier Transfer-Infra Red
FWHM	Full width at half maximum of profile
GC-MS	Gas Chromatography-Mass Spectrometry
GFF	Generalized Fermi Function
HDM	Hydrodemetallization
HMA	Hot Mix Asphalt

HRTEM	high resolution transmission electron microscopy
IS	Infrared Spectroscopy
LDMS	laser desorption mass spectrometry
MALDI	Matrix-Assisted Laser Desorption/Ionization
MS	Mass Spectroscopy
NMP	*N*-methyl-2-pyrrolidone
NMR	Nuclear Magnetic Resonance
P	Pearson VII
PAV	Pressure Aging Vessel
PG	Performance Grade
RFCC	Residue Fluid Catalytic Cracking
RLCA	on reaction-limited cluster aggregation
SANS	Small Angle Neutron Scattering
SARA	Saturates, Aromatics, Resins and Asphaltenes
SAXS	Small Angle X-ray Scattering
SEM	scanning electron microscopy
SHRP	Strategic Highway Research Program
SMA	Specially Modified Asphalt

STEM	scanning transmission electron microscopy
STM	scanning tunneling microscopy
TFOT	Thin Film Oven Test
UV_F	Ultraviolet Fluorescence
UV-A	Ultraviolet Absorption
UV-vis	Ultraviolet-visible spectrophotometry
V	Pseudo-Voigt
VPO	Vapor Pressure Osmometry
WMA	Warm Mix Asphalt
XPS	X-ray Photoelectric Spectroscopy
XRD	X-ray diffraction

CHAPTER 1: INTRODUCTION TO HEAVY OIL AND ASPHALTENES

As the global supply of light, sweet crude is exhausted, refinery feedstocks are exceedingly shifting towards heavy conventional and unconventional crude. Highly viscous crudes, such as bitumen, are rapidly displacing light ends on the global market. Lighter crude oil has a low viscosity, low heteroatom content, contains a high percentage of desirable low molecular weight hydrocarbons and therefore, is more expensive. High gravity, high boiling, low solubility and heteroatom-rich, heavy feeds introduce enormous technical processing challenges. First, compounds that compose heavy crude are higher in molecular weight and heteroatom content than light crudes. Heteroatoms are organic compounds of nitrogen, oxygen and sulfur and trace metals such as nickel, vanadium, iron and copper that are responsible for a multitude of problems encountered throughout oil production and refining. Second, heavy crude oil is more viscous than light crude oil and therefore has a greater resistance to flow, requiring additional measures for transporting oil to a refinery. Because of the wide range of chemical moieties present in crude oil, a vast number of techniques determine processing techniques for different feeds. Understanding the composition, chemical and physical properties of petroleum, heavy oil and bitumen is paramount to meet future energy needs.

1.1 Asphaltenes

Petroleum asphaltenes (or simply “asphaltenes”) is the by-product of crude oil treated in paraffinic hydrocarbon solids heated to a low boil. Asphaltenes are characterized as being dry,

thick, black-brown in color (Altgelt, 1993), (Speight, 2001) and dissolvable in liquids such as benzene and toluene. They cannot, however, be dissolved by non-polar hydrocarbon solvents like n-heptane and n-pentane. Deasphaltened oil, or the so-called maltene fraction, describes the portion of crude oil that is dissolvable in paraffinic solvents (Altgelt, 1993). Asphaltenes are traditionally hard to chemically treat (because of their refractory qualities as well as trace metal concentrations and heterocompounds in their composition), but they still must be separated from bitumen and heavy oil (Sheu, 2002).

1.1.1 Asphaltene structure

According to standard Carbon-13 Nuclear Magnetic Resonance (^{13}C NMR) techniques, the breakdown of asphaltene carbon can be described as roughly 50% aromatic and 50% saturated, though slightly more aromatic than saturated (Boduszynski, 1987). Furthermore, asphaltene aromatic carbon is pericondensed rather than catacondensed (Calemma, Rausa, 1998). Figure 1.1 illustrates pericondensed and catacondensed structures. As can be seen, pericondensed rings (also known as pericyclic structures) comprise the base structures of asphaltene. This is due to their having abundant aromatic sextet carbon rather than isolated double-bond carbons, the latter which are known to be less stable (Herod and Bartle, 2007). The diameter of asphaltene's fused aromatic core measures around 10**Å**, or approximately half a dozen fused aromatic rings (Zajac et al., 1994).

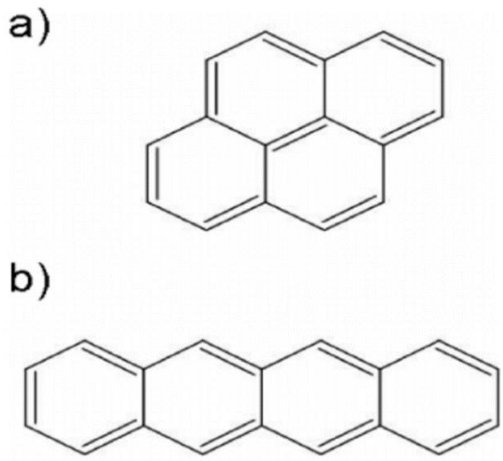

Figure 0-1: Structure of Condensed Aromatic Ring Systems (A) and Pericondensed Structure (B), (Durand et al., 2010).

1.1.2 Asphaltene properties

Among the many definitions of asphaltenes provided over the previous decades, Speight (1999) highlighted asphaltenes as that portion which has been removed from petroleum or crude oil by adding hydrocarbon solvents (e.g., n-heptane) to the mix.

Table 1.1: Elemental Composition of Asphalt from World Sources (Speight, 1999).

Source	Composition (wt.%)					Atomic Ratios			
	C	H	N	O	S	H/C	N/C	O/C	S/C
Canada	79.0	8.0	1.0	3.9	8.1	1.21	0.0011	0.037	0.038
Iran	83.7	7.8	1.7	1.0	5.8	1.19	0.017	0.009	0.026
Iraq	80.6	7.7	0.8	0.3	9.7	1.15	0.009	0.003	0.045
Kuwait	82.2	8.0	1.7	0.6	7.6	1.17	0.017	0.005	0.035
Mexico	81.4	8.0	0.6	1.7	8.3	1.18	0.006	0.016	0.038
Sicily	81.7	8.8	1.5	1.8	6.3	1.29	0.016	0.017	0.029
USA	84.5	7.4	0.8	1.7	5.6	1.05	0.008	0.015	0.025
Venezuela	84.2	7.9	1.6	1.7	4.5	1.13	0.020	0.014	0.020

Table 1.1 shows asphaltene as a chemical composition. Resins, meanwhile, can be highlighted as that portion in asphalt-free oil that comprises a large part of substances such as alumina and silica and may be separated only through the use of a solvent mixture involving, for instance, toluene and methanol. Asphaltenes represent aromatic heterocompounds that include aliphatic substitutions and hence comprise crude oil's polar-most part. (Koots et al., 1975) believed that resins' correlation to asphaltenes was the major factor of its degree of solubility in crude oil.

1.1.3 Asphaltene characteristics

Asphaltenes occur across a broad range of natural settings as well as in different types of forms, including dispersed organic matters in sediments and bitumen. As mentioned above, there are numerous definitions of asphaltene, but they all generally refer to "heavy organics from carbonaceous sources such as petroleum, coal, and shale oil that [are] insoluble in low molecular weight n-paraffins and soluble in aromatic solvents such as benzene and toluene" (Mansoori et al., 1988). Figure 1.2 illustrates asphalt as "operational material" that is solubility-dependent. By applying the Yen-Mullins approach, Mullins (2010) sees asphaltenes as being dependent on molecular weight analyses of various hierarchial stages.

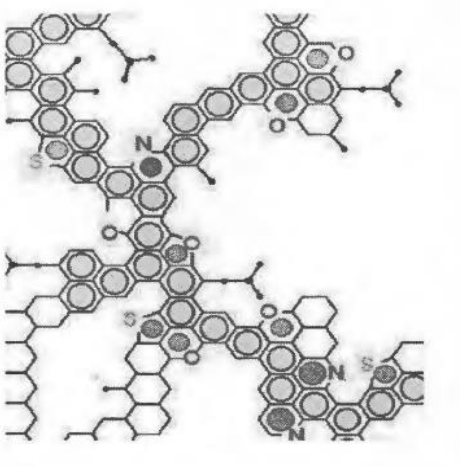

Figure 0-2: Modified Molecular Structure of Asphaltene (Altamirano et al., 1986).

As illustrated in Figure 1.3, the solubility curves show how soluble fractions change during solivation to create a precipitate fraction. This occurs during their interaction within the solution. From this, we can see that the precipitate asphaltenes are insoluble by a higher toluene fraction than entire asphaltenes. In fact, in their study, Keith et al. (2003) demonstrated how a whole or precipitate is far less soluble than a soluble fraction.

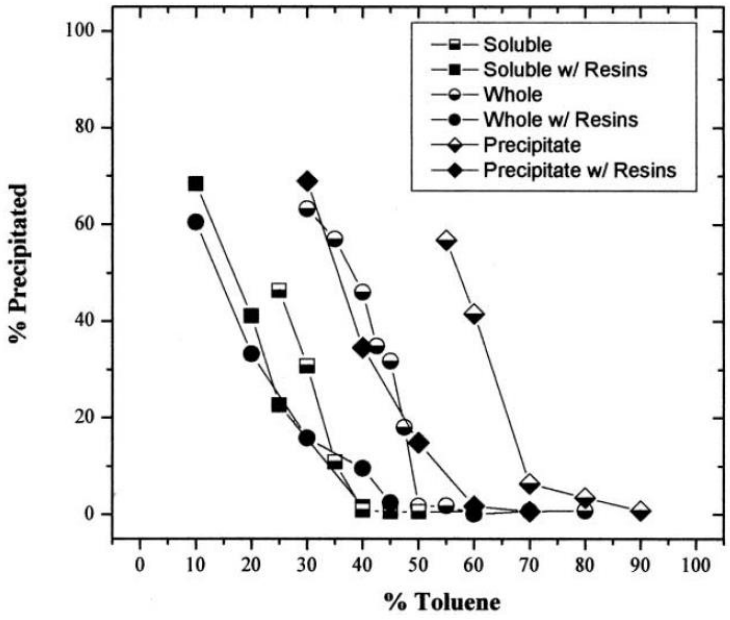

Figure 0-3: Modified Figure of Solubility (Keith, 2003).

Thus, while asphaltenes may remain plagued by numerous partial definitions because of the many types and structures of crude oil molecules, researchers are mostly in agreement over the fact that asphaltenes always have the following: alicyclic moieties, polynuclear aromatics, and aliphatics, along with elements like sulfur, nitrogen, oxygen, and vanadium. Furthermore, asphaltenes make up the largest portion of compounds which include resins and aromatics. The most recent definition of asphaltenes was offered by Mullins (2011), who combined several different approaches to develop a modified Yen model.

1.1.4 Asphalt types

In order to obtain the best possible performance according to construction designs, it is essential to use the right asphalt mixture for the right conditions. So, for instance, the specifications for highways must take into account high traffic loads as well as weather conditions that can range from hot to cold and dry to wet, sometimes even within a single day. Under such conditions, the appropriate mixture must be able to endure intense levels of deformation and stiffness while at the same time be flexible and strong enough not to crack under the myriad of different pressures that can occur on a typical roadway. These factors form the basis for pavement durability.

During the mixing process, it is essential for the chemical mixers to have a sound grasp of all the different asphalt categories in order to develop an appropriate mix to satisfy the requirements for durability and performance. A few of the main asphalt types are as follows:

1. Cold Mix Asphalt (CMA): In this asphalt type, no heating of the aggregate is required. This is caused by the presence of a bitumen that breaks under compaction or mixing. Post-break, the aggregate is coated by the emulsion, increasing strength over a period of

time. CMA is usually used only in rural roads that rarely if ever have to handle heavy traffic loads.

2. Warm Mix Asphalt (WMA): In this asphalt type, the mix is made using heat ranging between 20° C and 40° C. Unlike CMA, WMA is intended for use in heavier trafficked roads and thus must not only have the stiffness factor but also be resistant to deformation and sufficiently flexible and strong to withstand cracking.
3. Hot Mix Asphalt (HMA): In this asphalt type, the mix is usually produced at an extreme temperature range (150° C to 190° C) and is intended for use on roads with heavy traffic as well as heavy vehicles.

There are two basic categories of asphalt – petroleum and natural. Petroleum asphalts develop as colloidally-dispersed hydrocarbon residue in the refinery process of crude petroleum distillation, while natural asphalts develop in layers over the course of hundreds of thousands of years. Pavement used in roads and residential properties is mostly made from petroleum crude asphalt. Portland cement concrete is used to make rigid pavements, whereas asphalt is used to make flexible pavement. Failures in flexible pavement can arise due to a wide range of issues, chief among which are alterations in refining processes or crude sources. Failures can also arise due to inaccurate specifications, mixing designs and additive usage as well as increased traffic volume involving heavy vehicles. The literature review section of this work will provide a more in-depth discussion on aspects of asphalt pavement failures, including the XRD analysis approach, flaws in the design mixture, and inappropriate application of aggregates in asphalt binders.

1.1.4.1 Natural Asphalt

As an organic compound, natural asphalt and oxygen interact (oxidation), resulting in alterations to the material's composition and molecular structure. During the interaction, the natural asphalt becomes deprived of its "stickability" factor. Oxidation generally happens faster in high temperatures rather than in lower ones. The primary use of natural asphalts nowadays is for bitumen content in asphalt mixes as well as for improving deformation resistance and surface performance.

1.1.4.2 Petroleum Asphaltene

Petroleum asphaltene is a specific class of petroleum liquids that is, according to Sheu (2002), not only the most refractory but also generally the heaviest of all oil components. Furthermore, the properties of asphaltene encompass both structure and molecular weight (Sheu, 2002).

Boussingault (1931) first identified asphaltene in the early 1930s, distinguishing it from an ether-insoluble fraction of asphalt. Nellensteyn (1933) believed asphaltenes to be high molecular hydrocarbons that create a colloidal system which becomes adsorbed by surface components. Since that time, several researchers have strived to better define the molecular

weight, structure, etc., of asphaltene, as they contend that it is an important base in numerous applications and also improves the production efficiency for petroleum products.

1.1.4.3 Asphalt Cement

Although it can be composed of a variety of substances, asphalt cement is usually made primarily of bitumen, resins, and absorbed gas. The distillation process for this type of asphalt may be naturally occurring and lead to the formation of asphalt lakes, or it may occur during the petroleum refinement phase. Moreover, the distillation process and type of crude are instrumental in defining both the content and the fractional proportions of the various primary and secondary compounds found in asphalt cement.

Asphalt cement typically undergoes physical and chemical alterations over the course of time, mainly due to the different reactions of its contents. The most common alteration is a stiffening that occurs as the asphalt ages (Richard, 2007). In order to create different asphalt cement grades, heavy residues are further processed during the refining process. Asphalt cement is currently marketed as “Performance Grade” (PG) binders and is used according to the traffic load and weather conditions of the intended locations.

1.2 Performance Grade (PG)

In the performance grade (PG) or binder-grading system, certain specifications are related to the physical properties in the actual field performance of asphalt binders. In PG testing, factors such as heat, cold, age, and traffic/vehicular loads are used. So, for instance, a PG binder

specification rated as PG 67-31 relays the following information: “67” indicates the highest temperature (in Celsius) the pavement can handle, while “-31” indicates the lowest temperature (again, in Celsius) under which the pavement performs well. Furthermore, PG 67-31 asphalt can withstand thermal cracking in frigid temperatures as low as -31 °C, while also mitigating the rutting of pavement during the summer when pavement temperatures can exceed 67 °C. Additionally, PG binder specs stipulate that asphalt must include polymers or similarly acting chemicals to satisfy performance standards. Introducing modifiers to the mix can also prove detrimental, in that it can lead to hardening and a reduction in temperature susceptibility, but it is twice as cheap as unmodified asphalts (Hesp, 2008). Overall, asphalt usually contributes approximately 6% of the HMA, but its cost can exceed 30% of HMA pavement price (Monismith, 1985).

1.3 Asphalt Binders and Asphaltene

The binding agent responsible for combining the aggregate in HMA is called an asphalt binder. As mentioned previously, asphaltene is strongly resistant to cracking and therefore decreases the production of petroleum in the distilling phase. However, having a large proportion of asphaltene in asphalt is highly preferable in road paving, particularly in roads that are heavily trafficked, take heavy loads, and endure relatively extreme temperature and weather condition changes.

1.4 Measuring X-ray Diffraction (XRD)

The main point of interaction for X-rays and electrons is atoms. However, during collisions between X-ray photons and electrons, a portion of the incident beam photons are deflected. If this occurs, the process by which the deflected X-rays retain their *hv* energy is referred to as 'elastic' (or Thompson) scattering. In this process, momentum rather than energy is transferred. The X-rays which are scattered are then used for measurement readings in diffraction experiments, as these rays retain important data regarding electron distribution which occurs in the specimen's thin film.

In contrast, in Compton scattering, which is an inelastic scattering process, there is a transfer of energy from X-rays to the electrons such that the scattered X-rays and incident X-rays exhibit different wavelengths. The diffracted waves emanating from the diverse atoms have a tendency to interfere one with the other, and the intensity distribution undergoes significant modulations from their rigorous interactions. This is an effective way to detect material composition.

1.5 X-Ray Scattering

When there is a marked distance separating detector and sample, along with an extremely collimated beam, precise measurements (scattering angle < 6°) can be taken of X-rays that are only slightly scattered. Bragg's Law asserts that because length, *d*, stands inversely proportional to the sample's scattering angle, smaller angles indicate larger features (as explained in section 2.1.1). The Yen model, which states that atoms periodically rearrange themselves into a cubic structure featuring four peaks, provides one option for our analysis pertaining to the data collected on asphalt binders. As well, we can look at the Yen-Mullins model for analyzing XRD (see section 2.1.2).

1.6 Thesis Statement

As briefly touched on above, asphaltenes can cause major issues during the process of petroleum production. Specifically, they cause problems all the way from the oil field to the refinery by introducing unwanted deposits into the processing infrastructure. Figure 1.4 illustrates a typical asphaltene deposit in a pipeline. Issues can include clogging of flowlines, wells, and refinery infrastructure, along with deposit formations underneath the well itself Mullins, O.C., et al., (2007).

Additionally, the presence of asphaltene can lead to problems on a molecular level. So, having an in-depth understanding of both the composition and factors affecting asphaltene is crucial not only for dealing with the substance but for predicting and, preferably, preventing asphaltene-related issues during the petroleum harvesting and refinement phases. In fact, asphaltene's physical and chemical features help point to the best approach to use for processing crude. Techniques based on molecular characterization highlight composition and molecular weight, and so are useful for determining the most optimal downstream processes. So, for instance, even though refineries extensively use catalysts, asphaltene molecules have a tendency to interfere with their functioning by deactivating them. This is particularly the case in instances of extreme heat and pressure, which are normal environments for asphaltene. How asphaltene acts in the transportation phase also should be factored into production decisions (McKenna, 2009).

Figure 0-4: An Asphaltene Deposit Formed on the Inside of a Pipeline in a Refinery (Mckenna, 2009).

1.6.1 Asphaltene aggregation.

In dilute toluene solutions, asphaltenes can self-associate and develop aggregates when found in crude oil (Mullins, 2008). In order to grasp how asphaltenes will impact large-scale functioning of the processing phase, it is first necessary to be aware of the material's colloidal properties and aggregation propensities in low concentrations (e.g., reducing pressure can lead to the presence of asphaltene deposits in under-saturated crude). Moreover, introducing solvents at any point in the production phase might lead to asphaltenes precipitating out of the solution (De Boer, R. B., et al., 1995). It should also be noted that, in some instances, inaccurate readings of asphaltene's molecular weight are likely due to aggregation, as initial asphaltene self-association can happen during concentration amounts that are typically significantly lower than the techniques employed for molecular weight readings (Sheu, Maureen, et al., 1992).

1.6.2 Asphaltene molecular weight.

The molecular weight of asphaltenes has, for some time, been the preferred parameter for understanding and predicting the material's behavior (Sheu, 2002). The generally agreed-upon (but not without some dissent) formulation of asphaltene's molecular weight is less than 1 kDa (Mullins, 2008). The ongoing disputes regarding asphaltene's molecular weight has largely been caused by the material's propensity, at the molecular level, to self-associate and aggregate in ultra-low concentrations readings Mullins, Betancourt, et al (2007). More specifically, the disagreement among researchers regarding asphaltene's molecular can be traced to the application of analysis approaches that are ill-fitted to asphaltenes. A few of the most contentious methods are highlighted below.

Vapor Pressure Osmometry (VPO) functions at concentrations two orders of magnitude greater than asphaltene's aggregation onset (Mullins, 2008). As a result, VPO readings essentially measure the aggregate's weight rather than that of the monomer. Another approach is laser desorption and ionization/mass spectrometry (LDI/MS), but its variability coupled with high surface concentration has resulted in persistently erroneously high readings for asphaltene's molecular weight readings Trejo, (Ancheyta., et al, 2007). Similarly, gas phase aggregation measuring molecular weight by LDI/MS also gives erroneous data readings (Herod, Bartle., et al., 2007). Yet another contentious approach is size exclusion chromatography, as it consistently gives high molecular weights for asphaltene due to a range of issues, as follows. The main problem with this method is that chromatography columns cannot, by definition, be compatible with toluene, despite it being an optimal solvent for asphaltene. It is worth noting that we do not yet know the process by which asphaltene aggregation takes place in other solvent systems, other

than to know that asphaltene cannot be made fully soluble in them. Additional failed methods for measuring asphaltene's molecular weight include solvents like N-methyl pyrrolidinone, but they have been shown to incur flocculation of more than half of the asphaltene sample and thus cause erroneous readings (Mullins, 2008).

1.6.3 Fatigue and rutting

Fatigue and rutting of asphalt pavement are the main issues impacting its performance. Fatigue causes increasing longitudinal cracks that eventually lead alligator cracking (so-called due to its resemblance to alligator skin). Rutting refers to a type of pavement deformation that typically happens when the asphalt softens under excessive heat conditions (i.e., during summer weather or in wildfires). To mitigate both the onset and the effects of fatigue and rutting, there is a clear need to investigate the composition and structure of asphalt binder on a microscopic level.

1.6.3.1 Rutting:

The rutting of heavily trafficked roadways frequently occurs due to heavy use. In contrast, airport pavements very rarely rut, as aircraft traffic is relatively light and infrequent compared to roadway loads. Rutting can still occur at airport runways, but then it is usually caused either by extreme weather conditions over time, unsuitable pavement mixtures, or both. Another cause of surface rutting on roadways is the failure of HMA layers, while subgrade rutting can happen if a subgrade cannot support the required loads. The rutting of roadways is illustrated in Figures 1.5 and 1.6.

Several researchers have looked further into possible reasons for rutting. For instance, McGennis et al. (1994) discovered that certain impurities in the binder (i.e., the percentage of mineral filler present or the HMA film thickness) had a significant impact on mixture rutting (McGennis et al. 1994), while Christensen and Bonaquist (2002) discovered that the shear strength of HMA mixture can be enhanced as the asphalt binder stiffens.

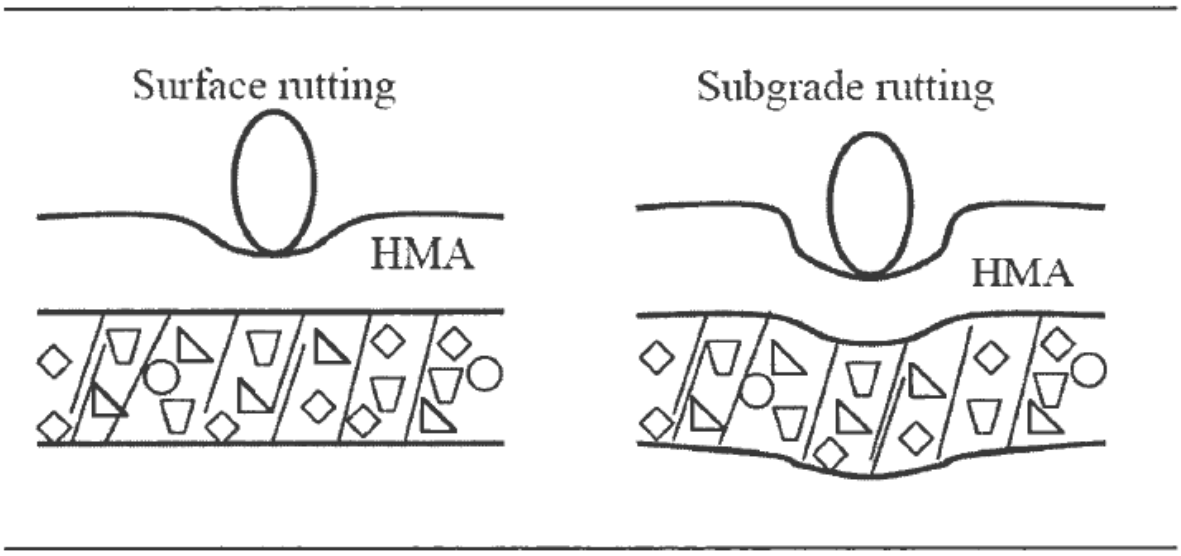

Figure 0-5: Sketch of Surface Cross-Section and Subgrade Rutting (Gebresellasie, 2012).

Figure 0-6: Rutted Road Surface Occurs with Too Soft Asphalt Binders (Gotame, 2016).

1.6.3.2 Fatigue Cracking

Fatigue cracking is another common condition of pavement that occurs over time. As illustrated in Figure 1.7, fatigue cracking is primarily due to heavy traffic causing ongoing deterioration in the pavement's internal structure, ultimately lessening the HMA load-bearing capacity. A typical manifestation is alligator cracks, characterized by distinct alligator skin-like patterns of interconnected fissures. According to (Galal and White, 2001), this type of deterioration is exacerbated by extreme low temperatures and general aging of the pavement, but the main causes are improper mixture as well as poor design and overloading (Galal & White, 2001).

Figure 0-7: Fatigue Cracked Road Surface Due to too Hard Asphalt Binders Being Used (Galal and White, 2001).

(Harvey et al., 1995) reported that, according to their investigations, an effective way to lengthen the life of HMA mixes was to increase the availability of the asphalt binder while reducing air void content. Higher binder content in the mix made the binder film thicker while also placing fewer strains on the binder. Furthermore, Harvey et al. (1995) also asserted that reducing the air void content resulted in the subsequent stiffening and strengthening of the HMA and a lowering of stress levels in the binder and aggregate. As well, the reduced air void content created a smoother binder aggregate structure and thus reduced stress concentrations at critical solid air interfaces (Harvey et al., 1995). Mixtures that feature high binder content and low air void content show longer fatigue life.

1.7 The objective of this research.

In this research, different samples of asphalt binders collected from different parts of Canada were tested in the laboratory for aging and investigating the composition of the aggregates at the microscope level.

The asphalt binders are aged for a week and the x-ray diffraction profiles are collected and analyzed accordingly from the Rigaku diffractometer, by the aid of advanced mathematical functions of Pearson-VII and Pseudo-Voigt and Generalized Fermi Function (GFF).

The XRD data show it is possible to differentiate asphalts of different standards and classifications through peak centroid and other parameters (such as aromaticity and crystallite) are considered.

Chapter 2: Literature Review

2.1 Asphaltene Characterizations

In order to gain an in-depth understanding of the nature and structure of asphaltenes, researchers must perform a variety of characterization analyses. There are many different types of characterization techniques, ranging from the simple to the complicated, and utilizing equipment that likewise ranges from cheap and easy-to-use to costly and complex. In this section, we will discuss a few of the analyses that have been applied to asphaltene to get a better grasp of the material's molecular structure.

2.1.1 Infrared Spectroscopy

During the initial processing phase, crude oil can be fractionated in a column to obtain different types of fractions. So, for instance, in aromatic distribution, vacuum gas oil contains structures exhibiting up to three polyaromatic cycles, while vacuum residues can have up to six (Merdrignac & Espinat, 2007). The general rule of thumb is: the higher the cut's boiling point, the higher the aromatic content (Merdrignac & Espinat, 2007). Although Gas Chromatography-Mass Spectrometry (GC-MS) can be used to analyze multi-ring cycles, the focus here is on discerning how much material left behind constitutes nonvolatile residue. This is not always easy to accurately ascertain. In fact, Pillon (2001) believed that only a portion of the sample is actually volatile when asphaltenes are characterized by GC-MS. Pillon (2001) also discovered that less than three-quarters (74 wt%) of the sample underwent adequate analysis.

Over the years, numerous researchers performed analyses on asphaltene using a variety of methods, including infrared spectroscopy (IS) and diffuse reflectance infrared (DR-IR)

(Elsharkawy et al., 2005); (Aske et al., 2001); (Seidl et al., 2004); (Buenrostro-Gonzalez et al., 2001b, 2002); (Miura et al., 2001). More recently, (Coelho and colleagues, 2007) showed that a linear correlation existed within infrared (IR) intensities of symmetric and asymmetric aromatic hydrogens for methyl substituted arenas (namely, in the 2,900 to 3,100 cm^{-1} range) as well as for out-of-plane deformation (again, namely in the 700 to 900 cm^{-1} range) (Coelho et al., 2007). Table 2.1 shows their observations in summary format. Furthermore, a Fourier Transfer-Infra Red (FT-IR) analysis, which tests aromatic rings, points to the existence of several different groups of asphaltenes, including -OH, $-CH_3$, $-CH_2CH_3$, with hydrogen-bonded phenols existing at between 3,100 to 3,300 cm^{-1} (Elsharkawy et al., 2005). When the sample includes sulfur but bands do not appear around 2,500 cm^{-1}, they could exist instead as thioether, thiophene, or a -C-S-C- form of structure (Elsharkawy et al., 2005).

Table 2.1: Functional Groups Present in Asphaltenes by Infrared Spectroscopy (Ancheyeta Et Al., 2010).

Functional group	Absorption Band (cm^{-1})
-OH, -NH stretch	3600–3300
OH contributing to different hydrogen bonds	
OH-π hydrogen bond	3530
Self-associated *n*-mers (n>3)	3400
OH-ether O hydrogen bonds	3280
Tightly bound cyclic OH tetramers	3150
OH-N (acid/base structures)	2940
COOH dimmers	2640
Aromatic hydrogen	3050
Aliphatic hydrogen	2993, 2920
-CH, $-CH_2$, $-CH_3$ stretching regions	3000–2800
-SH stretching regions	~2500
C=O	1800–1600
Keton (C=O stretching)	1735–1705
Aldehide (C=O stretching)	1740–1730
Conjugated C=C	1650, 1600
Aromatic C=C	1602
-CH, $-CH_2$, $-CH_3$ bending regions	1450–1375
Methyl bending vibrations	1377
Ether or ester group	1306

Ester linkage	1032
Sulfoxide groups	1030
C-S, C-O, C-N stretching regions	~1000
Aromatic C-H bending	900–700
Two adjacent H	810
1 adjacent H	900–860
2 adjacent H	860–800
3 adjacent H	810–750
4 adjacent H	770–735
5 adjacent H	710–690 (or 770–730)
Alkyl chain longer than four methylene groups	725–720

In examining asphaltene's infrared spectra, we can clearly see evidence of hydrocarbon bands. Specifically, both symmetrical and asymmetrical stretchings on C-H aromatics bounds υCH_{ar} are evident from 3,057 to 3,000 cm^{-1}, and both symmetrical and asymmetrical stretchings on C- H aliphatic bounds δCH3-CH2 from 2,922 to 2,852 cm^{-1} can also be seen. As well, the following can also be seen: Deformation bands of methyl δCH3 from 1,375 to 1,365 cm^{-1}; methylene γCH3-CH2 from 1,460 to 1,440 cm^{-1}; aromatic bending of mono-substituted γCH_{AR1} from 870 to 860 cm^{-1}; di- and tri-substituted $\gamma CH_{AR2,3}$ from 810 to 800 cm^{-1}; and tetra-substituted δCH_{AR4} from 760 to 740 cm^{-1}. Additionally, there are stretching within four methyl groups, namely $\gamma CH_{2,n}$ from 727 to 722 cm^{-1} (Buenrostro-Gonzalez et al., 2002; (Langhoff et al., 1998); Christy et al., 1989; Conley, 1972; Dyer, 1965). In samples lower than 0.01 wt% of concentration, signals at 3,585 cm^{-1} related to oxygenated groups, while aromatic C=C stretching occurs in signals from 1,609 to 1,580 cm^{-1}. Borrego et al. (1996) found signals at 1,600 cm^{-1}, giving them identical stretchings.

(Wilt and colleagues, 1998) stated that FT-IR can be applied to various groups within asphaltenes and can also quantify how much asphaltene exists in crude. In fact, they applied a partial least-squares model (an r^2 value of 0.95 and a standard error of 0.92 wt%) to determine in

advance how much asphaltene could exist in 42 different types of crude (Wilt et al., 1998). Although the research was carried out nearly 20 years ago, the approach gives faster analysis results and does not require the use of solvents. In this regard, it is still as useful and accurate as more recent laboratory procedures.

2.1.2 Asphaltene Molecular Weight

There is currently very little agreement among scientists and other researchers about the molecular weight of asphaltenes. The reason for the disagreement is the general distrust of the techniques used to measure the weight as well as the analysis conditions (i.e., using temperature or solvents). A few decades ago, (Vellut and colleagues, 1998) carried out a comprehensive review of the various approaches used throughout the 20^{th} century to measure the molecular weight of macromolecules (Vellut et al., 1998). The researchers divided the techniques into the three categories of thermodynamic colligative, separation, and spectroscopic methods. In the following sub-sections, a review of results of some other researchers regarding asphaltene's molecular weight analyzed by the vapor pressure osmometry (VPO) method. We also look at mass spectroscopy (MS).

2.1.2.1 Vapor Pressure Osmometry (VPO)

As indicated in the previous sections, the actual molecular weight of asphaltenes remains somewhat controversial due to disagreements over methods used to measure it. Currently, vapor pressure osmometry (VPO) is one of the most popular approaches, as it enables the setting of an absolute value in relation to the number-average molecular weight. In using VPO, the values measured for both non-polar compounds and low molecular weight substances are considered to

be highly reliable. In fact, VPO values reflect those of mass spectroscopy during analysis of crude oils and resins (Yang & Eser, 1999).

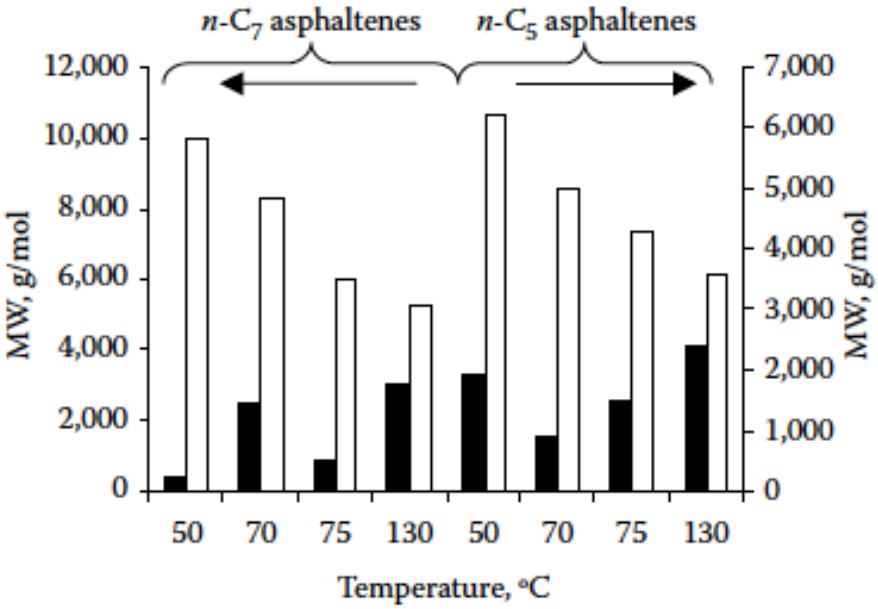

Figure 2-1: Estimated Molecular Weight of Monomer and Aggregate Asphaltenes in Two Different Solvents: (■) Monomer (□) Aggregate (Yarranton, 2000).

Furthermore, conflicting values emerge when using different solvents to analyze the asphaltenes. Applying the VPO approach, Acevedo and colleagues (1992a) found values ranging between 1,500 and 12,300 g/mol when using the solvent pyridine. For Yarranton and colleagues (2000), the molecular weight values of Athabasca and Cold Lake bitumen asphaltenes widely varied between 4,000 and 10,000 g/mol, and the molecular weight of an asphaltene monomer under VPO was around 1,800 g/mol. The monomer value was derived by considering the interception of a measured molecular weight compared to asphaltenes concentration, and then extrapolated at a concentration of zero. Research indicates that extrapolation may only occur at low concentration of asphaltenes (e.g., 3 g/L or lower) (Yarranton et al., 2000).

In Figure 2.1, we can see how asphaltene's molecular weight is extracted by using n-pentane and n-heptane as part of the monomeric. The figure shows VPO-obtained measured values on Athabasca asphaltenes, using as solvents 1, 2-dichlorobenzene as well as toluene. According to the temperature and composition of the analysis parameters, asphaltenes can exist in aggregates of up to six monomers. Acevedo et al. (2005) performed analyses of asphaltenes via VPO. They used nitrobenzene at temperatures up to 100^0 C, altering the solution concentrations between 0 and 6 g/L. (Acevedo et al., 2005) found reasonably good correlation between VPO and mass spectrometry.

Speight (1987) believed that not only the degree of concentration, but also temperature, solvent type and polarity contributed to the outcome of the VPO method. In fact, Speight (1987) suggested that the only way to achieve accurate readings of asphaltene's molecular weight was to analyze samples using three concentrations and three temperatures. So, in a plot that featured molecular weight compared to concentration, the data obtained from the three temperature readings would be extrapolated at a concentration of zero concentration; meanwhile, the zero-concentration data at the three separate temperature readings would likewise be extrapolated under room temperature (Speight, 1994). A few decades earlier, Moschopedis et al. (1976) had suggested employing high temperatures (100 to 150° C) and nitrobenzene to ascertain asphaltenes molecular weight. When applying this latter approach, the readings showed low molecular weight; moreover, the results were in agreement with those gained by structural determinations of solution ^{1}H nuclear magnetic resonance (1H NMR) (Moschopedis et al., 1976).

There are both clear advantages and disadvantages to using VPO. The advantages are that VPO provides accurate molecular weight values for resins and lighter types of petroleum, and

that at extreme (hot) temperatures, the molecular weight remains reliable even with the application of a highly dissociating solvent. Using the VPO approach, there is also no correspondence to aggregate molecular weight.

The two main disadvantages in this method are solvent-related. The first is that the asphaltene molecular weight will actually be an aggregate molecular weight if the solvent proves to be inadequate. The second disadvantage is that the solvent usage restricts temperature increases in most types of equipment.

2.1.2.2 Mass Spectroscopy

One approach that has become popular in the petroleum industry over the past few decades is mass spectroscopy (MS). This strategy enables the molecular weight of asphaltenes and other materials to be distributed. Mass spectroscopy requires the use of non-fragmenting ionization methods. Domin et al. (1999) cautioned that the only way to get a reliable distribution of molecular weight using MS is by adhering to the following procedure: (1) vaporizing the molecule, and then (2) ionizing the m, being careful not to fragment them. This, however, can be difficult, given the polydispersity and complicated structure of asphaltenes. To mitigate this problem to a certain extent, laser desorption mass spectroscopy (LDMS) can understate the molecular weight values in samples that are complicated.

An alternative approach that uses MS is called matrix-assisted laser desorption/ionization, or MALDI for short. The MALDI technique utilizes a compound for its matrix. Karas and Hillenkamp (1988) debuted this approach in the late 1980s; since then, the strategy is being applied in polymers, biomacromolecules, and also petroleum fractions. Including a matrix reclassifies MALDI as a “soft” approach, as the matrix lessens through

dispersion any heat generated through the actions of the laser beam, after which it distributes, thus preventing sample fragmentation.

MALDI and SEC both enjoy reasonably good correspondence, according to Suelves et al. (2003). They discovered agreement ranging between 200 and 3,000 g/mol. The substances left out of SEC (equaling only 1 to 2 wt% of the entire sample) are unknown but, based on MALDI, would likely relate to samples measuring 3,000 to 10,000 g/mol. Materials that feature high molecular weight could serve as a nucleation center when using inadequate solvents to aggregate small molecules. Herod et al. (2000) provided a brief summary of considerations they saw as key concerns that must be dealt with if utilizing MALDI for molecular weight analysis. The four main issues are listed below:

1. Raising the voltage on ion-extraction leads to higher ionization, which then assists in the detection of materials that feature higher molecular weight.

2. Higher molecular weights are readily perceived upon removing the reflector, as this boosts the ability of the equipment (i.e., makes it more sensitive) to detect them.

3. Spectra signal-to-noise ratios become greater with every increase in co-added scans.

4. The molecular weight distribution can be affected by the composition of the materials in the matrix and samples, as well as by their combination.

According to (Merdrignac and colleagues, 2004), MALDI found molecular weights ranging from 100 to 1,000 g/mol in the molecular weight distribution of asphaltene fractions. Their results suggest that molecular weight is not solely determined by molecular fragmentation, but instead is impacted by polydispersity. Using a variety of temperatures, Seki and Kumata (2000) examined some spectra of asphaltenes from demetallized Kuwait atmospheric residue.

The LDMS (laser desorption mass spectroscopy) of asphaltenes derived from the feedstock, along with items tested at around 370 and 390° C, appeared to be broad and polydispersive. This pointed to conditions not being sufficiently harsh to prompt any major alterations to asphaltenes below 400° C. In such conditions, the asphaltenes showed a strong peak at m/z 1,100 and m/z 600 g/mol, potentially revealing the presence of compounds quite light in molecular weight.

In heat conditions exceeding 400° C, alterations became clearer. So, for instance, when the heat reached 410° C, the peak declined to less than m/z 1,000 g/mol. Then, at 430° C, the researchers saw non-identical twin peaks (Fig. 2.2), providing the following explanation: (1) the peaks come from a novel asphaltene fraction that developed as a result of hydrodemetallization (HDM) reactions; the peaks (2) were built by asphaltenes with only one aromatic skeleton, while the second peak comes from the asphaltenes' creation of two aromatic skeletons.

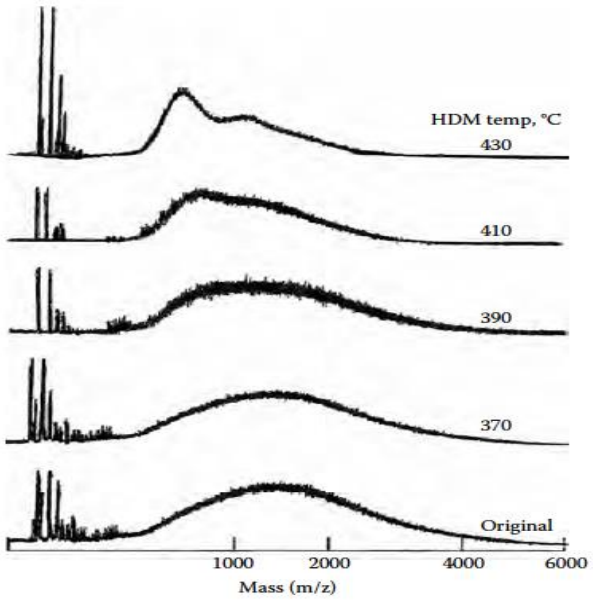

Figure 2-2: LDMS Spectra of Nonhydrotreated and Hydrotreated Asphaltenes (Seki and Kumata, 2000).

Figure 2.3 illustrates work done by Trejo et al. (2007), who investigated LDMS and MALDI spectra in Maya crude asphaltenes. Applying sinapinic acid as a matrix, maximum

ion count ranged from m/z 1,500 to m/z 2,000 g/mol when measured for LDMS, and m/z 2,000 g/mol when measured for MALDI. That the MALDI spectrum appears to be lacking in lower molecular weights might be the result of smaller asphaltene molecules evaporating.

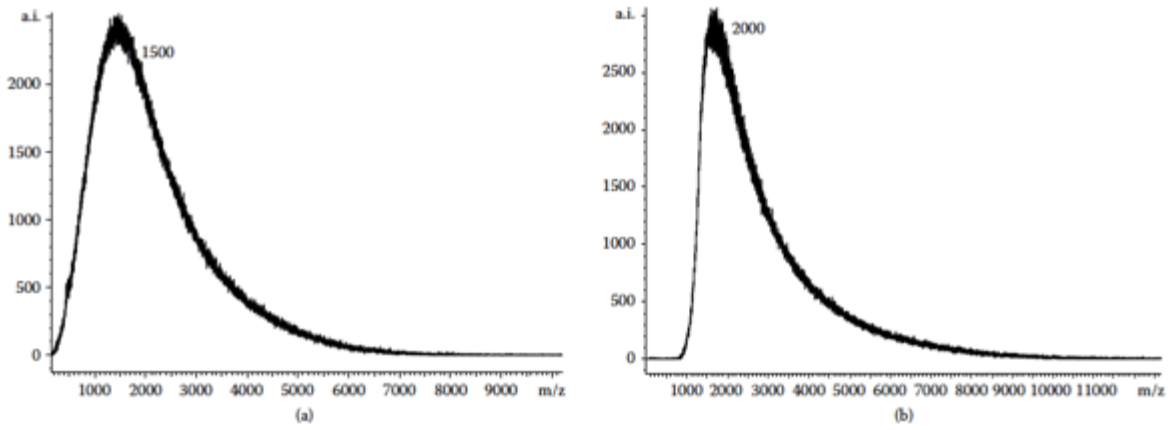

Figure 2-3: LDMS (A) And Maldi (B) Spectra Of Maya Crude Asphaltenes (Trejo et al., 2007).

2.1.3 Ultraviolet (UV) fluorescence

Guan and Zhu (2007) utilized FT-IR, Ultraviolet-visible spectrophotometry (UV-vis), and synchronous fluorescence spectrometry to investigate how aromatic rings are distributed in asphaltenes and resins in instances where their intense interactions are effected by hydrogen bonds. In using synchronous fluorescence spectrometry and UV absorption to locate the structures, Guan and Zhu (2007) found that asphaltenes and resins mainly differed only in relation to the number of conjugated aromatic rings. Specifically, asphaltenes have minimum 5 rings, while resins have maximum 4 in a conjugated aromatic unit, and both materials exhibit a peri-condensed structure (Guan & Zhu, 2007).

A few years earlier, Ascanius and colleagues (2004) investigated asphaltene's insoluble fraction in *N*-methyl-2-pyrrolidone (NMP), finding that it had very little fluorescence for the

wavelengths under investigation. Based on these results, Ascanius et al. (2007) determined that the approaches involving fluorescence and UV visible spectroscopy actually stopped short of analyzing whole asphaltenes, and that the apparent absence of fluorescence could be caused either by molecular interactions or the sample's structural make-up. The outcome of either condition would be strong red shifts and the dilution of any fluorescence present, both of which were noted by the researchers (Ascanius et al., 2007).

In asphaltene's insoluble fraction, the presence of aliphatic species was more pronounced, whereas in NMP's soluble fraction, the presence of aromatic structures was greater. However, Al-(Muhareb et al., 2007) noted that increasing the insolubility in NMP led to a subsequent increase in aromatic chromophores. Based on these observations, (Al-Muhareb et al., 2007) posited the insolubility of asphaltenes largest chromophores in NMP, despite their easy solubility in chloroform, but conditions which can be verified under UV fluorescence spectroscopy. Moreover, Al-Muhareb et al. (2007) indicated that the NMP insoluble fraction is likely part of aliphatic groups which are much larger. A few year earlier, Millan et al. (2005) discovered in their research that heptane-insoluble materials (such as asphaltene) exhibit only a weak fluorescence under UV-fluorescence, and that such an approach cannot detect materials that feature high mass and are therefore inappropriate (Millan et al., 2005). Meanwhile, Trejo et al. (2007) investigated UV fluorescence using asphaltenes derived from virgin Maya crude and applying NMP as a mobile phase. Figure 2.4 illustrates the main differences between UV-F (fluorescence), UV-A (absorption) and chromatograms at 350 nm (Trejo et al., 2007).

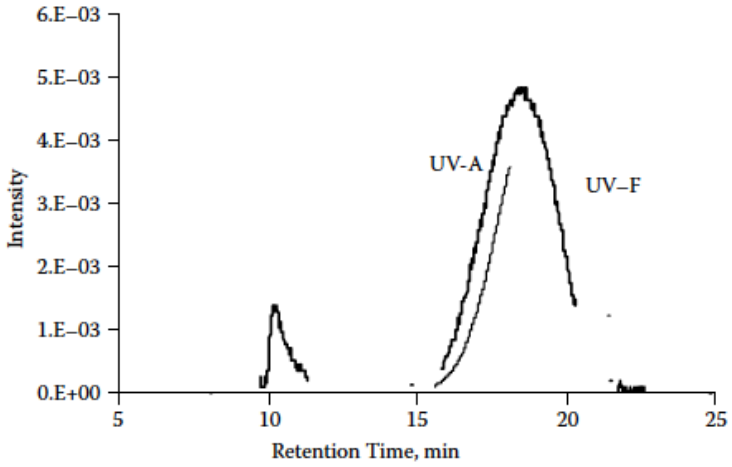

Figure 2-3: SEC Profiles with UV-F and UV-A in NMP at 350 Nm of Asphaltenes from Maya Crude Oil. (Trejo et al., 2007).

In utilizing a higher solvent power of NMP, a sizeable material eluting could be seen with the UV-A detector near the chromatographic column exclusion limit from 6.5 min onward. The UV-A signal exhibited smaller distribution compared to UVF chromatogram, most likely due to the fact that smaller aromatics tend to exhibit more fluorescence. If fluorescence is absent or weak, this is likely due to structural reasons or molecular interactions dimming fluorescence intensity and red shifts, as mentioned previously (Ascanius et al., 2004). According to Herod et al. (2007), most researchers agree on UV fluorescence not being able to detect molecular weights exceeding 3,000 g/mol. Earlier, Herod, working with Kandiyoti (1995), found a progressive shift in spectral maximum intensity for UV fluorescence and molecular weight, and also noted a reduction in fraction mobility on the planar chromatographic plate. To (Herod and Kandiyoti, 1995), this indicated a polynuclear aromatic system that increases progressively.

(Similarly, Strausz et al., 2002) believed there are differences in fluorescence properties according to the sample's molecular weight. So, for instance, for diluted fractions of Athabasca asphaltenes, the greatest amount of fluorescence appears in the smallest molecular weight fraction, whereas the least amount is found in the highest molecular weight fraction. Also worth

noting here is that, in aromatic chromophores connected by polymethylene, sulfide, or C˘ C bridges (or various combinations thereof), rigid geometrical objects do not provide any rotational motion.

Below is a summary of the three main problems:

1. Aromatic compounds found in asphaltenes are the primary absorbers, but there are numerous asphaltenes that do not absorb in the 300 to 700 nm spectral range.

2. As fluorescence represents the manifestation of an intramolecular-level competitive process, species might absorb but they might not subsequently fluoresce.

3. As asserted by (Cowan and Drisko, 1976) as well as (Brauman, 2000), moieties (e.g., intramolecular H-bonded complexes, metal salts and complexes, clay organics, etc.) can also be quenchers.

(Suelves et al., 2003) also investigated the maximum intensity shift in fluorescence in the direction of longer wavelengths and molecular sizes. However, they believed that rather than being aggregates of smaller molecules, MALDI and SEC molecular weight measurements could be a sign that fluorescing molecules have larger aromatic systems.

2.1.4 X-ray diffraction

In the form of X-ray diffraction (XRD) as conceived by Warren (1941), Franklin (1950), and (Cartz et al., 1956), diffracted waves exhibit pointed interference peaks that have identical symmetry to the atom distribution. We can see a material's atom distribution by measuring diffraction patterns, in that the peaks are proportional to atomic distances. Figure 2.5 illustrates a 2-dimensional incident X-ray beam interacting with periodically-arranged atoms.

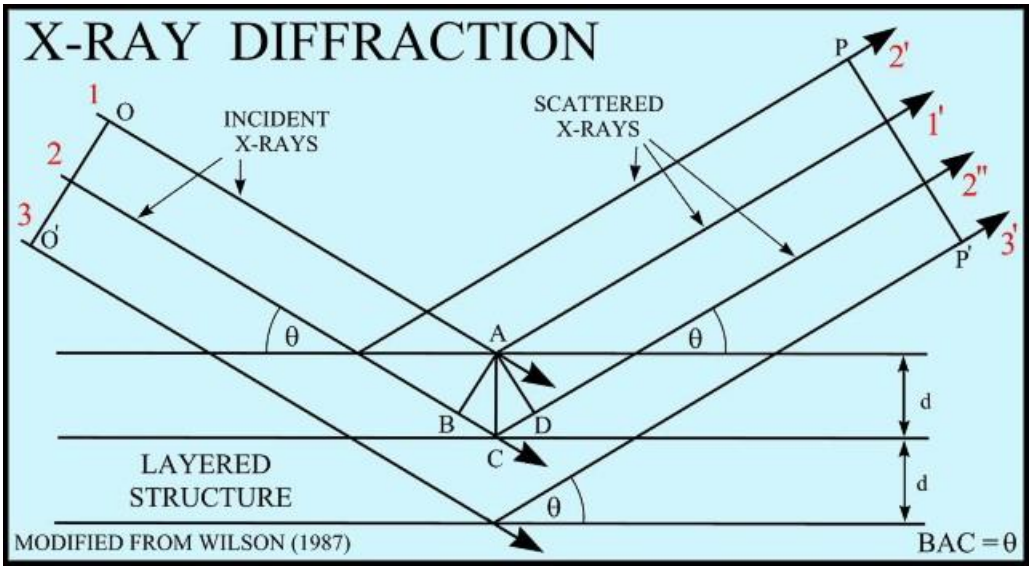

Figure 2-4: Diffraction of X-Ray through Cross Sectional View of Asphaltene Clusters (Westmoreland, D., 2015).

Since the mid-1900s, X-ray diffraction has been developed to the point that it can now be used across a broad spectrum of research fields. For instance, (Ergun and Tiensuu, 1959) applied XRD to investigate the structure of coal; (Alexander and Sommer, 1957) used it to explore the features of carbon black structures; (Ruland, 1967) used it to look into noncrystalline polymers aromatic systems; and (Shiraishi et al., 1972) used it to study pitch fractions. Additional mid-century work in the field was undertaken by (Yen et al., 1961), who used XRD on petroleum asphaltenes. The researchers found the method useful for measuring the distance between aromatic layers in relation to the grapheme (002) band that manifests at around 26°, as well as for measuring the distance between aliphatic layers that manifests at around 20° (Yen et al., 1961). Moreover, XRD has been found to offer important details about asphaltene's internal structure, including for the extraction of molecular crystallite parameters in relation to aggregates (Shirokoff et al., 1997).

Because asphaltene aromatic cores can be arranged to create a stack of aromatic sheets, we can use XRD analysis, as stacking enables the formation of crystallites. (Siddiqui et al., 2002) stated that XRD can also be used to analyze additional crystallite parameters like polar aromatics, naphthene aromatics, and saturate fractions; they applied the approach to Arabian asphalts (Siddiqui et al, 2002). (Schwager et al., 1983) suggested applying XRD to develop a hypothetical crystallite which can then show asphaltene structure. Using stacked condensed aromatic sheets, where the sheets are parallel and naphthenic rings and aliphatic chains appear at the edges, we can obtain the following crystalline parameters:

L_a = aromatic sheet diameter and alkyl chains α -carbons (Å).

L_c = approximate height of aromatic sheet stack situated perpendicularly to the sheet's plane (Å).

d_m = distance of inter-aromatic layer (Å).

d_γ = distance of inter-chain and/or inter-naphthene layer (Å).

M = approximate number of related aromatic sheets in the stacked cluster.

We can then use the Bragg relation to calculate the crystalline parameters of inter-layer distances among aromatic sheets (d_m), which can be based on the (002 band maximum (Siddiqui et al., 2002), as follows:

$$d_m = \lambda\, 2sin\theta \tag{2.1}$$

Where λ represents wave length (Å) and θ represents the angle of the peak's center. The full-width half-maximum (FWHM) must be tabulated from the approximate height of the aromatic sheet stack situated perpendicular to sheet plane (L_c), as follows:

$$Lc = \lambda\, \omega\, cos\theta \tag{2.2}$$

Where ω indicates FWHM. Meanwhile, the aromatic sheets in a stacked cluster (M) are formulated in the following equation to find their number:

$$M = \frac{L_c}{d_m} + 1 \tag{2.3}$$

According to the results, interlayer distance (d_m) can vary slightly from 3.5 to 3.7 Å, inclusive, while dγ can range from 4.4 up to 5.4 Å. Figure 2.4 illustrates potential stacking of asphaltenes. As can be seen, the XRD approach provides quantitative-intensity curves, while the shape and peak positions provide structural parameters. Andersen et al. (2005) asserts that asphaltene crystallographic parameters depend on a broad range of assumptions as well as the type and complexity of the data. Researchers should avoid the temptation to over-simplify their interpretation, as the asphaltene system is highly complex and stacking is just a small portion of aggregation.

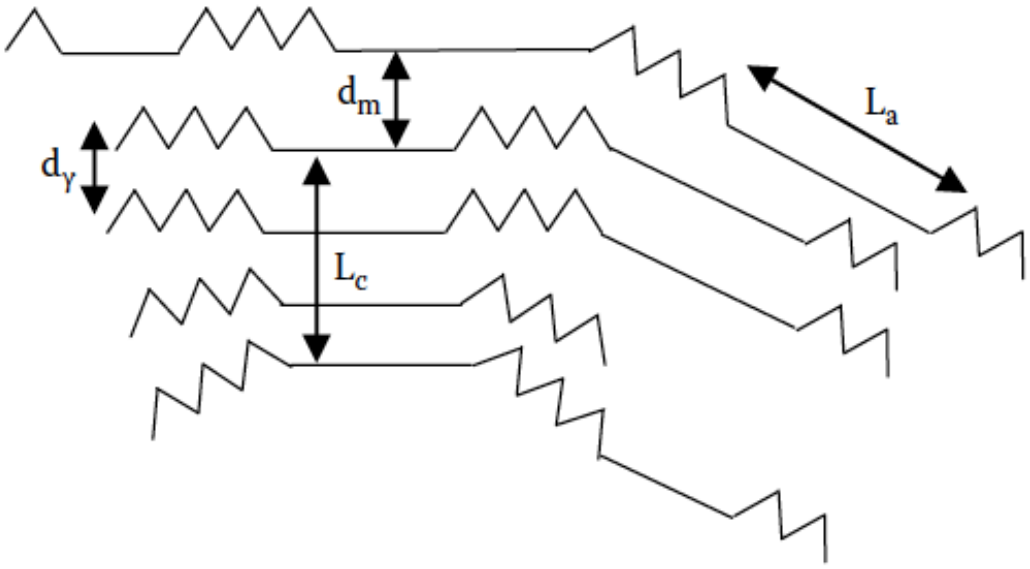

Figure 2-5: Cross-Sectional View of Asphaltene Model; Zigzag Structures Represent The Configuration of Alkyl Chains or Naphthenic Rings and The Straight Lines Represent The Edge of Flat Sheets of Condensed Aromatic Rings (Schwager et al., 1983).

As most asphaltenes exhibit a 002 peak at approximately 26°, we can surmise that interlayer spacing is around 3.55. As shown in Table 2.2, an extensive variety of interlayer spacing has been cited in the literature (e.g., (Andersen et al., 2005); (Kumar & Gupta, 1995); (Adams et al., 1998); (Bouhadda et al., 2000); (Hishiyama & Nakamura, 1995); (Shirokoff et al., 1997); (Buenrostro Gonzalez et al., 2002); (Suresh Babu & Seehra, 1996); and (Alvarez et al., 1999).

Table 2.2: Reported Magnitudes of XRD Derived Parameters of Different Carbon and Hydrocarbon Material (Andersen et al., 2005).

Material	d_{002} band, Å	L_c, Å	L_a, Å
Graphitized Assam coking coal	3.338	220	110
Single-crystal graphite	3.354		
High-purity graphite	3.357	458	324
Thermal graphite	3.364	710	990
Turbostratic film	3.437	16.4	40.4
Semicoke (H/C = 0.75)	3.52	35	
Hassi-Messaoud asphaltenes	3.56	16.5	9.5
Baxterville asphaltenes	3.57	19	10
Arab Berri (H/C = 1.02)	3.60	22.7	13
RT-asphaltene	3.70	14.3	9.9

(Futheiz, Shirokoff and Lewis, 2016) conducted a study of computer controlled X-ray diffraction (XRD) spectra of heavy oil components were characterized by studying the important X-ray peaks (i.e. planes of 002-graphine and gamma). This procedure used different background types in order to assess the precision of fit and residual error of fit (level, 3rd order polynomial and 4th order polynomial). Mathematical functions (Pearson VII, pseudo-Voigt, generalized Fermi) were employed with varying Pearson VII exponent (0.75, 1.25, 1.75) and pseudo-Voigt Lorentzian (0.2, 0.6, 0.8) when profile fitting the XRD data. In general they have shown that they

affect the peak position and calculated average size of crystallite parameters for interlayer distance between the aromatic sheets (d_M) for Pearson VII is 4, less than 5 for pseudo-Voigt and distance between the saturated portions ($d\gamma$) for Pearson VII is 7, greater than 6 for peudo-Voigt . The results are explained in terms of the calculation of X-ray background intensities, peak shape function, profile fitting, asymmetry of XRD data, and residual errors for fitting background radiation.

2.1.4.1 Asphalt as cubic material (Yen model)

In XRD patterns, asphaltene exhibits four distinct peaks. The first peak (peak 1) is considered the saturated structural packing distance that results from X-rays undergoing scattering due to condensed saturated rings and aliphatic chains. The graphene peak (peak 2) results from the XRD of aromatic molecule stacks, as proposed by Siddiqui et al. (2002). The third and fourth peaks, numbered as (100) and (110), respectively, in XRD result from the aromatics in-plane structure, as shown in Figure 2-7. In the ring compounds, these peaks, respectively, relate to the first and second nearest neighbors in solid crystals, and short-range orders in others. Thus, the diffraction patterns exhibit sharp peaks but only a singly broad peak.

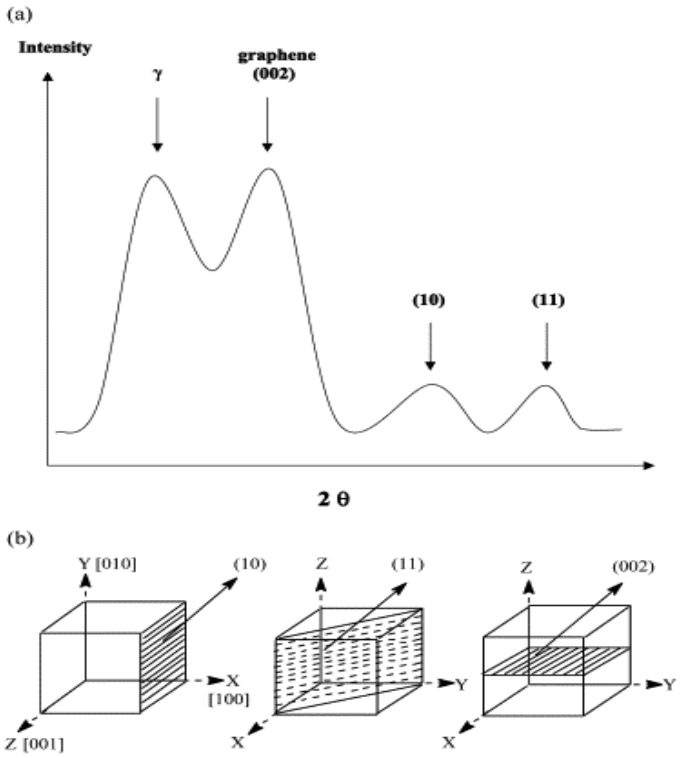

Figure 2-6: The Bands and Planes of an X-Ray Diffractogram (Yasar, et al., 2009).

2.1.4.2 Modified Yen model (the Yen-Mullins model)

In recent years, there has been renewed research interest around asphaltene properties, with a focus on molecular weight and structure. Mullins (2010) discussed how long-standing disputes over asphaltene's molecular weight are beginning to be resolved through the application of various accepted techniques. Despite these promising change, asphaltene's properties remain for all intents and purposes still lacking in a clear definition due mainly to the complexity of the material's structure. Figure 2.8 provides some details about its properties.

In exploring the many facets of asphaltene, we can use the modified Yen model as a means to deal with the enormous amount of data (Mullins, 2010). The modified Yen model represents a first principle approach and can thus be applied towards asphaltene properties in bulk as a way to break down the analysis into more manageable portions (Mullins, 2010).

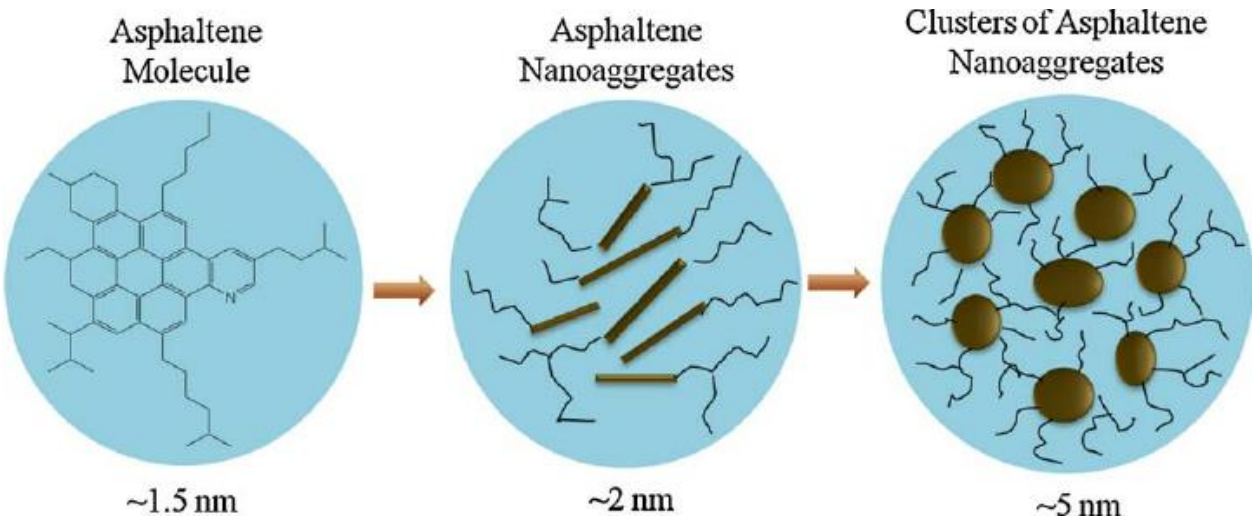

Figure 2-7: The Yen–Mullins Model (Zuo et al., 2012).

Working from his earlier studies, Mullins and colleagues (2012) further investigated asphaltene, discovering that the asphaltene nanoscience model can be correlated to the modified Yen model. This is an exciting discovery, as it may prove to resolve, on the nano-scale, many contentious issues regarding the behavior of compounds, including composition and structure. Figure 2.9 illustrates some potential resolutions to long-standing issues plaguing the study of asphaltenes.

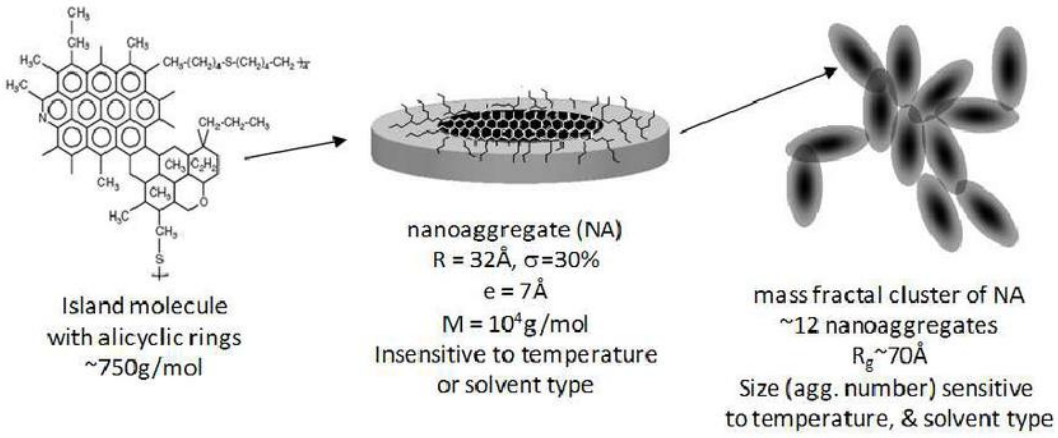

Figure 2-8: An Altered Figure of Asphaltene Nanoscience Showing Consistency of Phase Behavior of Asphaltene from the Modified Yen Model (Zuo et al., 2012).

2.1.5 Nuclear Magnetic Resonance (NMR)

Using the nuclear magnetic resonance (NMR) approach, several components can be identified. This is useful, for example, in the analysis of complex hydrocarbons, if one wishes to calculate the number of carbons aromatically and/or aliphatically. (Patt and Shoolery, 1982), as well as (Jakobsen et al., 1982), used the NMR Attached Proton Test, which is described as scalar coupling between a proton and carbon. Such coupling enables the researcher to differentiate between carbon that represents even proton numeration (hence, methylene groups and quaternary carbons) and carbon that represents odd proton numeration (hence, methyne and methyl groups). The so-called direct 13 C method is a standard type of analysis that applies NMR and enables aliphatic and aromatic carbons to be identified. Aliphatic carbons (e.g., CH, CH2, CH3, quaternary aliphatic carbon) range between 70 and 0 ppm, while aromatic carbons (quaternary aromatic carbon) manifest through integrating the chemical shift range from 160 to 100 ppm.

More recently, Ibrahim et al. (2003) applied NMR in the analysis of Kuwait crude asphaltenes, discovering that they have several polycondensed aromatic units (between 5 and 9) joined via alkyl chains 4 to 6 carbons; these chains can either be with or without hetero-atoms. (Seki and Kumata, 2000) reported in their work that the aromaticity factor of asphaltenes during hydroprocessing generally remains consistent at 400 °C, but then the f_a rises to 430 °C (Seki & Kumata, 2000), likely indicating the decreasing of alkyl chains joined to the aromatic core. Such a decrease agrees with the findings of (Merdrignac et al., 2006), who noticed that any carbon left behind in asphaltenes during the conversion process grows increasingly aromatic. The increase in aromaticity and aromatic carbon content could be due to faster conversions in aliphatic chains.

Zajac et al. (1994) used NMR to analyze asphaltenes found in Maya vacuum residue. The sourced aromatic carbon fell into three categories, as follows: (1) peripheral aromatic carbons joined to protons; (2) peripheral aromatic carbons joined to aliphatic carbon; and (3) internal or bridgehead carbons (Zajac et al., 1994). These three carbon types can be used to find the dimensions of aromatic clusters. So, for instance, the asphaltene sample of condensed ring sections measure 11.1 ± 1.4. Given these dimensions, one potential schematic representation could be a condensed aromatic core with nine aromatic rings. Joined to these rings would be naphthenic rings, which would feature nitrogen and sulfur formations in the core. As the primary structure for Maya vacuum residue asphaltenes is the continental type, we can find structural data in the NMR spectra simply by using these equations (Calemma et al., 1995):

$$f_a = \frac{C_{aromatic}}{C_{aromatic} + C_{aliphatic}} \tag{2.4}$$

Where f_a is the aromaticity factor, $C_{aromatic}$ and $C_{aliphatic}$ are the amount of aromatic and aliphatic carbon, respectively,

$$n = \frac{C_{aliphatic}}{C_{substituted\ aromatic\ carbon}} \tag{2.5}$$

Where n is the average length of alkyl chains and $C_{substituted}$ aromatic carbon is all aromatic carbon which has an alkyl substituent attached to an aromatic core,

$$A_S = \frac{Percent\ of\ substituted\ aromatic\ carbon}{Percent\ of\ nonbridge\ aromatic\ carbon} \times 100 \tag{2.6}$$

Where A_s is the percentage of substitution of aromatic rings,

$$R_a = \frac{C_{aromatic} - (C_{unsubstituted\ aromatic\ carbon} + C_{subtituted\ aromatic\ carbon})}{2} - 1 \tag{2.7}$$

Where R_a is the number of aromatic rings, Cunsubstituted aromatic carbon is all aromatic carbon without any alkyl substitution. Other equations to calculate the substitution and condensation index are (Merdrignac et al., 2006)

$$SI = \frac{C_{quat-sub}}{C_{aro-total} - C_{quat-cond}} \tag{2.8}$$

Where SI is the substitution index, Cquat-sub is a quaternary carbon substituted by an alkyl chain, Caro-total is the total aromatic carbon content, and Cquat-cond is the total amount of quaternary carbons linked to other quaternary carbons,

$$CI = \frac{C_{aro-total} - C_{quat-cond}}{C_{aro-total}} \tag{2.9}$$

Where CI is the condensation index. Figure 2.9 is an example of different types of carbon.

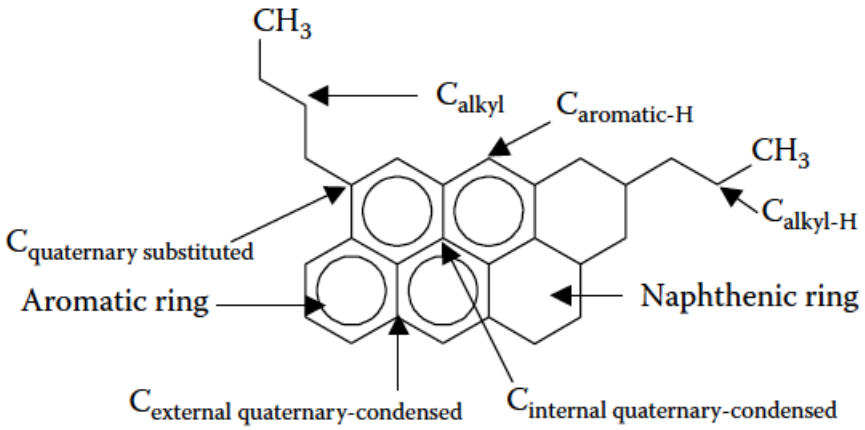

Figure 2-9: Different Types of Aromatic and Aliphatic Carbons.

Although asphaltenes can come from anywhere in the world, most of them still display CI and SI featuring seven condensed aromatic cycles (Calemma et al., 1995). NMR analyses of asphaltenes from Maya, Isthmus, and Olmeca crude are presented in Figure 2.10 (Ancheyta et al., 2002).

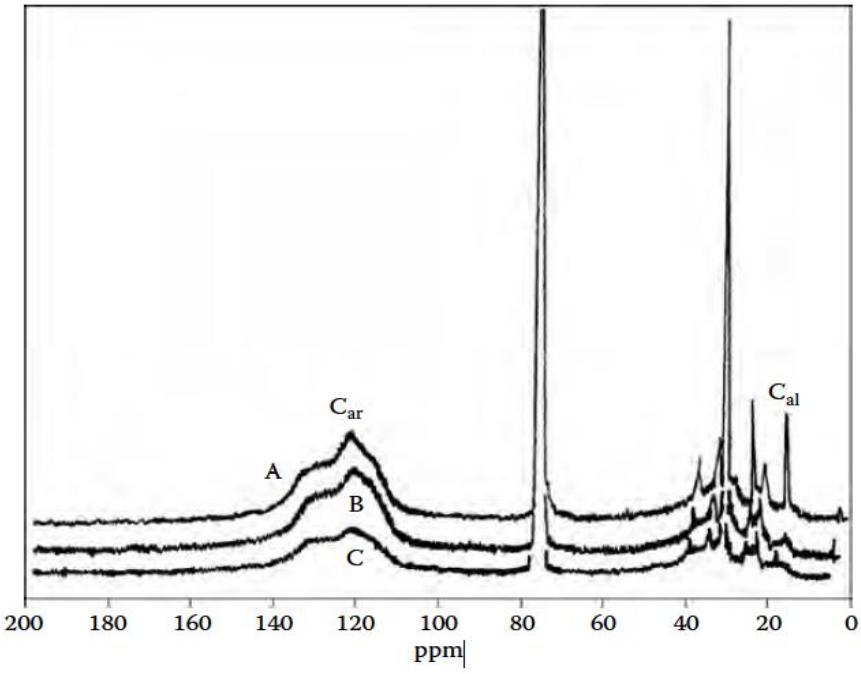

Figure 2-10: NMR Spectra of Asphaltenes Using N-Pentane as Solvent: (A) Olmeca, (B) Isthmus, And (C) Maya (Ancheyta et al., 2002).

Utilizing a variety of solvents for the purpose of precipitating asphaltenes can also have an impact on the material's chemical properties. For instance, according to NMR measurements, heptane leads to more aromatic asphaltenes with larger alkyl chains. Moreover, and as shown in Table 2.3, aggregate molecular weight via VPO can also be much higher if heptane rather than pentane is used. (Zhang et al., 2007) demonstrated this by using NMR to analyze asphaltenes and resins. In quantifying the ring number, they arrived at values of 8.2 and 5.6, respectively, for asphaltenes and resins.

Because asphaltene's aromatic core is primarily comprised of benzene-polycarboxylic acids, it has a peri-condensed structure. (Bansal et al., 2007) studied samples of Residue Fluid Catalytic Cracking (RFCC). They discovered that while saturate and aromatic fraction alkyl chain lengths fall somewhere in the range of normal and is paraffinic hydrocarbons (normal paraffinic/is paraffinic ~1.2-1.4), the condensation index is 25% and the substitution index of

aromatic rings is 47%. Thus, NMR-obtained structural information, in conjunction with functional group analyses and XRD, can be used to discover hypothetical average structures in asphaltene molecules. However, NMR is by far the most useful of all the tools currently being employed toward understanding asphaltene on a molecular level.

Table 2.3: Structural Parameters for Average Molecule of Asphaltenes (Ancheyta et al., 2002).

	Maya		Isthmus		Olmeca	
property	n-c5	n-c7	n-c5	n-c7	n-c5	n-c7
Aggregate MW (VPO)	3680	5190	2603	3375	1707	2663
fa	0.47	0.52	0.59	0.57	0.61	0.62
n	7.4	6.8	4.8	5.0	4.1	5.5
Ra	35	62	34	45	24	40
As	35.6	38.9	37.9	41.0	39.1	32.9

2.1.6 Small Angle Scattering

In crude oil, asphaltenes exist as colloidal structures, so a suitable approach for characterizing them is to apply the small angle neutron and x-ray scattering technique. According to Espinat et al. (1993), a variety of solvents can be used to dissolve asphaltenes in crude oil, but each of these solvents needs to be analyzed to find which one is most appropriate for use at ultra-high temperatures in heavy crude and in vacuum residue. Having a firm understanding heavy crude's colloidal nature is crucial for industry workers, particularly in relation to issues that might arise during refining, transport, or other areas of production. To date, there is a large knowledge gap around the molecular weight of heavy fractions, as well as around the size and composition of aggregates. Alterations undergone by heavy fractions (such as asphaltenes) as a result of rising temperatures or pressure changes over the course of the crude oil processing are

also only partially understood by most industry workers. These gaps in knowledge urgently need to be filled to ensure faster, safer, and more efficient refining.

Small angle scattering is an effective method applied to heavy crudes during analysis of complex fractions. It can be carried out either by X-ray or neutron scattering. Bardon et al. (1996) explained that small angle X-ray scattering (SAXS) measures aromatic rings, while small angle neutron scattering (SANS) gathers information on particle volume. The latter technique is utilized to ascertain asphaltene size and shape under the application of different solvents. When in solution, asphaltenes are similar to polymer-like solutions surrounded by resins (Hirschberg et al., 1984; Laux et al., 1997). (Altgelt and Harle, 1975) had earlier considered using maltenes as a solvent in which to suspend asphaltenes, but this concoction was looked upon by later researchers as a molecular solution instead of a suspension.

Numerous analytical approaches have been suggested and applied as a means to study aggregated asphaltenes. (Xu et al., 1995) investigated Athabasca asphaltenes at concentrations measuring 5 and 15 wt% dissolved in toluene at room temperature, only to find that the sample represented polydispersed spheres with radii of 33. (Savvidis et al., 2001) looked into the internal structure of asphaltenes powder. They discovered that aggregates form a compact system of asphaltene material prone to sedimentation, and that this sedimentation prompts macroscopic phase separation. By applying the SAXS approach, (Fenistein and Barr, 2001) applied ultracentrifugation as a means to separate asphaltenes. Their findings indicated that there is a broad-based range for the radii molar mass and gyration in separated asphaltenes. Pierre et al. (2004) studied how asphaltene concentrates and discovered that asphaltenes share similar structures regardless of the concentration amount.

Additional experiments using SAXS were also performed by a number of researchers in the field (e.g., Giavarini et al., 2000; Barr. et al., 1997; Bardon et al., 1996; Espinat, 1991; Espinat et al., 1984; and Herzog et al., 1988), while experiments based on the SANS technique were performed by (Gawrys and Kilpatrick, 2005). The latter researchers discovered that asphaltenic aggregate shapes stemming from Arab Heavy, Canadon Seco and Hondo asphaltenes can be more effectively studied via an oblate cylinder approach.

A number of experiments were performed by (Spiecker et al., 2003) applying fractionation of n-heptane and toluene on a variety of asphaltenes (e.g., Arab Heavy, Canadon Seco, B6, and Hondo), after which SANS was applied on the aggregates. Spiecker et al. (2003) discovered that the largest aggregates were created by the fractions which were least soluble, and that the aggregate dimensions of asphaltenes grew larger as the solvent aromaticity was reduced. This held true to the solubility limit point, after which reductions in aggregate dimensions were obtained by adding n-heptane. Spiecker et al. (2003) also found that the solubility of Canadon Seco asphaltenes had the biggest aggregates, and that these were affected through aromatic π – bonding as a result of the low nitrogen content and H/C ratio.

Meanwhile, Spiecker and colleagues (2003) also discovered that Hondo and B6 asphaltenes created aggregates that had more or less the same dimensions, a phenomenon which they described as polar interaction-related because of the high nitrogen content and H/C atomic ratio. (Spiecker et al., 2003) also discovered that Arab Heavy asphaltenes manifested extremely small aggregates in the toluene and n-heptane mix. They applied VPP and elemental analysis to get a better grasp of asphaltene aggregation in relation to n-heptane and toluene. A few years earlier, (Fenistein et al, 1998) carried out toluene and n-heptane fractionation together with intrinsic viscosities. They observed that if heptane volume percentages were increased in the

toluene and heptane mix, the intrinsic viscosities found in asphaltene aggregates were at first reduced (i.e., when the heptane percentage was around 10-20 vol%) but then rose when nearing the flocculation point (Feninstein et al., 1998). Applying SANS showed that aggregates in asphaltene possess an open structure in toluene, and that the density increases when n-heptane is added. Furthermore, if the mixture has n-heptane at 15 vol% or more, the aggregates' molecular weight and size undergo continuous growth until reaching the precipitation threshold.

By measuring asphaltene size prior to and after hydrotreating Boscan crude, Ravey et al. (1988) investigated how asphaltenes can change morphology and dimension. The asphaltene concentration in a tetrahydrofuran solution was 1.1 wt% in both non-hydrotreated and hydrotreated asphaltenes, while disc-type aggregates shrank to 0.9 nm (compared to an average of 6 to 20 nm for asphaltenes in good solvent). Characterizing asphaltenes is useful in creating more effective hydrotreating catalysts for processing heavy feedstocks, as asphaltenes' shape and size are crucial parameters in catalyst textural properties. As asphaltenes have the ability to be polydisperse, a suitable hydroprocessing catalyst could have macropores to enable large particles to be diffused within pores (Plumail et al., 1983).

Liu et al. (1995) used Ratawi crude to carry out tests on asphaltenes in high-concentration solutions, applying up to 80 wt% concentrations in toluene. Similar tests and analyses using the SANS approach were performed by (Overfield et al., 1988; 1989), (Sheu et al., 1992), Storm et al. (1993), Storm and Sheu (1995), and Roux et al. (2001). Tanaka et al. (2003), when investigating structural changes in petroleum asphaltene aggregates, used SANS to separate asphaltenes in Iranian Light, Khafji, and Maya crudes dissolved in a variety of solvents (e.g., quinoline, 1-methylnaphthalene, decalin, etc.). The SANS analyses, which were done for temperatures ranging between 25 and 350 °C, indicated topological features that differed

according to the solvent used and/or the origin of the asphaltene. Tanaka et al. (2003) found that, in general, the asphaltenes developed into aggregations across all solvents tested, forming into prolate ellipsoids at 25 °C and shrinking as the temperature rose. The researchers noted that the morphology and size of asphaltenes appeared to be related to the temperature range during analysis. For Maya asphaltenes, decalin was applied as a solvent, creating a fractal network that retained its form even at 350 °C. This is likely related to Maya asphaltenes' high coking tendency.

When (Thiyagarajan et al., 1995) modified their test solvent as 1-methylnaphthalene, they discovered 2 × 15 nm aggregates that appeared rod-like, but when (Sheu et al., 1992) applied toluene, they found asphaltene aggregates that looked spherical and had a radius of 5 nm. However, Maya asphaltenes tested in 1-methylnaphthalene exhibited, at low temperatures, rod-like colloidal particles that had relatively uniform radius but polydispersed lengths. At room temperature, asphaltenes dissolved in the same solvent aggregated into rod-shaped particles with a radius of 18 and different lengths up to 500 nm. Interestingly, increasing the temperature to 100° C resulted in a noteworthy shortening of aggregate length, while the radius was unchanged. At a temperature of 150° C, two particle types emerged: a spherical one with a radius measuring 12, and an ellipsoidal one featuring semi-axes of 12 and 33. A further temperature increase to 320^0 C resulted in a loosening of the ellipsoidal particle concentration. Then, when the temperature was raised to 340 and 400° C, the only particles remaining were the spherical ones with radii of 12. Cooling the samples down to room temperature did not show reversibility (Thiyagarajan et al., 1995).

In (Takeshige, 2001) study, tests on asphaltene viscosity in a benzene solution indicated that asphaltenes can be solvated with only a single molecular layer of benzene, and that any

shape alterations (e.g., from ellipsoidal particles) occurring under ultra-high temperatures might be an indication of covalent bond formation. Figure 2.12 illustrates how both shape and dimensions act as a function of temperature for asphaltene particles (Hunt & Winans, 1999).

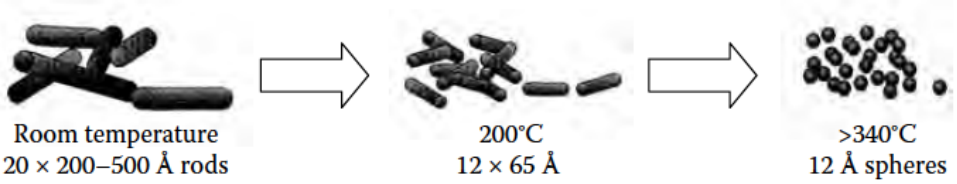

Figure 2-11: Shape of Asphaltenes (5 Wt %) in 1-Methylnaphthalene by Sans at Different Temperatures (Hunt and Winans, 1999).

Overall, the outcome of tests on asphaltenes that were treated in a variety of solvents indicates the type of changes (shape, size, morphology, etc.) they can undergo at high temperatures. For instance, Thiyagarajan et al. (1995) and Roux et al. (2001) found a correlation between reductions in molecular weight and rises in temperature when using organic solvents (). When treating asphaltenes in real crude or its residue, however, the modifications are different. Espinat et al. (1993) and Bardon et al. (1996) used SAXS to study asphaltenes that were dissolved in resins and vacuum residue. The tests revealed that some asphaltenes persisted as "disk-type systems" in resin suspensions. (Espinat et al., 1993) also suggested that lamellar particles in association with paraffinic and aromatic sections could form the origin of asphaltenes. According to (Maruska and Rao, 1987), asphaltene aggregation might possibly be caused by dipole-dipole interactions. They calculated asphaltene's dielectric constants as having a range between 5 and 7, and surmised that asphaltene molecules might contain more than one dipole and measure between 3 and 6.

Meanwhile, Bardon et al. (1996) used the SAXS method of analysis in order to confirm the aggregates' morphology via viscosimetry. (Bardon et al.'s, 1996) results showed that, when

diluted in toluene, Safaniya vacuum residue of 10 to 34 wt% w/w acts much the same way as purified asphaltene solutions and resins in toluene. Furthermore, in the analysis of pure Safaniya vacuum residue, there can, in fact, be changes in electronic density arising from the presence of molecules such as paraffins and aromatics. (Bardon et al., 1996) looked at vacuum residue (artificial) containing asphaltenes at approximately 14 wt% and maltenes at approximately 86 wt% (pure Safaniya), finding good correspondence among them with regard to low Q-values. However, the researchers found a large discrepancy with regard to high Q-values, which pointed to differences in behavior among artificial and pure vacuum residue systems.

Specifically, when tested at around 200° C, the scattering was similar to scattering under room temperature conditions. Density fluctuations appeared at high temperatures as well, whereas under room temperature conditions, the fluctuations are likely caused by asphaltene or resin aggregations, or even paraffin crystallization. When tested at 300° C, the researchers noted that the scattering intensified, and suggested this was likely due to thermal cracking (Bardon et al. (1996).

(Tanaka et al., 2004), using SANS, SAXS and XRD data, developed a 3-point hierarchy of asphaltene aggregates, as follows:

1. **Core aggregates**: These are based on $\pi - \pi$ interactions of stacked asphaltenes and measure around 20.

2. **Medium aggregates**: These represent secondary aggregates of core aggregates and are based on interactions with maltenes, oils, solvents or the medium and measure around 50 to 500.

3. **Fractal aggregates**: These constitute secondary aggregates of core aggregates but, unlike medium aggregates, are based on reaction-limited cluster aggregation (RLCA) or

diffusion-limited cluster aggregation (DLCA); these aggregates can also be independent of media measuring > 1000 (Tanaka et al., 2004).

The model shown in Figure 2.13 illustrates Tanaka et al.'s (2004) hierarchy concept

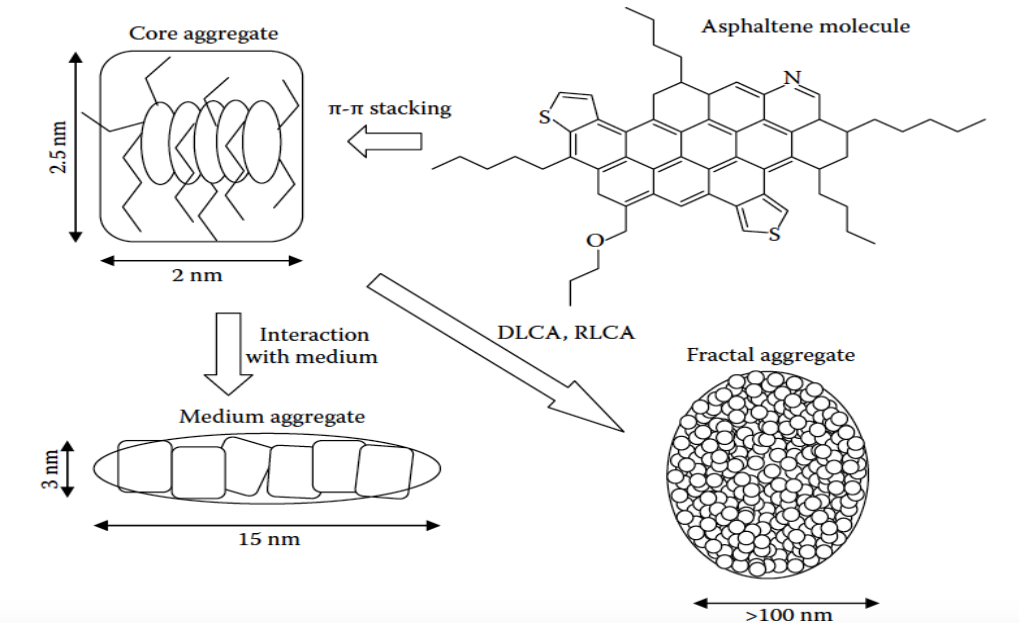

Figure 2-12: Hypothetical Representation of the Hierarchy in Asphaltene Aggregates Based on XRD, SAXS, and SANS Data (Tanaka et al., 2004).

2.1.7 Microscopic analysis

Microscopic analysis can be used to characterize the structure of asphaltenes as well as the modifications it undergoes molecularly during processing. In (Dickie et al., 1969) and (Donnet et al., 1977), we can see how microscopic characterization is able to identify asphaltene and bitumen structure. We can also employ confocal laser scanning microscopy, scanning electron microscopy (SEM), scanning tunneling microscopy (STM), and high resolution transmission electron microscopy (HRTEM) for more in-depth asphaltene imagery. In relation to the latter approach (HRTEM), (Sharma et al., 2002) applied it in their investigations of model compounds. The researchers found that the compounds shared some features with asphaltenes

(e.g., aromatic structures and an attached alkyl chain) and suggested that stacking ruptures could be caused by alkyl chains. Around the same time, (Camacho-Bragado et al., 2002) investigated a purified sample's asphaltene structure through the removal of resins. The researchers used scanning transmission electron microscopy (STEM) and discovered that S, V, and Si were the key heteroatoms making up the structure of asphaltene. With HRTEM, the interlayer distances of aromatic sheets can be calculated, taking into consideration that the sheets are identical to those sensed by XRD with regard to the graphene band of stacked aromatic cores. Under HRTEM testing, the authors likened the image to a cauliflower in structure and measured the space between the aromatic layers as 0.39 nm.

Chapter 3: Research Methodology

3.1 Set-up components

The majority of our knowledge regarding crystalline and amorphous solids comes from investigations based on X-ray diffraction (XRD). So, we can also use the XRD technique to find asphaltene's crystallite structure. In crystals, where atoms are arranged in planes, the incident radiation's wavelength has to be the same order as atomic gaps among crystallographic planes for diffraction to take place. Figure 2.3 illustrates the cross-section of two wavelength X-rays hitting an asphaltene cluster surface at an angle θ.. As can be seen, the aromatic sheets are divided at interplanar distance d_m. Because the planes have a sizeable amount of atoms, they typically exert a strong reaction from the incident x-rays.

In addition to macrostructural data, the XRD technique can offer information on the crystallite parameters of asphaltene aggregate-related molecules. Specifically, XRD can provide quantitative intensity curves, while the positioning and formatting of the peaks gives the structural parameters (Frejo et al., 2007). As a general rule, the greater the tested material's amorphousness, the broader are the peaks in the diffraction patterns. Different XRD-obtained patterns of aromatics, naphthenes and paraffin show the gamma band (γ) resulting mainly from aliphatic ring-ordering or side chains. The (100) band and the graphene (002) band (derived from aromatic molecule stacks) are related to ringed compounds' nearest/second-nearest neighbors (Sadeghi et al., 1986). The gamma (γ) band indicates the packing distance for the layer of condensed saturated rings and/or for aliphatic chains (Siddiqui et al., 2002).

As mentioned previously, the X-ray methods utilized in this study are based on (Yen et al., 1961) and (Sadeghi et al., 1986) investigations into asphaltenes. Hence, various crystallite

parameters, including inter-chain distance dγ, inter-layer distance d_m, and the diameters of aromatic sheets L_a and aromatic clusters L_c, were all derived from X-ray diffraction (XRD) patterns in Canadian asphaltenes. In X-ray intensities calculated for 2θ = 5° to 110°, the curves mirror other peaks. According to (Yen et al., 1961), (Sadeghi et al., 1986) and (Siddiqui et al., 2002), asphaltene XRD patterns typically exhibit 4 main bands, namely: the gamma band (γ), the (002) band, the (100) band, and (110) band.

This present study shows XRD patterns from Canadian asphaltenes that mirror similar characteristics as those from well-known studies (e.g., Yen et al., 1961; Sadeghi et al., 1986; Siddiqui et al., 2002). XRD patterns in Canadian asphaltenes feature 3 characteristic peaks, resulting in 3 distinct peaks of around 17.5° gamma (γ), 20° graphene (002), and 44° (100). As well, we found a faint peak (110) at around 2θ =80°. Such characteristics show a highly dispersed asphaltene order (Andersen et al., 2005). The mean distance is shown here in the graphene band (002) maximum situated at 20° on the 2θ axis among the aromatic sheets. Accordingly, the asphaltenes d_m was formulated using the Bragg Equation $dm = \boldsymbol{\lambda}/2\, sin\theta$, with λ being Cu-K-a radiation wavelength and θ being Bragg angle. it can be seen, the (002) peak appears near 2θ = 20°, showing interlayer spacing at around 4.35, which is close to summarized aromatic structure layers by (Andersen et al., 2005). In fact, (Andersen et al., 2005) and (Trejo et al., 2007) defined amorphous carbon as having interlayer spacing at 3.55 and single crystal graphite structures at 3.35.

Because the size of aromatic sheets determines the d_m value, we can posit that the interlayer spaces in Canadian asphaltenes are similar to small-order amorphous materials, and that the mean spaces between saturated structures can be derived in the same way.

$$d\gamma = (5\,\lambda)/8sin\theta \tag{3.1}$$

The $d\gamma$ values were measured, finding that the asphaltene cluster's mean height, L_c, could be derived from the Scherrer crystallite size equation. This formulation can be made using the graphene band's full width at half maximum (FWHM) approach.

$$L_c = 0.9w\,COS\theta = 0.45/(B\,[1/2] \tag{3.2}$$

The average number of aromatic sheets in a stacked cluster, M, is given by the values of L_c and d_m by using the following equation and its values are reported in chapter 4.

$$M = (L_c/d_m) + 1 \tag{3.3}$$

We can formulate the mean diameter of the aromatic sheets layers, L_a, using Scherrer crystallite size calculations for breadth B [1/2] in band (100) and/or band (110).

$$L_a = (1.84\boldsymbol{\lambda})/(w\,COS\theta) = 0.92/(B\,[1/2]) \tag{3.4}$$

XRD calculations of aromaticity f_a for (002) and gamma (γ) peak area. Aromaticity f_a refers to the aromatic rings' carbon atom ratio to asphaltenes' total carbon atoms, with $A_{(002)}$ being the space beneath the peak (002) and A_γ being the space beneath the gamma peak (γ).

$$fa = \frac{A_{(002)}}{(A_{(002)} + A_\gamma)} \tag{3.5}$$

Where $A_{(002)}$ is the area under the peak (002), A_γ is the area under the gamma peak (γ).

3.2 Sample preparations

We used Alberta (Canadian) crude oil and asphalt for our samples. We first applied solvent separation methods, after which the post-dissolution samples were smeared over glass slide holders and heated in a drying oven at 150 °C for ~10 min. This was followed by a cooling down phase of the samples to ambient room temperature (~25 °C).

Similarly, we prepared thin film asphalt binder samples over glass slide holders, heating them at 150 °C in a dry oven for ~10 minutes, after which they were removed and cooled down to ambient room temperature (~25 °C).

3.3 Thin film method

The XRD approach can be extremely useful in characterizing thin film samples. Because the semiconductor material forms relatively sharp peaks as a result of the material's ultra-low defect densities, there is a need for high angular resolution. Thus, to obtain highly-collimated X-ray beam, several different crystal monochromators are employed for the measurements.

Before being subjecting to XRD, all of the samples were smeared onto a glass slide and then annealed in a drying oven for ~10 minutes. The oven was set at a moderately high temperature of 150 °C to obtain a film measuring approximately 1mm thick. Employing a Rigaku D/Max-2200V-PC with monochromatic Cu-K-a radiation set to function at 40KV and 40mA, a series of XRD tests was performed using a scanning range of 5° to 110° 2θ, a rate of 0.01° 20s- 1, and 5 s/step as a count time. The tool presented a divergence slit of 0.5°, along with a receiving slit of 0.3mm.

Samples were analyzed both pre- and post-oxidation for one week at 20°, and calculated the FWHM and profile fits with Pearson VII and Pseudo-Voigt using six different backgrounds (level, parabolic, linear, fixed, and 3rd and 4th order) across ranges of 5-35° 2θ and 60-110° 2θ

The Jade (version 6.1) software package, which included Pearson VII and Pseudo-Voigt additions, was applied to the creation/analysis of the X-ray patterns. The data were then given a common background so that a comparison could be made of the spectra features of the four main peaks, namely: γ, (002) graphene, (100) and (110). We prepared our XRD samples on standard aluminum sample holders 25 mm in diameter and 1 mm thick. Table 3.1 shows the specimen collected from specific location and all the samples follow the PG standard set by CGSB.

Table 3.1: Pertinent Asphalt Properties.

Asphalt Binders	Modification Type	Grades
655-2	RET+ PPA oxidized	PG 64-34
655-3	SBS	PG 64-34
655-4	SBS + acid-modified	PG 64-34
655-5	SBS	PG 64-34
655-6	oxidized	PG 64-34
655-7	acid-modified Lamont, Alberta	PG 64-34
RR7L		
SC58-34		

3.4 Powder method

The powder form of the XRD method is perhaps the most popular of all X-ray diffraction approaches used in characterizing different substances. In the powder XRD method, the sample has a characteristic powdery consistency made of fine grains from the single crystalline material to be tested. Powder XRD is typically applied when investigating particles in thin film

substances as well as in polycrystalline solids and liquid suspensions. The 'powder' aspect refers to the sample's crystalline domains being scattered (i.e., arranged in a random fashion), such that a two-dimensional recording of a diffraction pattern will display concentric rings of scattering peaks that match the crystal lattice d-spacing.

In the XRD powdering approach, data on the peaks' intensities and locations can be used to determine the material's structure. So, for instance, diamonds' diffraction lines differ substantially from those of graphite, despite both being carbon-based substances. Phase identifications enabled via the powder XRD method is crucial, as most material properties are structure-dependent.

Using original and/or lab samples, several recent XRD investigations have looked into powder diffraction patterns in asphaltenes that have been chemically precipitated out of asphalt cement. A number of structural (e.g., crystallite and aromaticity) parameters have been determined in the studies' asphaltene powder samples, from which data are derived to create viable cross-sectional modeling. In most cross-sectional asphaltene models, the molecules' aromatic sections usually assume a stacking format (the classic "pi stack") due to the Loudon dispersion force.

In the asphaltene model, aliphatic side chains branch out from the asphaltene molecule's center aromatic part. The side chains serve as quasi-templates that enable wax to crystallize. Lu and (Redelius, 2006) discovered and isolated paraffin waxes within asphalt cement, and then studied their XRD spectra.

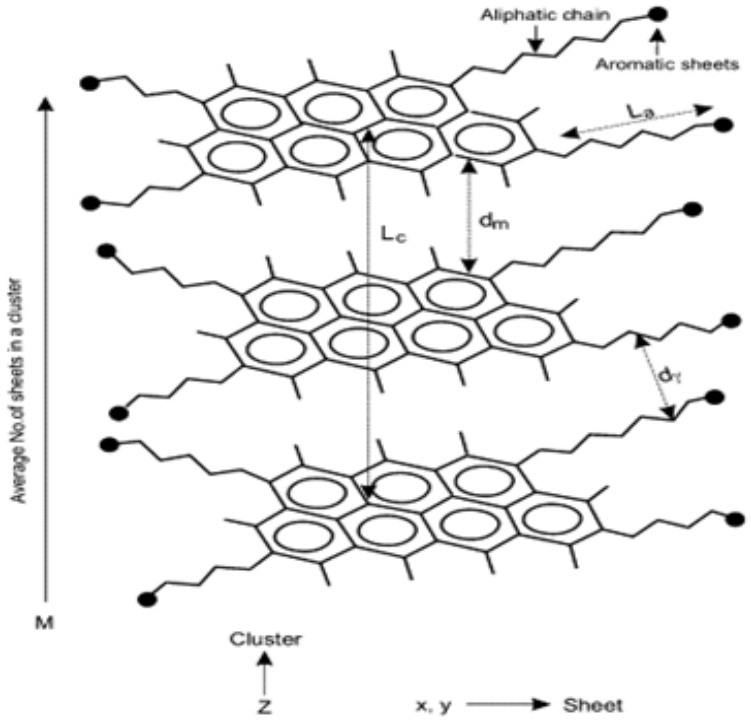

Figure 3-1: The Cross Section of Asphaltene Cluster Structure Model.

3.5 Applying mathematical approaches to spectral line shapes modeling

Finding aromaticity, f_a, by dividing γ and (002) bands requires using a few possible error sources. The first source is small-angle scattering, an approach that raises the intensity of the γ band's low-angle side. In broader peaks, scattering can be difficult to discern, as there are no discrete lines but instead only intensity reductions as the angles increase. If we assume the γ band as symmetrical, we could infer the band's low angle side intensity as being small-angle scattering and therefore neglect it when calculating *f*. Other error sources can arise due to the intensity of the (002) band. So, for instance, a 2.4 nm sample consisting of 7 layers might give an intensity measuring 1.17 times over that exhibited in a 0.7-1.1 nm thick 2-layered sample. From this example, we can see that differences in the samples' size distribution could cause errors in *f*.

In our studies, however, the asphalt binders all share similar L, while the γ band's FWHM has nearly identical size distribution.

3.6 Pearson VII and Pseudo-Voigt

The diffraction approaches adopted nowadays differ significantly from those used even a few decades ago. The main changes have been in data analysis and the instruments used. Today, the process is primarily computer-based, with computer programs providing solutions for nearly every research stage, while collecting and processing large amounts of data. Given this trend in instrumentation, it is highly likely that line-broadening analysis will be adopted as (a) means to obtain routine program output in conjunction with intensities, lattice parameters, line positions, and so on. There is already widespread and accepted use of full-pattern analysis software that involves parameters relating to domain strain and size. However, line broadening inspection has not yet become standard form and thus can promote various degrees of inaccuracy due to outdated or unsuitable models currently utilized in many programs.

To rectify this situation, (Balzac and Led better, 1995) pioneered a method derived from voicing functions, as they discovered that Cauchy and Gauss functions fall short on modeling diffraction line broadening with any accuracy. Hence, a model that follows the Voigt function could prove not only more accurate but also more realistic. Furthermore, the Warren-Averbach approach, which was formerly considered a divergent method, along with integral-breadth methods, are assume to be interrelated. In fact, elements such as the functional dependence of mean square strain on averaging distance highlighted in the Warren-Averbach approach share similarities with the so-called double-Voigt model.

Nevertheless, there are a few potential practical and theoretical limits in the Voigt-based models. From a practical perspective, the line profiles could dip beneath the Voigt-Cauchian limit, while theoretically, profiles could be asymmetrically physically broadened. Absent a more efficient option, however, the Voigt function is still relatively effective. In fact, the Voigt functional form has for some time provided the basis for X-ray photoelectron spectroscopy (XPS) spectra quantitative analysis. Considering that there is no analytic form representing Gaussian Lorentzian (G*L) convolution, two approximations to the Voigt function can be applied, as follows:

Gaussian/Lorentzian Product Form:

$$GL(x,F,E,m) = \frac{\exp(-4ln2(1-m)\frac{(x-E)^2}{F^2}}{(1+4m\frac{(x-E)^2}{F^2})} \tag{3.6}$$

where the following parameters: (m = weighting parameter varying from 0-1), (E =center point), (F = the width). And (x= functions are symmetric about the y-axis).

Gaussian or Lorentzian Sum Form:

$$SGL(x,F,E,m) = (1-m)\exp(-4ln2(1-m)\frac{(x-E)^2}{F^2} + \frac{m}{(1+4\frac{(x-E)^2}{F^2})} \tag{3.7}$$

3.6.1 Voigt-type line shapes in exponential asymmetric blending

For the Lorentzian or Gaussian symmetric line shapes given in the above, an asymmetric profile can be formulated using the following blend function:

$$Y(x) = GL(x) + (1 - GL(x)) * T(x) \tag{3.8}$$

Where,

$$T(x,k,F,E) = \begin{cases} \exp\dfrac{(x-E)}{F}, & if\ x \le E \\ 1, & Otherwise \end{cases} \tag{3.9}$$

3.7 Using peak search and profile fit in line shape analysis

Employing parabolic filtration comprising screened-out Ka-2 peaks, peak location summit, intensity cutoff 0.1 percent, threshold sigma 3.0, a range-to-find background at 1.0, a points-to-average background at 7 (all based on 10,000 raw data points), we peak-searched XRD spectra at angular ranges from 5 to 110°. Then, by applying Pearson VII and/or Pseudo-Voigt functions (6 backgrounds, Exponent = 0.75, 1.25 and 1.75, and Lorentzian = 0.2, 0.6 and 0.8), we calculated the profile fits along with FWHM using over 2θ ranges at 5 to 35° and 60 to 110° on our desired XRD line spectra. Additionally, we modeled the spectra using the computation program software *Mathematica* and the generalized Fermi function (GFF).

3.8 Generalized Fermi function (GFF)

A shown in Eq. 4.4, GFF is input in Mathematica software in order to fit the XRD raw data. A sampling of the process and codes employed as well as a simulation of specimens are presented in the Appendix.

Chapter 4: Results and Discussion

In keeping with the Yen model, XRD patterns in asphaltene binders exhibit 4 main peaks: γ, (002) graphene, (100), and (110). Table 4.1 presents some data showing values of GFF of f_a = 0.4 and d_m = 4.29. These data underscore the fact that GFF profile-fitting is not as reliable as P and V profile-fitting. This lack of consistency is likely caused by the fact that there is no role of neither the background nor the change of parameters such as Lorentzian in Pseudo-Voigt and Exponent in Pearson VII, which thus indicates that GFF exhibits heightened the lack of sensitivity with regard to asymmetry and gives only one value for crystallite (d_m) and aromaticity (f_a) parameters that are either higher or lower than they should be.

4.1 XRD Patterns

In the 8 asphalt binder samples used, the XRD patterns were created using the standard techniques methods mentioned in Jade software. In Figures 4.1 to 4.4, we can see the asphalt binders (labeled 655-2, to 655-7, RR7L and SC58-34), as follows:

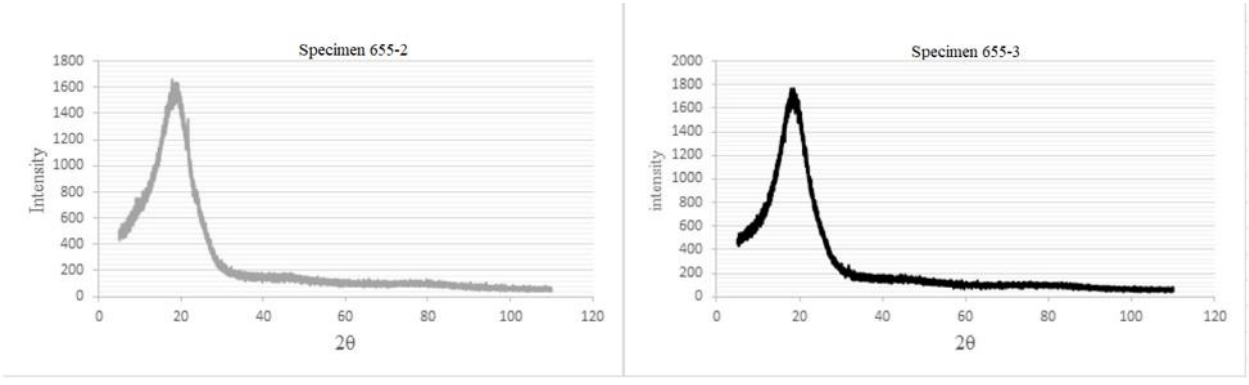

Figure 4-1: Specimen 655-2 and 655-3 of XRD Profile.

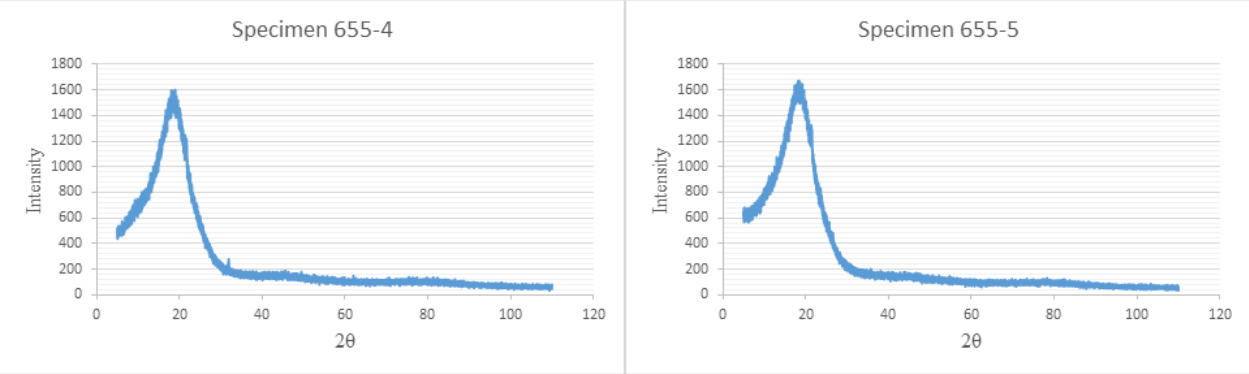

Figure 4-2: Specimen 655-4 and 655-5 of XRD Profile.

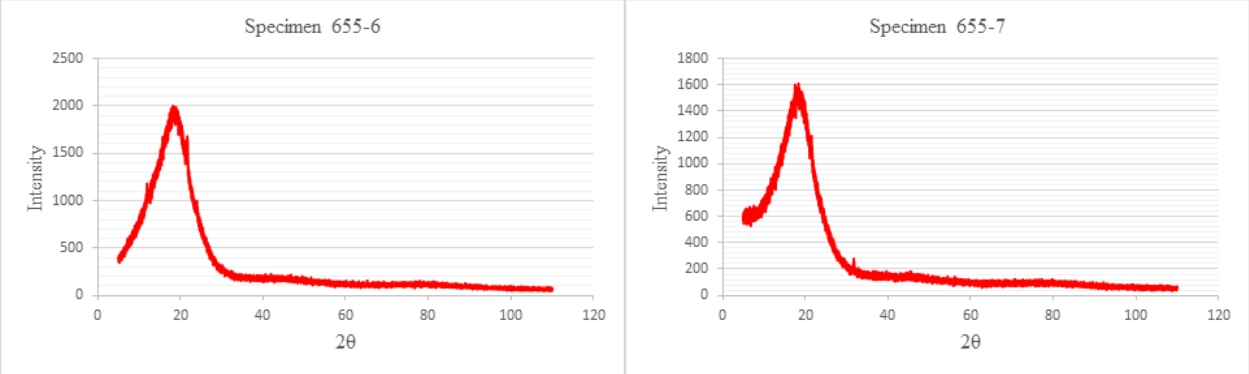

Figure 4-3: Specimen 655-6 and 655-7 of XRD Profile.

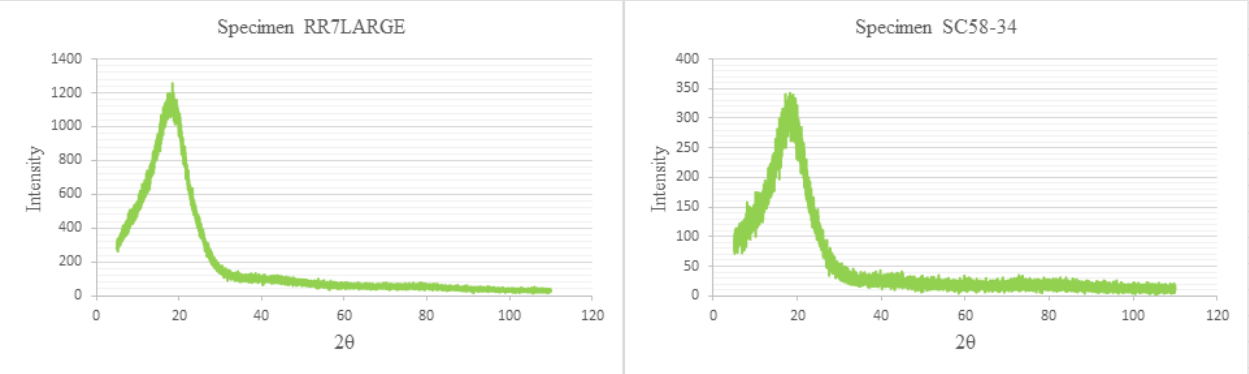

Figure 4-4: Specimen RR7L and Sc58-34 of XRD Profile.

4.2 XRD measurements

As shown in Figure 4.5, we fit the data obtained from the XRD data to either/or the Pseudo-Voigt and Pearson VII profile functions. It is worth noting that true Voigt represents a

Gaussian and Lorentzian convolution, whereas Pseudo-Voigt represents linear combination of the same components. However, because the true Voigt approach can be significantly more complex computationally, the Pearson VII method is preferable. This approach involves Gaussian and Lorentzian components being exponentially mixed. Information regarding the potential applications of Pseudo-Voigt and Pearson VII, including details of their symmetry and shapes, is provided in the following sections.

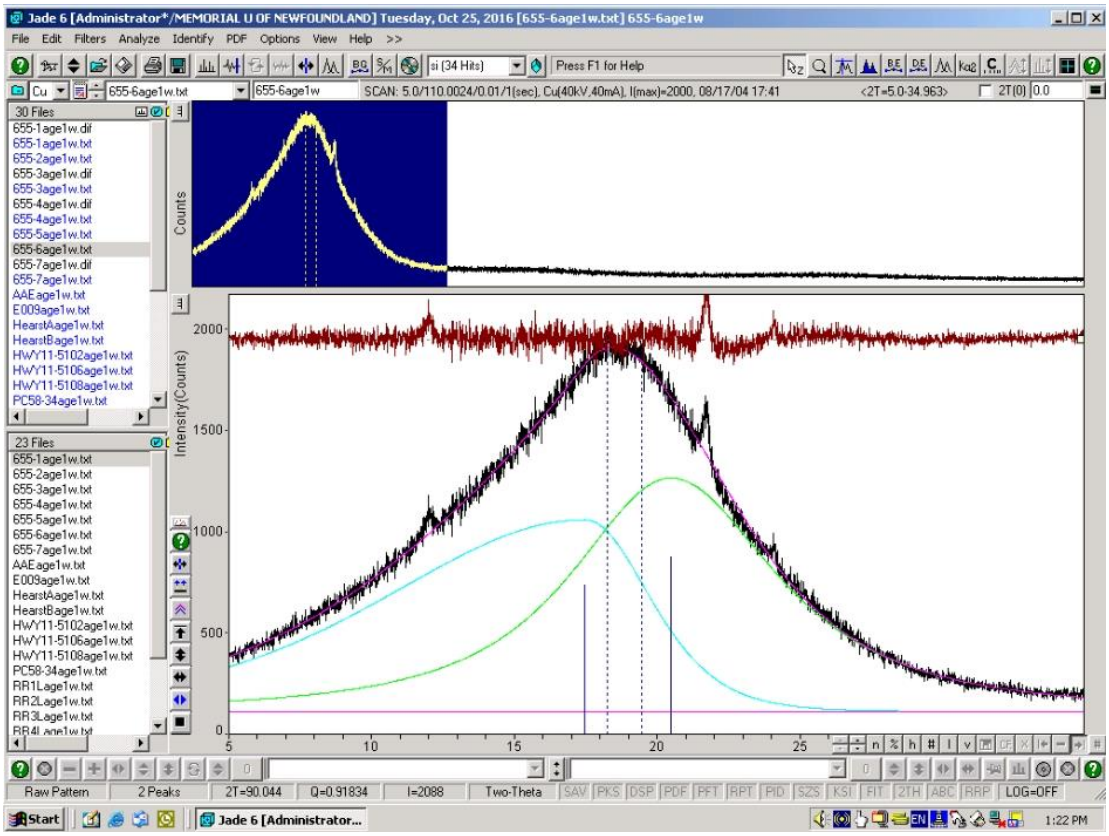

Figure 4-5: Profile Fit of Asphalt Binder.

4.3 Peak Shape Functions

As depicted in Figures 4.1 to 4.4, we can locate the intensity, Y(i), from the ith point's general form in the ($1 \leq i \leq n$) diffraction pattern, with n representing all the measured points

and being the contribution summation, *yk*, of the *m* in each Bragg peak (1 =< *k* =< *m*) and background, b(i):

$$Y(i) = b(i) + \sum_{k=1}^{m} I_k \left[y_k(x_k) + 0.5 y_k(x_k + \Delta x_k) \right] \tag{4.1}$$

Where I_k represents the k^{th} Bragg reflection intensity, $x_k = 2\theta_i - 2\theta_k$, and $\mathbf{\Delta}x_k$ represents contrasts among K$\boldsymbol{\alpha}_1$ and K$\boldsymbol{\alpha}_2$ component Bragg angles in the XRD doublet γ and graphene (002) in asphalt binders. By applying the Bragg intensity in this equation as a multiplier, we can analyze the behaviors of a variety of normalized functions without deferring to peak intensity. In other words, we make the assumption that, for each case, the peak shape function's definite integral (working from negative to positive infinity) is unity. Based on this approach, we define 4 typical empirical peak shape functions (*y*) as below:

$$y(x) = PV(x) = \eta \frac{C_G^{1/2}}{\sqrt{\pi} H} exp(-C_G x^2) + (1 - \eta) \frac{C_L^{1/2}}{\pi H'} (1 + C_L x^2)^{-1} \tag{4.2}$$

Where H and H' indicate FWHM.

Pearson-VII:

$$y(x) = PVII(x) = \frac{\Gamma(\beta)}{\Gamma(\beta - \frac{1}{2})} \frac{C_P^{1/2}}{\sqrt{\pi} H} (1 + C_P x^2)^{-\beta} \tag{4.3}$$

GFF:

$$h(s) = \frac{A}{exp\big(-a(s-c)\big) + exp(b(s-c))} \tag{4.4}$$

Where A, a, b, c represent unknown parameters described as $s = \frac{2\sin\theta}{\lambda}$, and where the A and c values represent the fit's amplitude and position, and (a) and (b) represent the fit's control shape.

$$X = \frac{(2\theta_i - 2\theta_k)}{H_k} \tag{4.5}$$

Where X indicates the diffraction pattern's i^{th} point Bragg angle, which is based on dividing the k^{th} peak position by the peak's FWHM.

Thus, $2\theta_i$ represents the diffraction pattern's i^{th} point Bragg angle.

And $2\theta_k$ represents the ideal Bragg angle in the k^{th} Bragg reflection.

$C_G = 4\ln 2$, while $\frac{\sqrt{C_G}}{\sqrt{\pi}H}$ indicates the Gauss function normalization factor as:

$$\int_{-\infty}^{\infty} \frac{\sqrt{C_G}}{\sqrt{\pi}H} \exp(-C_G\ x^2)\ dx = 1 \tag{4.6}$$

$C_L = 4$, while $\frac{\sqrt{C_L}}{\pi H'}$ indicates the Lorentz function normalization factor as:

$$\int_{-\infty}^{\infty} \frac{\sqrt{C_L}}{\pi H'} (1 + C_L\ x^2)^{-1}\ dx = 1 \tag{4.7}$$

$C_P = 4(2^{1/\beta} - 1)$, and $[\frac{\Gamma_\beta}{\Gamma_{(\beta - 1/2)}}] \frac{\sqrt{C_P}}{\sqrt{\pi}H}$ are the Pearson VII function normalization factors as follows:

$$\int_{-\infty}^{\infty} [\frac{\Gamma_\beta}{\Gamma_{(\beta - 1/2)}}]\ \frac{\sqrt{C_P}}{\sqrt{\pi}H} (1 + C_P\, x^2)^{-\beta}\ dx = 1 \tag{4.8}$$

$$H = \sqrt{(\mathrm{U}tan^2\theta\ +\ \mathrm{V}\tan\theta + \mathrm{W})} \tag{4.9}$$

The Caglioti formula (above) shows that the FWHM is a function of θ for Pseudo-Voigt, Pearson VII and Gauss, whereas U, V, W represent free variables and Γ, indicates the gamma function (Pecharsky et al., 2005).

$$H' = \frac{U}{cos\theta} + V\ tan\theta \tag{4.10}$$

Where H' represents the FWHM as a function of θ in the Lorentz function, and U and V indicate free variables.

$$\eta = \eta_o + \eta_1 2\theta + \eta_2\theta^2 \tag{4.11}$$

Where,$0 \leq \eta \leq 1$ while η represents a mix parameter for the Pseudo-Voigt function. In other words, it is the Gauss function's fractional contribution as part of the combined linear Gauss and Lorentz functions, where η_o , η_1 and η_2 indicate free variables.

$$\beta = \beta_o + \frac{\beta_1}{2\theta} + \frac{\beta_2}{2\theta^2} \tag{4.12}$$

Where β Indicates the exponent working as a Bragg angle function as part of the Pearson-VII function, whileβ_o, $\beta_1$and β_2 representsare free variables.

Figure 4.6 depicts the peak shape functions for both Gauss (dashed-dotted line) and Lorentz (solid line) peak shape functions, while the FWHM is represented by thick horizontal arrows.

As can be seen, the two peak shape functions that are least complex are Gaussian and Lorentzian distributions working from Bragg peak intensities. Moreover, the Lorentz function shows a sharp peak close to the maximum, with lengthy “streams” flowing on both sides close to the base. Conversely, the Gauss function a round maximum and shows no such streams. Nonetheless, both functions can be described as centrosymmetric, in that: G (x) = G (- x) and L(x) = L (- x).

The formation of real Bragg peaks is an outcome derived of functions ranging from convoluting multiple instrumental to specimen functions. As such, they cannot be adequately described in XRD as Gaussian and Lorentzian distributions. Because peak shapes typically occur among these distributions, they can most accurately be described using a mix of the two, such as, for instance convoluting the Gauss and Lorentz methods as a variety of proportions. Convolution, however, can be a complicated process involving numerical integration if any of the peak shape function parameters are modified. Thus, an easier version Gauss and Lorentz linear combination – Pseudo-Voigt – can be applied. In this pared-down approach, we mix Gaussian and Lorentzian compounds (η to 1-η ratio) until the mixing parameter value of 'η shifts to 1 Gauss from 0 Lorentz, keeping in mind that beyond this range in this formulation, η has no meaning. An additional peak shape function that can be applied is the Pearson VII, as presented in Eq. (4.3).

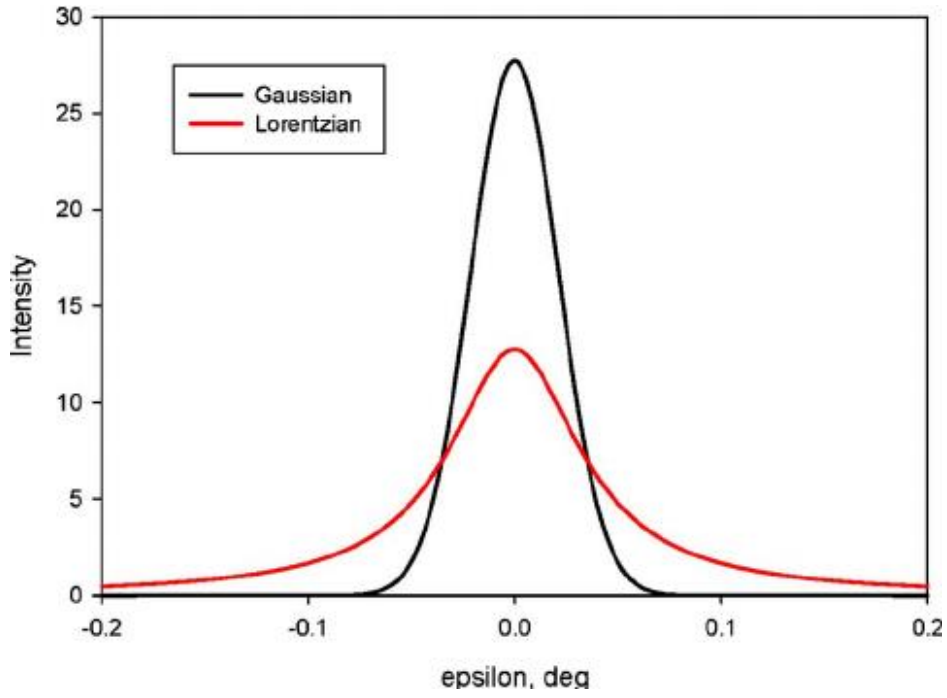

Figure 4-6: Gauss and Lorentz Peak Shape Functions (Gebresellasie, 2012).

A brief examination reveals that this is very much like the Lorentz distribution, other than for the fact that the exponent (β) in Pearson VII can be variable but stays the same (β= 1) in Lorentz. Specifically, Pearson VII offers intensity distribution similar to Pseudo-Voigt, in that when (β = 1), it is the same as the Lorentz distribution; furthermore, when ($\beta \cong 10$), the Gaussian and Pearson VII functions are equal. So, if exponents are 0.5< β <1 or β >10, the peak shape exceeds, respectively, the Lorentz and Gauss functions. That being said, β values only very rarely occur.

Figure 4.6 illustrates XRD profile-fitting employing Pearson VII. As can be seen, the Pearson VII and Pseudo-Voigt functions are depicted as symmetrical. Peak maximum is calculated from the argument, x, in the four empirical functions, as follow:

$$x = 0\,, and\ 2\theta_i = 2\theta_k\,.$$

In both the Pearson VII ad Pseudo-Voigt approaches, the following factors can be noted:

- Peak shape can be accurately modeled by applying Pearson VII and Pseudo-Voigt functions.

- In FWHM, the H occurs in both functions.

- FWHM relates to micros train as well as size of crystallites size.

- FWHM can be successfully modeled by utilizing the Cagliotti Equation given by Eq. (4.8).

- The parameter most closely connected to strain broadening is U.

- The size of crystallites can be formulated using U and W.

- In anisotropic broadening, U can be divided into (hkl)-dependent parts.

Therefore, peak FWHM at a 2θ angle can be given as in Eq. (4.13):

$$FWHM = H = \sqrt{(\mathrm{U}tan^2\theta + \mathrm{V}\tan\theta + \mathrm{W})} \tag{4.13}$$

The H in FWHM is yet another parameter that can help find the argument's value, which can change with 2θ. Being Bragg angle-dependent, the H can be depicted as a function related to empirical peak-broadening. As such, it includes 3 free parameters (*U, V, W*), but the Lorentzian only has 2.

4.4 GFF Spectral Line Shapes Analysis

The figures below show Two of the Eight samples (655-3, 655-2) fits derived from GFF simulation results generated by XRD data. The figures show Two peaks (or bands) indicate that the γ and (002) graphene.

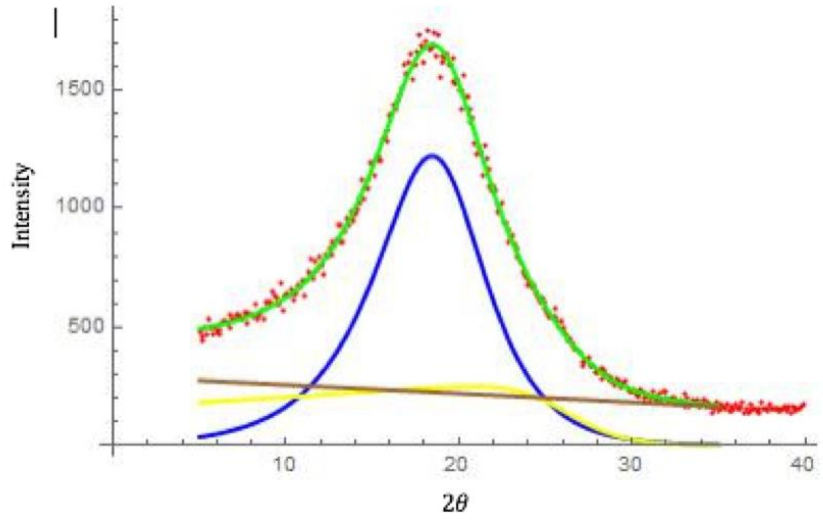

Figure 4-7: Sample 655-3 from GFF.

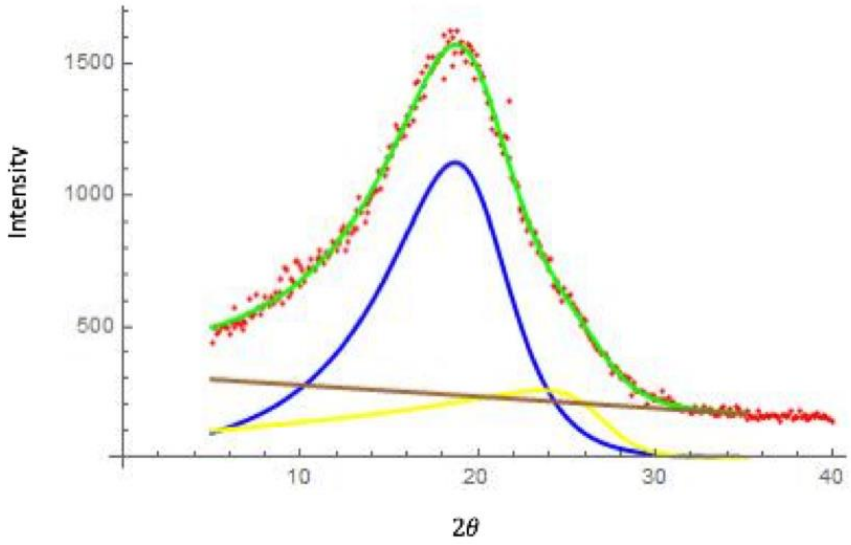

Figure 4-8: Sample 655-2 from GFF.

4.5 Comparing the Results of all Asphalt Samples

The XRD patterns were found must be fit through theoretical distributions. This process is necessary to obtain from the required information about the spectral lines. The fitting functions

of Pearson VII and Pseudo-Voigt were applied, along with 3 major bands – γ, (002) and (100) – located at around 2θ = 17°, 20°, and 44° to enable initial estimates.

In some instance, the (001) band can be found at the (100) peak's high 2θ side, positioned at around 53°. Also required to start the regression process are rough estimates of the peak width and intensity. Furthermore, as backgrounds can cause major problems in XRD patterning of asphaltenes, they could only be presented as a "best fit". Figures (4.9 to 4.16) below show comparison between different backgrounds and functions for the samples. The rest of the figures can be seen in the appendix.

Meanwhile, for the low 2θ side, because the baseline cannot yet be accurately defined, the HRD (high resolution X-ray diffraction system) pattern's high value must, by default, be applied as the baseline. However, the process then involves errors arising from reasonable assumption and/or statistical inaccuracies, both of which can skew results. It is worth noting that alterations in the baseline generally had no or only a very minor impact on results related to factors like aromaticity.

Table 4-1: The average values of Aromaticity and Crystallite Parameters Calculated Using Pearson VII, Pseudo-Voigt and GFF.

		Fa			dM			dγ			Lc			La			Me		
Sample	**Background**	**p7**	**v**	**GF**	**P7**	**V**	**GF**	**P7**	**V**	**GF**	**P7**	**V**	**GF**	**P7**	**V**	**GF**	**P7**	**V**	**GF**
655-2	**3d**	**0.52**	**0.53**	**0.52**	**4.44**	**4.44**	**3.77**	**6.33**	**6.35**	**5.93**	**6.36**	**5.67**	**6.15**	**13.01**	**11.58**	**12.58**	**2.43**	**2.28**	**2.63**
655-3	**3rd**	**0.38**	**0.42**	**0.53**	**4.32**	**4.24**	**4.76**	**6.17**	**6.13**	**6.23**	**5.34**	**5.02**	**5.61**	**10.91**	**10.27**	**11.46**	**1.49**	**1.49**	**1.49**
655-4	**4th**	**0.447**	**0.47**	**0.52**	**4.38**	**4.34**	**4.264**	**6.25**	**6.24**	**6.08**	**5.85**	**5.345**	**5.88**	**11.96**	**10.93**	**12.02**	**1.96**	**1.88**	**2.061**
655-5	**4th**	**0.54**	**0.52**	**0.89**	**4.27**	**4.31**	**4.82**	**5.99**	**6.07**	**6.11**	**5.29**	**4.55**	**4.76**	**10.81**	**9.30**	**9.73**	**1.49**	**1.49**	**1.49**
655-6	**Level**	**0.52**	**0.52**	**0.68**	**4.35**	**4.31**	**4.49**	**6.33**	**6.26**	**6.08**	**2.93**	**2.95**	**2.87**	**5.99**	**6.04**	**5.87**	**1.49**	**1.49**	**1.49**
655-7	**Parabolic**	**0.85**	**0.83**	**0.85**	**4.24**	**4.41**	**4.80**	**6.19**	**6.40**	**6.05**	**4.54**	**4.45**	**4.01**	**9.28**	**9.10**	**8.20**	**1.49**	**1.49**	**1.49**
RR7L	**Level**	**0.47**	**0.37**	**0.51**	**3.98**	**4.01**	**4.45**	**5.95**	**5.95**	**6.15**	**2.88**	**2.86**	**2.87**	**5.90**	**5.84**	**5.87**	**1.49**	**1.49**	**1.49**
SC58-34	**Linear**	**0.73**	**0.51**	**0.70**	**4.41**	**4.43**	**4.80**	**6.03**	**6.25**	**5.95**	**3.91**	**3.81**	**3.94**	**8.00**	**7.78**	**8.06**	**1.49**	**1.49**	**1.49**

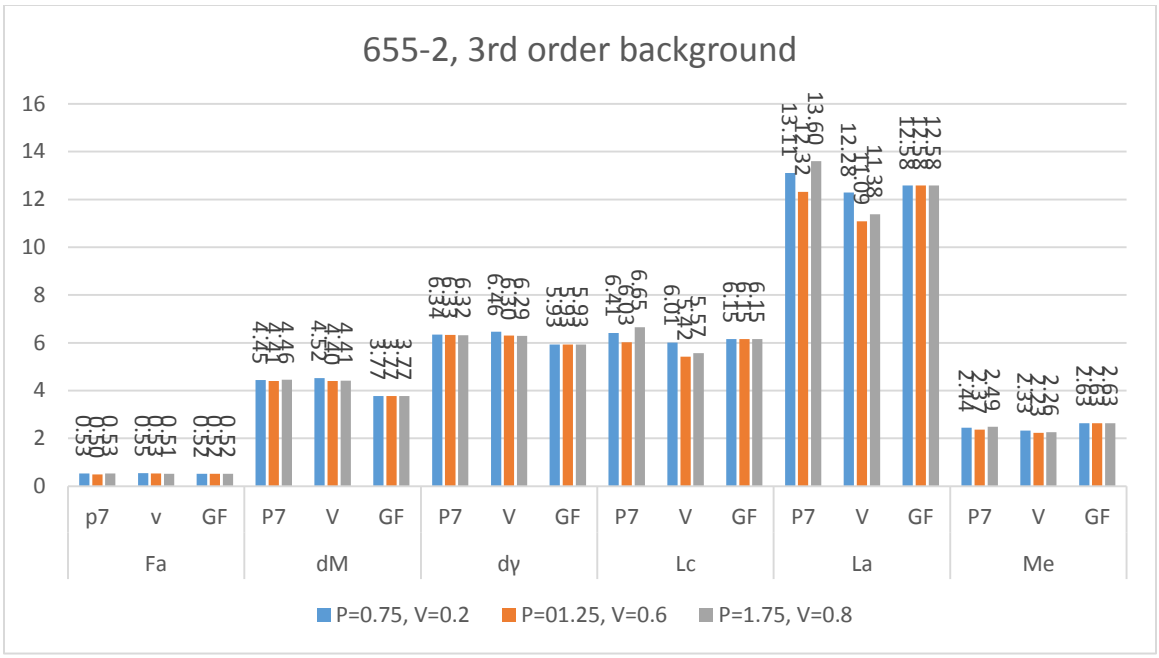

Figure 4-9: Aromaticity and Crystallite Parameters for Sample 655-2 Calculated Using Pearson VII, Pseudo-Voigt and GFF with 3rd Order Background.

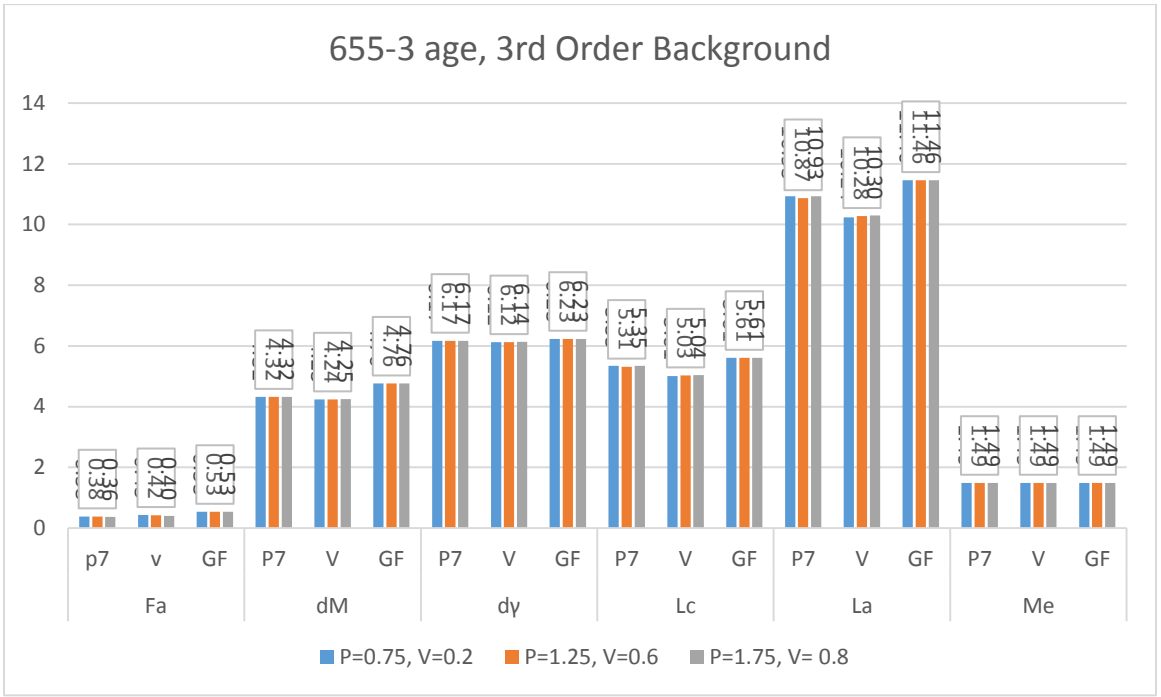

Figure 4-10: Aromaticity and Crystallite Parameters for Sample 655-3 Calculated Using Pearson VII, Pseudo-Voigt and GFF with 3rd Order Background.

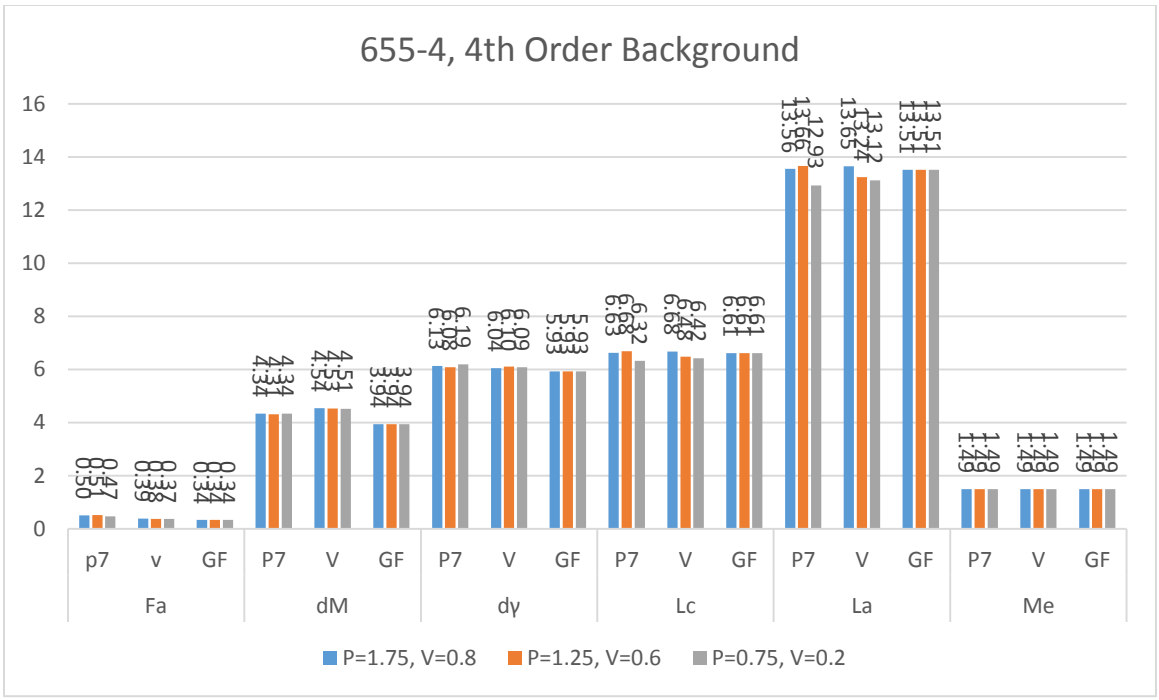

Figure 4-11: Aromaticity and Crystallite Parameters for Sample 655-4 Calculated Using Pearson VII, Pseudo-Voigt And GFF with 4th Order Background.

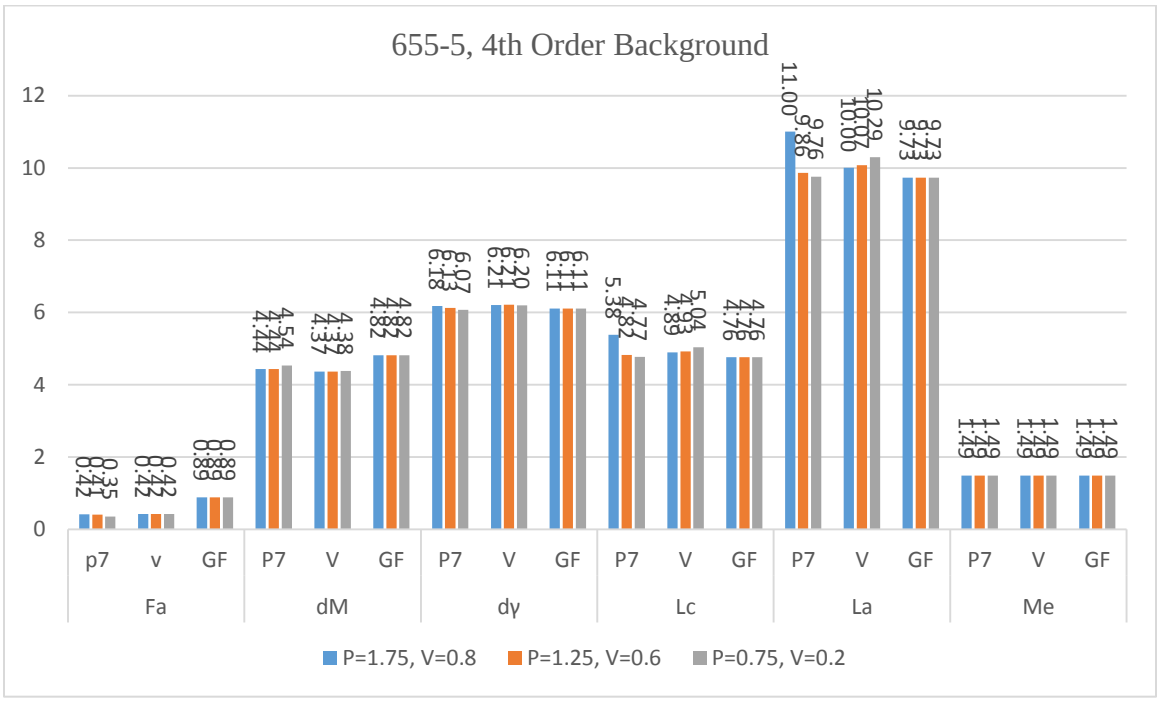

Figure 4-12: Aromaticity and Crystallite Parameters for Sample 655-5 Calculated Using Pearson VII, Pseudo-Voigt and GFF with 4th Order Background.

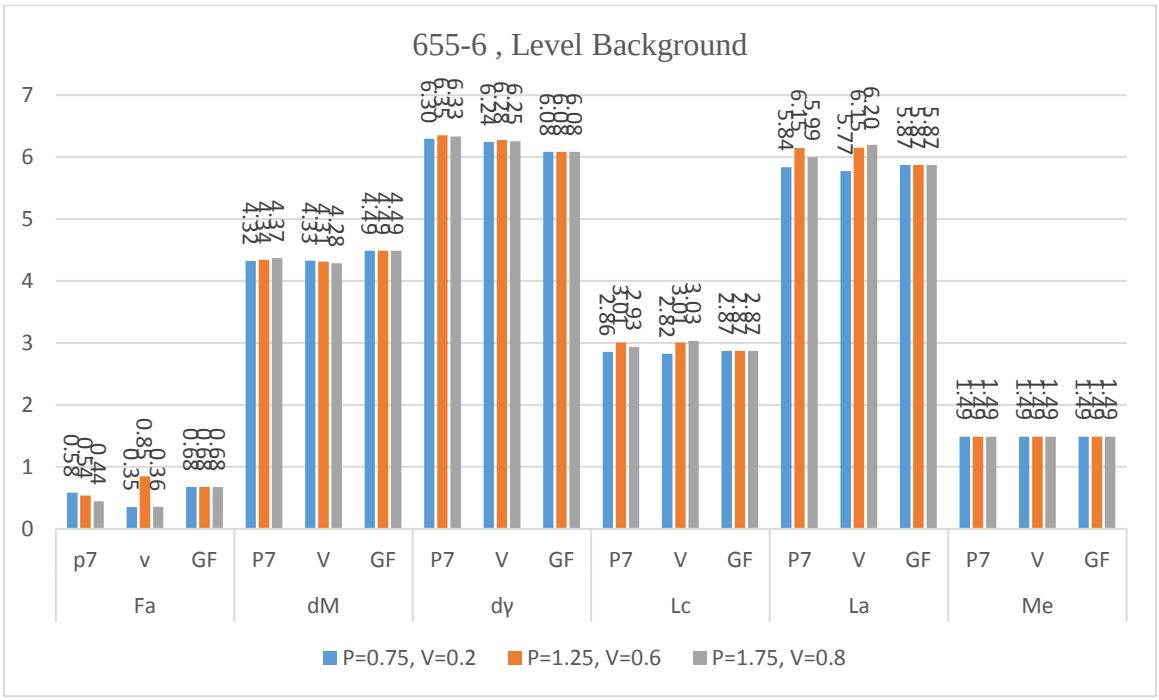

Figure 4-13: Aromaticity and Crystallite Parameters for Sample 655-6 Calculated Using Pearson VII, Pseudo-Voigt and GFF with Level Background.

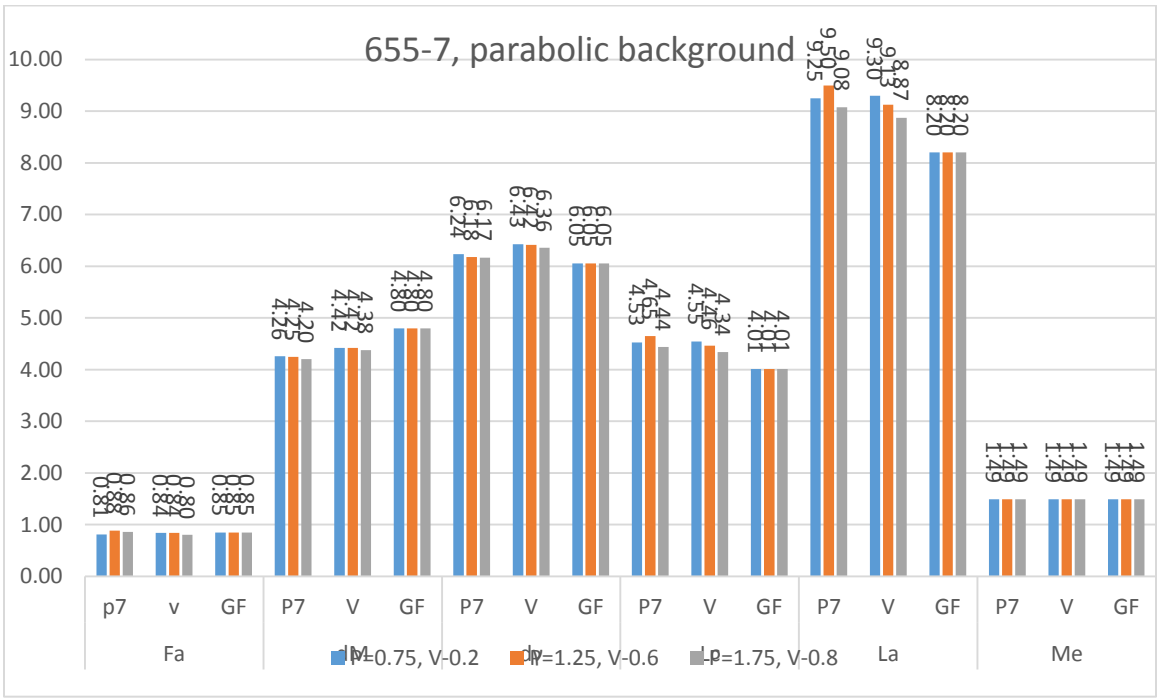

Figure 4-14: Aromaticity and Crystallite Parameters for Sample 655-7 Calculated Using Pearson VII, Pseudo-Voigt and GFF with Parabolic Background.

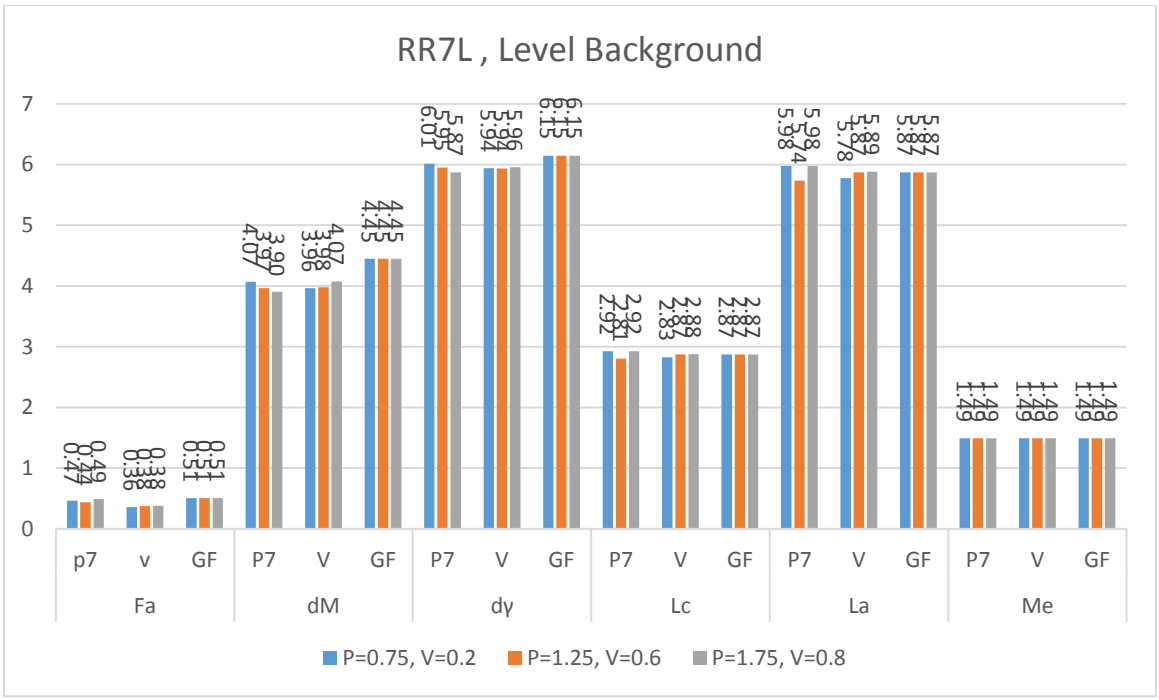

Figure 4-15: Aromaticity and Crystallite Parameters for Sample RR7L Calculated Using Pearson VII, Pseudo-Voigt and GFF with Level Background.

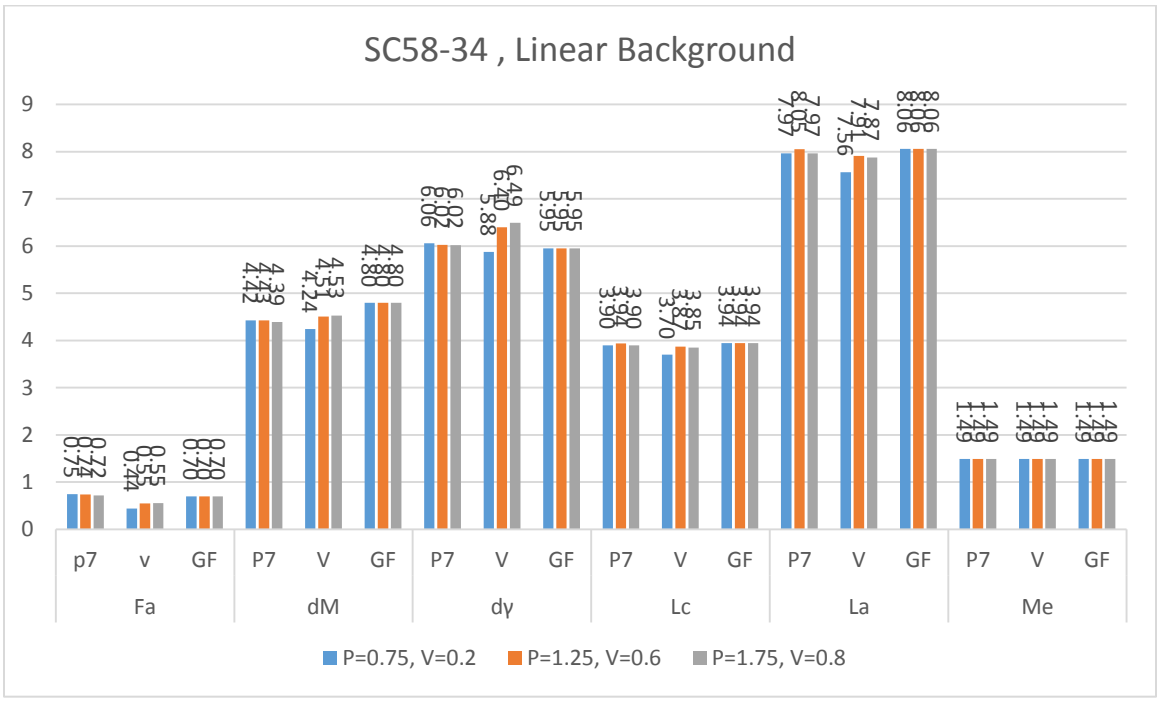

Figure 4-16: Aromaticity and Crystallite Parameters for Sample SC58-34 Calculated Using Pearson VII, Pseudo-Voigt and GFF with 4th Order Background

With Pearson VII and Pseudo-Voigt, aromaticity (f_a) for 655-2, 655-5 and RR7L had approximately average values of 0.5, and 0.4 for 655-3, 655-4 and 655-6; whereas both samples 655-7 and SC58-34 had higher values of 0.84 and 0.6 respectively. Using GFF shows that the data fits were found to be poor since it lacks applying backgrounds and thus results mostly came out to be similar in only one background. An instance of how poor the fit in GFF is, in sample 655-5 which does look, from the appearance of the XRD profile, as apparently having a large γ contribution. However, when using GFF the (002)peak becomes very broad and hence the γ contribution becomes smaller, making f_a in the range of 0.8, while the Pearson VII and Pseudo-Voigt give consistent aromaticity of approximately 0.5. In addition, using the crystallite parameter of the interlayer distance (L_a) had higher average values from GFF of 11.46 in sample (655-3) compared to 10.9 and 10.2 from Pearson VII and pseudo-Voigt. In contrast, sample (655-7) had lower value of (L_a) from GFF compared to Pearson VII and pseudo-Voigt. However, the rest of the results for all other samples show more consistency. The lower aromaticity values for 655-5 indicates that a very distorted x-ray diffraction pattern at low angles that has a strong impact on the quality of the fit. For the rest of the samples, attempts at fitting an individual peak gave an aromaticity with approximately similar results with an error of ±0.5.

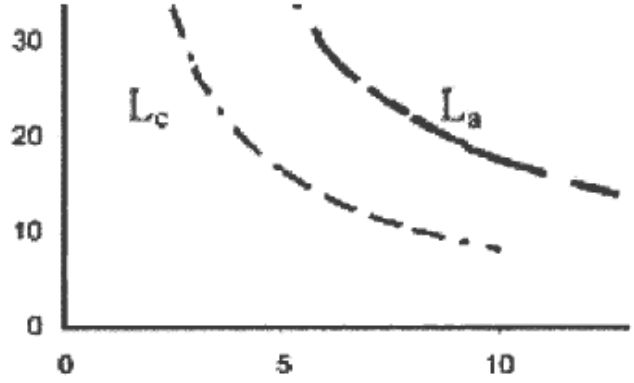

Figure 4-17: Modified Figure of Relationship Showing Crystalline Dimension (Vertical) Versus Bandwidth (Horizontal) (Anderson et al., 2005).

From Figure 4.17, we can assert that the two key parameters for finding crystallite size are L_c and L_a, despite their sensitivity to FWHM. Specifically, L_c shows sensitivity to even minor alterations in γ, such as, for instance, modifying $2\theta = 5°$ to $2\theta = 6°$ cuts the height of the stack in half (i.e., 1.5 nm from 3.0 nm). However, data involving sheet diameter appear to be not quite as sensitive; the only parameter affected seems to be the narrow (100) band. At the same time, we can assert that the results differ significantly even terms of trends if the research uses XRD and shifts between Pearson VII and Pseudo-Voigt. As shown in detail in the previous chapter, the fitting procedure can fall victim to hyper-simplification, as graphs generally require non-symmetric (002) peaks to be created through a number of different factors (e.g., noise in the data residue).

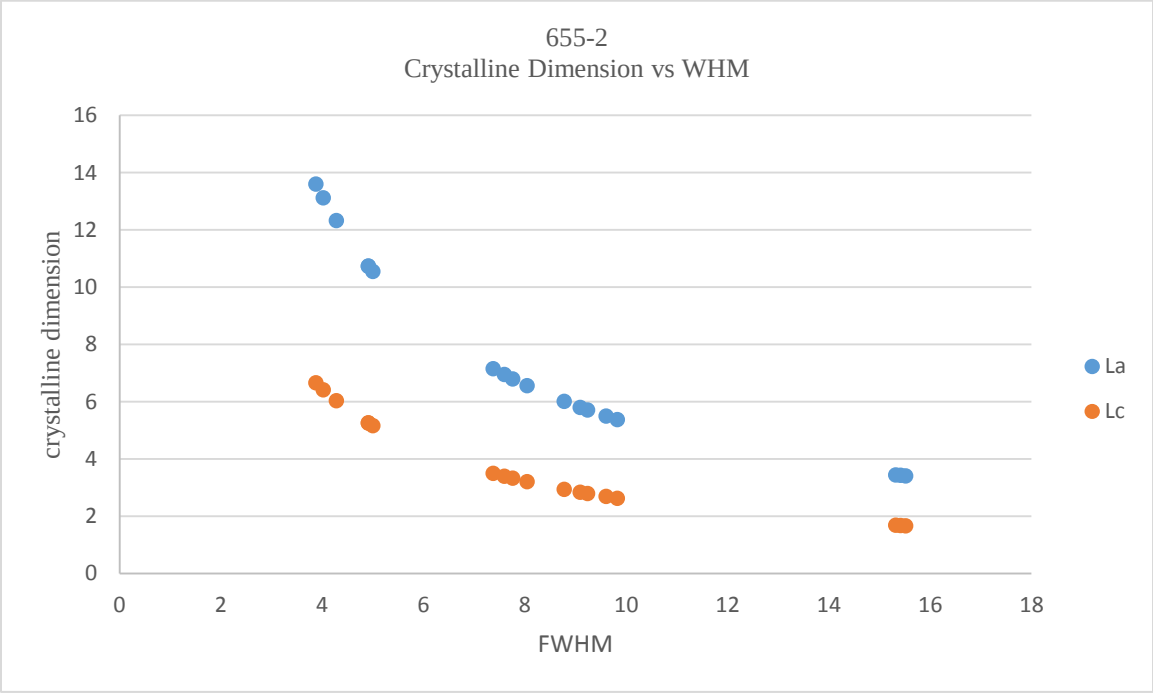

Figure 4-18: Crystalline Dimension Vs FWHM for Sample 655-2.

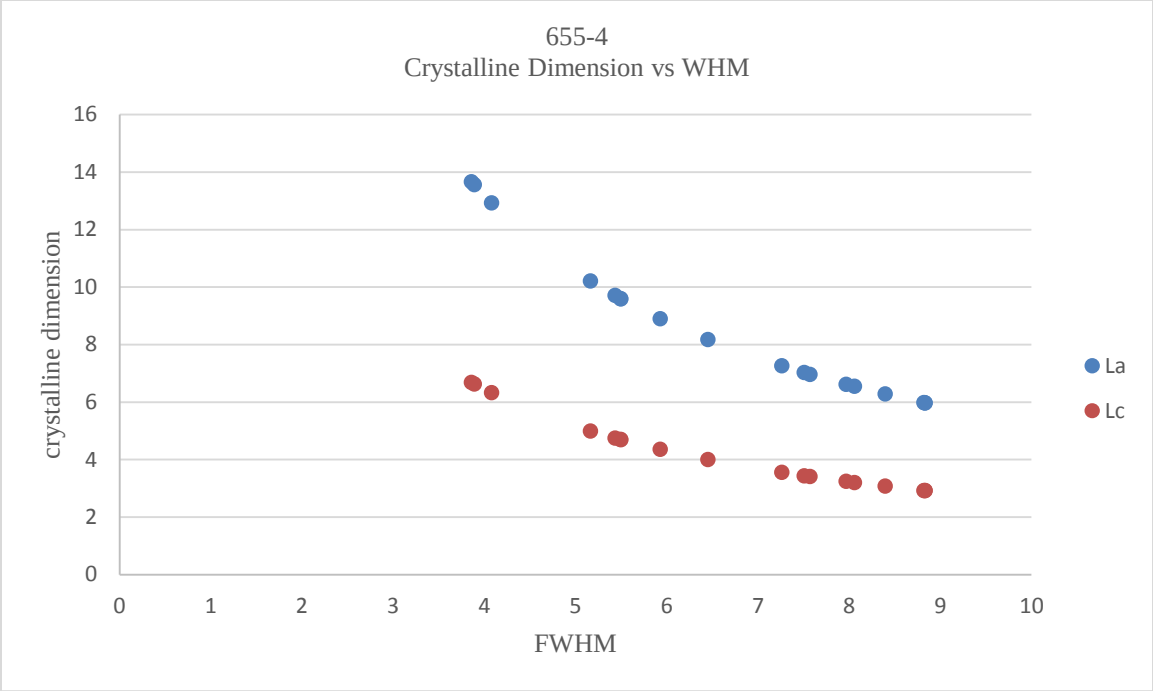

Figure 4-19: Crystalline Dimension Vs FWHM for Sample 655-4.

Chapter 5: Conclusion

In this study, XRD pattern profile fits were compared using the Pearson VII and Pseudo-Voigt functions to find crystallite and aromaticity for a range of values. GFF was applied to model XRD data using the software program Mathematica, but these tools gave generally mixed results for the Pearson VII and Pseudo-Voigt approaches, as outcomes were impacted by asymmetrical XRD data, profile fitting, and peak shape functions.

Eight distinct asphaltene samples originating from diverse sources underwent XRD testing and analysis analyzed, using GFF modeling and the Pearson VII and Pseudo-Voigt functions for raw data. Over a 7-day time period, the samples were steady aged process across all asphalt binders under observation. The results showed a correlation among Pearson VII, pseudo-Voigt, and GFF for some crystallite size parameters ($d\gamma$, La, Lc, Me, f_a, d_m), and the XRD experiments unveiled some features of asphalt binder aggregates.

Peaks were noted and analyzed, showing that crystallinity was enhanced in tandem with asphalt binder aging. Furthermore, even minor modifications of profile angles resulted in shifts in atoms in the planes, thus indicating a direct association between Pearson VII and Pseudo Voigt functions, as well as GFF.

Analysis of the results obtained in this research work indicates that XRD provides insight into the structural and compositional properties of asphalt binders, which is significant in understanding the asphalt binders and asphalt cement pavement. Since asphalt binder XRD results have previously complimented civil engineering tests, as reported by some research studies (Hesp et al., 2007), it is reasonable to expect in the future that asphalt binder XRD results

can possibly play a role in predicting the performance and durability of asphalt in pavement, and asphalt binder conversion into lighter fuels.

In light of the above findings and restrictions, future investigations could look into connections, if any, between value intensity variations and variations within chemical materials, as aging can be connected (at the molecular level) to oxidation. The findings of this present study point to the increasing ability of XRD to accurately describe the properties (both compositional and structural) in asphalt binders, all of which is crucial for grasping how asphalt binders and pavement age in a real-world setting. While XRD lab testing can quite easily complement the civil engineering results from research studies, they cannot necessarily foretell any issues that might arise concerning asphalt-based pavement's durability and performance levels. Therefore, additional research should be performed in this field, first to find the potential problems and then to resolve them using all available tools at hand.

Reference

Akbarzadeh, K., Hammami, A., Kharrat, A., Zhang, D., Allenson, S., Creek, J.,and Mullins, O. C. (2007). Asphaltenes—problematic but rich in potential.*Oilfield Review*, *19*(2), 22-43.

Alexander, L. E., and Sommer, E. C. (1957). Systematic analysis of carbon black structures. The Journal of Physical Chemistry, 60(12), 1646-1649.

Ali, L. H., and Al-Ghannam, K. A. (1981). Investigations into asphaltenes in heavy crude oils. I. Effect of temperature on precipitation by alkane solvents. Fuel, 60(11), 1043-1046.

Al-Muhareb, E. M., Karaca, F., Morgan, T. J., Herod, A. A., Bull, I. D., and Kandiyoti, R. (2006). Size exclusion chromatography for the unambiguous detection of aliphatics in fractions from petroleum vacuum residues, coal liquids, and standard materials, in the presence of aromatics. Energy and fuels, 20(3), 1165-1174.

Al-Muhareb, E., Morgan, T. J., Herod, A. A., and Kandiyoti, R. (2007). Characterization of petroleum asphaltenes by size exclusion chromatography, UV-fluorescence and mass spectrometry. Petroleum science and technology, 25(1-2), 81-91.

Al-Sahhaf, T. A., Fahim, M. A., and Elkilani, A. S. (2002). Retardation of asphaltene precipitation by addition of toluene, resins, deasphalted oil and surfactants. Fluid phase equilibria, 194, 1045-1057.

Altgelt, K. H. (1993). Composition and analysis of heavy petroleum fractions. CRC Press.

Altgelt, K. H., and Harle, O. L. (1975). The effect of asphaltenes on asphalt viscosity. Industrial and Engineering Chemistry Product Research and Development, 14(4), 240-246.

Alvarez, A. G., Martınez-Escandell, M., Molina-Sabio, M., and Rodrıguez-Reinoso, F. (1999). Pyrolysis of petroleum residues: analysis of semicokes by X-ray diffraction. Carbon, 37(10), 1627-1632.

Ancheyta, J., Centeno, G., Trejo, F., Marroquin, G., Garcia, J. A., Tenorio, E., and Torres, A. (2002). Extraction and characterization of asphaltenes from different crude oils and solvents. Energy and Fuels, 16(5), 1121-1127.

Andersen, S.I. (1990). Association of petroleum asphaltenes and related molecular—study on interactions and phase equilibria. PhD thesis, Technical University of Denmark.

Andersen, S.I. 1994. Dissolution of solid Boscan asphaltenes in mixed solvents. Fuel Sci. Tech. Int. 12 (11–12): 1551–1577.

Andersen, S.I. and Birdi, K.S. (1990). Influence of temperature and solvent on the precipitation of asphaltenes. Fuel Sci. Tech. Int. 8 (6): 593–615.

Andersen, S.I. and Speight, J.G. (2001). Petroleum resins: Separation, character, and role in petroleum. Petrol. Sci. Tech. 19 (1–2): 1–34.

Andersen, S.I. and Stenby, E.H. (1996). Thermodynamics of asphaltene precipitation and dissolution investigation of temperature and solvent effects. Fuel Sci. Tech. Int. 14 (1–2): 231–287.

Andersen, S.I., Jensen, J.O., and Speight, J.G. 2005. X-ray diffraction of subfractions of petroleum asphaltenes. Energy Fuels. 19 (6): 2371–2377.

Ascanius, B.E., Merino-Garcia, D., and Andersen, S.I. 2004. Analysis of asphaltenes subfractionated by N-methyl-2-pyrrolidone. Energy Fuels. 18 (6): 1827–1831.

Aske, N., Kallevik, H., and Sj.blom, J. 2001. Determination of saturate, aromatic, resin, and asphaltenic (SARA) components in crude oils by means of infrared and nearinfrared spectroscopy. Energy Fuels. 15 (5): 1304–1312.

ASTM, D. (1988). 4124, Standard Test Method for separation of asphalt into four fractions. American Society for Testing and Material: Philadelphia.

ASTM, D. (1990). 3279 Standard test method for n-heptane insolubles. American Society for Testing and Materials, Pittsburgh, PA, 4, 305-7.

Babu, V. S., and Seehra, M. S. (1996). Modeling of disorder and X-ray diffraction in coal-based graphitic carbons. Carbon, 34(10), 1259-1265.

Bansal, V., Krishna, G. J., Chopra, A., and Sarpal, A. S. (2007). Detailed hydrocarbon characterization of RFCC feed stocks by NMR spectroscopic techniques. Energy and fuels, 21(2), 1024-1029.

Bardon, C., Barre, L., Espinat, D., Guille, V., Li, M. H., Lambard, J., and Zemb, T. (1996). The colloidal structure of crude oils and suspensions of asphaltenes and resins. Fuel Science and Technology International, 14(1-2), 203-242.

Barre, L., Espinat, D., Rosenberg, E., and Scarsella, M. (1997). Colloidal structure of heavy crudes and asphaltene soltutions. Revue de l'Institut Français du Pétrole, 52(2), 161-175.

Bartholdy, J., Lauridsen, R., Mejlholm, M., and Andersen, S. I. (2001). Effect of hydrotreatment on product sludge stability. Energy and fuels, 15(5), 1059-1062.

Bartle, K. D., Mulligan, M. J., Taylor, N., Martin, T. G., and Snape, C. E. (1984). Molecular mass calibration in size-exclusion chromatography of coal derivatives. Fuel, 63(11), 1556-1560.

Bearsley, S., Forbes, A., and G HAVERKAMP, R. (2004). Direct observation of the asphaltene structure in paving- grade bitumen using confocal laser- scanning microscopy. Journal of microscopy, 215(2), 149-155.

Beck, J., Svrcek, W., and Yarranton, H. (2005). Hysteresis in asphaltene precipitation and redissolution. Energy Fuels. 19 (3): 944–947.

Behar, E., Barreau, A., Vellut, D., and Jose, J. (1998). Comparative Ebulliometry: a Simple, Reliable Technique for Accurate Measurement of the Number Average Molecular Weight of Macromolecules. Preliminary Studies on Heavy Crude Fractions. Revue de l'Institut Français du Pétrole, 53(6), 839-855.

Behrouzi, M., and Luckham, P. F. (2008). Limitations of size-exclusion chromatography in analyzing petroleum asphaltenes: A proof by atomic force microscopy. Energy and Fuels, 22(3), 1792-1798.

Bennett, B., and Love, G. D. (2000). Release of organic nitrogen compounds from kerogen via catalytic hydropyrolysis. Geochemical Transactions, 1(1), 61.

Binnig, G., Quate, C. F., and Gerber, C. (1986). Atomic force microscope. Physical review letters, 56(9), 930.

Boduszynski, M. M. (1987). Composition of heavy petroleums. 1. Molecular weight, hydrogen deficiency, and heteroatom concentration as a function of atmospheric equivalent boiling point up to 1400. Degree. F (760. degree. C). Energy and Fuels, 1(1), 2-11.

Bollet, C., Escalier, J. C., Souteyrand, C., Caude, M., and Rosset, R. (1981). Rapid separation of heavy petroleum products by high-performance liquid chromatography. Journal of Chromatography A, 206(2), 289-300.

Borrego, A. G., Blanco, C. G., Prado, J. G., Díaz, C., and Guillén, M. D. (1996). 1H NMR and FTIR spectroscopic studies of bitumen and shale oil from selected Spanish oil shales. Energy and fuels, 10(1), 77-84.

Bouhadda, Y., Bendedouch, D., Sheu, E., and Krallafa, A. (2000). Some preliminary results on a physico-chemical characterization of a Hassi Messaoud petroleum asphaltene. Energy and fuels, 14(4), 845-853.

Boussingault, M. (1837). Memoire sur la Composition des Bitumes. In Annales de Chimie et de Physique (Vol. 64, p. 141).

Bragado, G. C., Guzmán, E. R., and Yacamán, M. J. (2001). Preliminary studies of asphaltene aggregates by low vacuum scanning electron microscopy. Petroleum science and technology, 19(1-2), 45-53.

Brandt, H. C. A., Hendriks, E. M., Michels, M. A. J., and Visser, F. (1995). Thermodynamic modeling of asphaltene stacking. The Journal of Physical Chemistry, 99(26), 10430-10432.

Brauman, J. I. (2000). Twist and fluoresce. Science, 290(5490), 286-287.

Briant, J. and Hotier, G. (1983). Research on the state of asphaltenes in hydrocarbon mixtures: Size of molecular clusters (in French). Oil Gas Sci. Tech.–Rev. IFP. 38 (1): 83–100.

Browarzik, D., Kabatek, R., Kahl, H., and Laux, H. (2002). Flocculation of asphaltenes at high pressure. II. Calculation of the onset of flocculation. Petrol. Sci. Tech. 20 (3-4): 233–249.

Buenrostro-Gonzalez, E., Andersen, S. I., Garcia-Martinez, J. A., and Lira-Galeana, C. (2002). Solubility/molecular structure relationships of asphaltenes in polar and nonpolar media. Energy and Fuels, 16(3), 732-741.

Buenrostro-Gonzalez, E., Espinosa-Pena, M., Andersen, S. I., and Lira-Galeana, C. (2001). Characterization of asphaltenes and resins from problematic Mexican crude oils. Petroleum science and technology, 19(3-4), 299-316.

Buenrostro-Gonzalez, E., Groenzin, H., Lira-Galeana, C., and Mullins, O. C. (2001). The overriding chemical principles that define asphaltenes. Energy and Fuels, 15(4), 972-978.

Calemma, V., Iwanski, P., Nali, M., Scotti, R., and Montanari, L. (1995). Structural characterization of asphaltenes of different origins. Energy and Fuels, 9(2), 225-230.

Calemma, V., Rausa, R., D'Anton, P., and Montanari, L. (1998). Characterization of asphaltenes molecular structure. Energy and Fuels, 12(2), 422-428.

Camacho-Bragado, G. A., Santiago, P., Marin-Almazo, M., Espinosa, M., Romero, E. T., Murgich, J., ... and Jose-Yacaman, M. (2002). Fullerenic structures derived from oil asphaltenes. Carbon, 40(15), 2761-2766.

Carbognani, L., Orea, M., and Fonseca, M. (1999). Complex nature of separated solid phases from crude oils. Energy and fuels, 13(2), 351-358.

Carnahan, N. F., Salager, J. L., Antón, R., and Dávila, A. (1999). Properties of resins extracted from Boscan crude oil and their effect on the stability of asphaltenes in Boscan and Hamaca crude oils. Energy and Fuels, 13(2), 309-314.

Cartz, L., Diamond, R., and Hirsch, P. B. (1956). New X-ray data on coals. Nature, 177(4507), 500-502.

Centeno, G., Trejo, F., Ancheyta, J., and Carlos, A. (2004). Precipitation of asphaltenes from Maya crude in a pressurized system. J. Mex, 186-195.

Champagne, P. J., Manolakis, E., and Ternan, M. (1985). Molecular weight distribution of Athabasca bitumen. Fuel, 64(3), 423-425.

Chiang, S. (1997). Scanning tunneling microscopy imaging of small adsorbed molecules on metal surfaces in an ultrahigh vacuum environment. Chemical reviews, 97(4), 1083-1096.

Christensen Jr, D. W., and Bonaquist, R. (2002). Use of strength tests for evaluating the rut resistance of asphalt concrete. Journal of the Association of Asphalt Paving Technologists, 71.

Christy, A. A., Dahl, B., and Kvalheim, O. M. (1989). Structural features of resins, asphaltenes and kerogen studied by diffuse reflectance infrared spectroscopy. Fuel, 68(4), 430-435.

Christy, A. A., Dahl, B., and Kvalheim, O. M. (1989). Structural features of resins, asphaltenes and kerogen studied by diffuse reflectance infrared spectroscopy. Fuel, 68(4), 430-435.

Coelho, R. R., Hovell, I., Moreno, E. L., de Souza, A. L., and Rajagopal, K. (2007). Characterization of functional groups of asphaltenes in vacuum residues using molecular modelling and FTIR techniques. Petroleum science and technology, 25(1-2), 41-54.

Cowan DO, Drisko RL (1976) Elements of organic photochemistry. Plenum, New York, chap 2.

Dabir, B., Nematy, M., Mehrabi, A. R., Rassamdana, H., and Sahimi, M. (1996). Asphalt flocculation and deposition. III. The molecular weight distribution. Fuel, 75(14), 1633-1645.

De Boer, R. B., Leerlooyer, K., Eigner, M. R. P., and Van Bergen, A. R. D. (1995). Screening of crude oils for asphalt precipitation: theory, practice, and the selection of inhibitors. SPE Production and Facilities, 10(01), 55-61.

Demirbaş, A. (2002). Physical and chemical characterizations of asphaltenes from different sources. Petroleum science and technology, 20(5-6), 485-495.

Dickie, J. P., Haller, M. N., and Yen, T. F. (1969). Electron microscopic investigations on the nature of petroleum asphaltics. Journal of Colloid and Interface Science, 29(3), 475-484.

Domin, M., Herod, A., Kandiyoti, R., Larsen, J. W., Lazaro, M. J., Li, S., and Rahimi, P. (1999). A comparative study of bitumen molecular-weight distributions. Energy and Fuels, 13(3), 552-557.

Donnet, J. B., Ducret, J., Kennel, M., and Papirer, E. (1977). Electron microscopic observations of the morphology of bitumens. Fuel, 56(1), 97-100.

Dorbon, M., Ignatiadis, I., Schmitter, J. M., Arpino, P., Guiochon, G., Toulhoat, H., and Huc, A. (1984). Identification of carbazoles and benzocarbazoles in a coker gas oil and influence of catalytic hydrotreatment on their distribution. Fuel, 63(4), 565-570.

Drushel, H. V. (1978). Trace sulfur determination in petroleum fractions. Analytical Chemistry, 50(1), 76-81.

Durand, E., Clemancey, M., Lancelin, J. M., Verstraete, J., Espinat, D., and Quoineaud, A. A. (2010). Effect of chemical composition on asphaltenes aggregation. Energy and Fuels, 24(2), 1051-1062.

Dutta, P. K., and Holland, R. J. (1984). Acid—base characteristics of petroleum asphaltenes as studied by non-aqueous potentiometric titrations. Fuel, 63(2), 197-201.

Dyer, J. R. (1965). Applications of absorption spectroscopy of organic compounds.

Elsharkawy, A.M., Al-Sahhaf, T.A., Fahim, M.A., and Yarranton, H.W. (2005). Characterization of asphaltenes and resins separated from water-in-crude oil emulsions formed in Kuwaiti oil fields. Paper presented at the 2005 AIChE Annual Meeting. Cincinnati, OH, October 30 to November 4.

Ergun, S., and Tiensuu, V. H. (1959). Alicyclic structures in coals. Nature, 183(4676), 1668-1670.

Espinat, D. (1990). Application of Light, X-Ray and Neutron Diffusion Techniques to the Study of Colloidal Systems. 1. Theoretical Description of 3 Techniques. Revue De L Institut Francais Du Petrole, 45(6), 775-820.

Espinat, D., Ravey, J. C., Guille, V., Lambard, J., Zemb, T., and Cotton, J. P. (1993). Colloidal macrostructure of crude oil studied by neutron and X-ray small angle scattering techniques. Le Journal de Physique IV, 3(C8), C8-181.

Espinat, D., Tchoubar, D., Boulet, R., and Freund, E. (1984). Study of heavy petroleum products by small angle X-ray scattering, in Characterization of Heavy Crude Oils and Petroleum Residues. Editions Technip, Paris, 147–152.

Fahim, M. A., Al-Sahhaf, T. A., and Elkilani, A. S. (2001). Prediction of asphaltene precipitation for Kuwaiti crude using thermodynamic micellization model. Industrial and engineering chemistry research, 40(12), 2748-2756.

Fenistein, D., and Barre, L. (2001). Experimental measurement of the mass distribution of petroleum asphaltene aggregates using ultracentrifugation and small-angle X-ray scattering. Fuel, 80(2), 283-287.

Fenistein, D., Barré, L., Broseta, D., Espinat, D., Livet, A., Roux, J. N., and Scarsella, M. (1998). Viscosimetric and neutron scattering study of asphaltene aggregates in mixed toluene/heptane solvents. Langmuir, 14(5), 1013-1020.

Fortier, R., and Vinson, T. (1998). Low-temperature cracking and aging performance of modified asphalt concrete specimens. Transportation Research Record: Journal of the Transportation Research Board, (1630), 77-86.

Frakman, Z., Ignasiak, T. M., Lown, E. M., and Strausz, O. P. (1990). Oxygen compounds in Athabasca asphaltene. Energy and Fuels, 4(3), 263-270.

Franklin, R. E. (1950). Influence of the bonding electrons on the scattering of X-rays by carbon. Nature, 165(4185), 71-72.

Galal K.A. , and White T.D. (2001). Correlations Between Superpave Asphalt Stiffness and In-Service Pavement Performance, 80th Annual Meeting of the Transportation Research Board, Washington, D.C.

Gawrys, K. L., and Kilpatrick, P. K. (2005). Asphaltenic aggregates are polydisperse oblate cylinders. Journal of colloid and interface science, 288(2), 325-334.

Gawrys, K. L., Matthew Spiecker, P., and Kilpatrick, P. K. (2003). The role of asphaltene solubility and chemical composition on asphaltene aggregation. Petroleum science and technology, 21(3-4), 461-489.

Gawrys, K. L., Spiecker, P. M., and Kilpatrick, P. K. (2002). The role of asphaltene solubility and chemistry on asphaltene aggregation: Conversion chemistry of petroleum residua. Preprints-American Chemical Society. Division of Petroleum Chemistry, 47(4), 332-335.

Gebresellasie, K. (2012). Investigation of asphalt binders by x-ray diffraction using pearson-vii, pseudo-voigt and generalized fermi functions (MSc Thesis, Memorial University of Newfoundland).

Ghloum, E. F., and Oskui, G. P. (2004). Investigation of asphaltene precipitation process for Kuwaiti reservoir. Petroleum science and technology, 22(7-8), 1097-1117.

González, G., Sousa, M. A., and Lucas, E. F. (2006). Asphaltenes precipitation from crude oil and hydrocarbon media. Energy and fuels, 20(6), 2544-2551.

Goual, L., and Firoozabadi, A. (2002). Measuring asphaltenes and resins, and dipole moment in petroleum fluids. AIChE Journal, 48(11), 2646-2663.

Groenzin, H., and Mullins, O. C. (1999). Asphaltene molecular size and structure. The Journal of Physical Chemistry A, 103(50), 11237-11245.

Groenzin, H., and Mullins, O. C. (2000). Molecular size and structure of asphaltenes from various sources. Energy and Fuels, 14(3), 677-684.

Guan, R. L., and Zhu, H. (2007). Study on components in Shengli viscous crude oil by FTIR and UV-Vis spectroscopy. Guang pu xue yu guang pu fen xi= Guang pu, 27(11), 2270-2274.

Guillen, M. D., Blanco, J., Canga, J. S., and Blanco, C. G. (1991). Study of the effectiveness of 27 organic solvents in the extraction of coal tar pitches. Energy and fuels, 5(1), 188-192.

Hammami, A., Ferworn, K. A., Nighswander, J. A., Over°, S. V. E. R. R. E., and Stange, E. (1998). Asphaltenic crude oil characterization: An experimental investigation of the effect of resins on the stability of asphaltenes. Petroleum science and technology, 16(3-4), 227-249.

Hammami, A., Phelps, C. H., Monger-McClure, T., and Little, T. M. (2000). Asphaltene precipitation from live oils: An experimental investigation of onset conditions and reversibility. Energy and Fuels, 14(1), 14-18.

Harvey, J. T., Deacon, J. A., Tsai, B. W., and Monismith, C. L. (1995). Fatigue performance of asphalt concrete mixes and its relationship to asphalt concrete pavement

performance in California. University of California, Berkeley, Institute of Transportation Studies, Asphalt Research Program, CAL/APT Program.

Herod, A. A., and Kandiyoti, R. (1995). Fractionation by planar chromatography of a coal tar pitch for characterisation by size-exclusion chromatography, UV fluorescence and direct-probe mass spectrometry. Journal of Chromatography A, 708(1), 143-160.

Herod, A. A., Bartle, K. D., and Kandiyoti, R. (2007). Characterization of heavy hydrocarbons by chromatographic and mass spectrometric methods: An overview. Energy and Fuels, 21(4), 2176-2203.

Herod, A. A., Bartle, K. D., and Kandiyoti, R. (2007). Characterization of heavy hydrocarbons by chromatographic and mass spectrometric methods: An overview. Energy and Fuels, 21(4), 2176-2203.

Herod, A. A., Lazaro, M. J., Domin, M., Islas, C. A., and Kandiyoti, R. (2000). Molecular mass distributions and structural characterisation of coal derived liquids. Fuel, 79(3), 323-337.

Herzog, P., Tchoubar, D., and Espinat, D. (1988). Macrostructure of asphaltene dispersions by small-angle X-ray scattering. Fuel, 67(2), 245-250.

Hesp, S. A. (2008). Low-Temperature Fractur e in Asphalt Binders, Mastics, and Mixtures. About the Editor, 429.

Hesp, S. A., Iliuta, S., and Shirokoff, J. W. (2007). Reversible Aging in Asphalt Binders†. Energy and Fuels, 21(2), 1112-1121. doi:10.1021/ef060463b

Hirschberg, A., DeJong, L. N. J., Schipper, B. A., and Meijer, J. G. (1984). Influence of temperature and pressure on asphaltene flocculation. Society of Petroleum Engineers Journal, 24(03), 283-293.

Hishiyama, Y., and Nakamura, M. (1995). X-ray diffraction in oriented carbon films with turbostratic structure. Carbon, 33(10), 1399-1403.

Hu, Y. F., and Guo, T. M. (2001). Effect of temperature and molecular weight of n-alkane precipitants on asphaltene precipitation. Fluid Phase Equilibria, 192(1), 13-25.

Huicheng, Z., Yongjie, Y., Wanfu, S., and Jifeng, W. (2007). Struc-tural description of polyaromatic nucleus in residue. China Petroleum Processing and Petrochemical Technology, 3, 35-43.

Hunt, A. (1996). Uncertainties remain in predicting paraffin deposition. Oil and Gas Journal, 94(31), 96-103.

Hunt, J. E., and Winans, R. E. (1999). An overview of resid characterization by mass spectrometry and small angle scattering techniques (No. ANL/CHM/CP-98951). Argonne National Lab., IL (US).

Hunt, J. E., Winans, R. E., and Miller, J. T. (1997). Characterization of asphaltenes from processed resids (No. ANL/CHM/CP--91840; CONF-970443--14). Argonne National Lab., IL (United States).

I. Futheiz, J. Shirokoff and John C. Lewis, Computer controlled X-ray diffraction spectra of heavy oil, Proceedings of the Newfoundland Electrical and Computer Engineering

Conference(NECEC), St. John's, NL, IEEE Newfoundland and Labrador Section, Nov. 10, (2016).

Ibrahim, Y. A., Abdelhameed, M. A., Al-Sahhaf, T. A., and Fahim, M. A. (2003). Structural characterization of different asphaltenes of Kuwaiti origin. Petroleum science and technology, 21(5-6), 825-837.

Institute of Petroleum (Great Britain). (1985). IP Standards for Petroleum and Its Products: Methods for analysis and testing (Vol. 1).

Islas-Flores, C. A., Buenrostro-Gonzalez, E., and Lira-Galeana, C. (2006). Fractionation of petroleum resins by normal and reverse phase liquid chromatography. Fuel, 85(12), 1842-1850.

Jada, A., and Salou, M. (2002). Effects of the asphaltene and resin contents of the bitumens on the water–bitumen interface properties. Journal of Petroleum Science and Engineering, 33(1), 185-193.

Jakobsen, H. J., Sørensen, O. W., Brey, W. S., and Kanyha, P. (1982). The "magic angle" for the differentiation between CH3 and CH multiplicities in 13C spin-echo J-modulation experiments. Journal of Magnetic Resonance (1969), 48(2), 328-335.

Jakobsen, H. J., Sørensen, O. W., Brey, W. S., and Kanyha, P. (1982). The "magic angle" for the differentiation between CH3 and CH multiplicities in 13C spin-echo J-modulation experiments. Journal of Magnetic Resonance (1969), 48(2), 328-335.

Johnson, B. R., Bartle, K. D., Herod, A. A., and Kandiyoti, R. (1997). N-Methyl-2-pyrrolidinone as a mobile phase in the size-exclusion chromatography of coal derivatives. Journal of Chromatography A, 758(1), 65-74.

Kabir, C. S., and Jamaluddin, A. K. M. (1999, January). Asphaltene characterization and mitigation in south Kuwait's Marrat reservoir. In Middle East Oil Show and Conference. Society of Petroleum Engineers.

Karaca, F., Islas, C. A., Millan, M., Behrouzi, M., Morgan, T. J., Herod, A. A., and Kandiyoti, R. (2004). The calibration of size exclusion chromatography columns: molecular mass distributions of heavy hydrocarbon liquids. Energy and fuels, 18(3), 778-788.

Karas, M., and Hillenkamp, F. (1988). Laser desorption ionization of proteins with molecular masses exceeding 10,000 daltons. Analytical chemistry, 60(20), 2299-2301.

Kelemen, S. R., George, G. N., and Gorbaty, M. L. (1990). Direct determination and quantification of sulphur forms in heavy petroleum and coals: 1. The X-ray photoelectron spectroscopy (XPS) approach. Fuel, 69(8), 939-944.

Koinuma, Y., Kushiyama, S., Aizawa, R., Kobayashi, S., Uemasu, I., Mizuno, K., and Shimizu, Y. (1997). Distribution of heteroatoms in asphaltenes separated from Khafji residue before and after hydrotreatment as studied by GPC fractionation. Preprints-American Chemical Society. Division of Petroleum Chemistry, 42(2), 331-335.

Koots, J. A., and Speight, J. G. (1975). Relation of petroleum resins to asphaltenes. Fuel, 54(3), 179-184.

Koral, S. L., Sayegh, S. G., and George, A. E. (1993). Phase equilibria of crude oils using the continuous thermodynamics approach. The Canadian Journal of Chemical Engineering, 71(1), 130-140.

Kumar, M., and Gupta, R. C. (1995). Graphitization study of Indian Assam coking coal. Fuel processing technology, 43(2), 169-176.

Langhoff, S. R., Bauschlicher, C. W., Hudgins, D. M., Sandford, S. A., and Allamandola, L. J. (1998). Infrared spectra of substituted polycyclic aromatic hydrocarbons. The Journal of Physical Chemistry A, 102(9), 1632-1646.

Laux, H., Rahimian, I., and Butz, T. (1997). Thermodynamics and mechanis of stabilization and precipitation of petroleum colloids. Fuel processing technology, 53(1-2), 69-79.

Leon, O., Rogel, E., and Espidel, J. (1999). Structural characterization and self-association of asphaltenes of different origins. American Institute of Chemical Engineers.

Leontaritis, K. J., and Mansoori, G. A. (1988). Asphaltene deposition: a survey of field experiences and research approaches. Journal of Petroleum Science and Engineering, 1(3), 229-239.

Li, W., Morgan, T. J., Herod, A. A., and Kandiyoti, R. (2004). Thin-layer chromatography of pitch and a petroleum vacuum residue: Relation between mobility and molecular size shown by size-exclusion chromatography. Journal of Chromatography A, 1024(1), 227-243.

Lin, M. Y., Sirota, E. B., and Gang, H. (1997, April). Neutron scattering characterization of asphaltene particles. In ABSTRACTS OF PAPERS OF THE AMERICAN CHEMICAL

SOCIETY (Vol. 213, pp. 66-FUEL). 1155 16TH ST, NW, WASHINGTON, DC 20036: AMER CHEMICAL SOC.

Liu, Y. C., Sheu, E. Y., Chen, S. H., and Storm, D. A. (1995). Fractal structure of asphaltenes in toluene. Fuel, 74(9), 1352-1356.

Loeber, L., Sutton, O., Morel, J. V. J. M., Valleton, J. M., and Muller, G. (1996). New direct observations of asphalts and asphalt binders by scanning electron microscopy and atomic force microscopy. Journal of Microscopy, 182(1), 32-39.

Luo, P., and Gu, Y. (2007). Effects of asphaltene content on the heavy oil viscosity at different temperatures. Fuel, 86(7), 1069-1078.

Mansoori, G. A., Jiang, T. S., and Kawanaka, S. (1988). Asphaltene deposition and its role in petroleum production and processing. Arab. J. Sci. Eng, 13(1), 17.

Martinez, M. T., Benito, A. M., and Callejas, M. A. (1997). Thermal cracking of coal residues: kinetics of asphaltene decomposition. Fuel, 76(9), 871-877.

Masson, J. F., Leblond, V., and Margeson, J. (2006). Bitumen morphologies by phase-detection atomic force microscopy. Journal of Microscopy, 221(1), 17-29.

McGennis, R. B., Anderson, R. M., Kennedy, T. W., and Solaimanian, M. (1995). Background of Superpave asphalt mixture design and analysis. Federal Highway Administration.

McKenna, A. M. (2009). Detailed characterization of heavy crude oils and asphaltenes by ultrahigh resolution Fourier transform ion cyclotron resonance mass spectrometry. The Florida State University.

McKenna, A. M. (2009). Detailed characterization of heavy crude oils and asphaltenes by ultrahigh resolution Fourier transform ion cyclotron resonance mass spectrometry. The Florida State University.

Mehrotra, A. K., Sarkar, M., and Svrcek, W. Y. (1985). Bitumen density and gas solubility predictions using the Peng-Robinson equation of state. AOSTRA J. Res, 1(4), 215-229.

Merdrignac, I. and Espinat, D. 2007. Physicochemical characterization of petroleum fractions: The state of the art. Oil Gas Sci. Tech. – Rev. IFP 62 (1): 7–32.

Merdrignac, I., and Espinat, D. (2007). Physicochemical characterization of petroleum fractions: the state of the art. Oil and Gas Science and Technology-Revue de l'IFP, 62(1), 7-32.

Merdrignac, I., Desmazi.res, B., Laprevote, O., and Terrier, P. (2004). Secondary effects in SEC analysis of oil asphaltenes evidenced by cross SEC separations and SEC-MS coupling. Preprints of AIChE 2004 Spring National Meeting, April, New Orleans, LA, 1922–1930.

Merdrignac, I., Quoineaud, A. A., and Gauthier, T. (2006). Evolution of asphaltene structure during hydroconversion conditions. Energy and fuels, 20(5), 2028-2036.

Millan, M., Behrouzi, M., Karaca, F., Morgan, T. J., Herod, A. A., and Kandiyoti, R. (2005). Characterising high mass materials in heavy oil fractions by size exclusion chromatography and MALDI-mass spectrometry. Catalysis today, 109(1), 154-161.

Mitchell, D. L., and Speight, J. G. (1973). The solubility of asphaltenes in hydrocarbon solvents. Fuel, 52(2), 149-152.

Mitra-Kirtley, S., Mullins, O. C., Van Elp, J., George, S. J., Chen, J., and Cramer, S. P. (1993). Determination of the nitrogen chemical structures in petroleum asphaltenes using XANES spectroscopy. Journal of the American Chemical society, 115(1), 252-258.

Miura, K., Mae, K., Li, W., Kusakawa, T., Morozumi, F., and Kumano, A. (2001). Estimation of hydrogen bond distribution in coal through the analysis of OH stretching bands in diffuse reflectance infrared spectrum measured by in-situ technique. Energy and Fuels, 15(3), 599-610.

Monismith, C. L., Epps, J. A., and Finn, F. N. (1985, February). Improved asphalt mix design. In Proceedings, Association of Asphalt Paving Technologists Technical Sessions, San Antonio, Texas (pp. 347-406).

Mordkovich, V. Z., Umnov, A. G., and Inoshita, T. (2000). Nanostructure of laser pyrolysis carbon blacks: observation of multiwall fullerenes. International Journal of Inorganic Materials, 2(4), 347-353.

Morgan, T. J., Millan, M., Behrouzi, M., Herod, A. A., and Kandiyoti, R. (2005). On the Limitations of UV− Fluorescence Spectroscopy in the Detection of High-Mass Hydrocarbon Molecules. Energy and fuels, 19(1), 164-169.

Moschopedis, S. E., and Speight, J. G. (1976). Investigation of hydrogen bonding by oxygen functions in Athabasca bitumen. Fuel, 55(3), 187-192.

Moschopedis, S. E., and Speight, J. G. (1976). Oxygen functions in asphaltenes. Fuel, 55(4), 334-336.

Moschopedis, S. E., Fryer, J. F., and Speight, J. G. (1976). Investigation of asphaltene molecular weights. Fuel, 55(3), 227-232.

Mou, J., Czajkowsky, D. M., Sheng, S. J., Ho, R., and Shao, Z. (1996). High resolution surface structure of E. coli GroES oligomer by atomic force microscopy. FEBS letters, 381(1-2), 161-164.

Mulligan, M. J., Thomas, K. M., and Tytko, A. P. (1987). Functional group fractionation and characterization of tars and pitches: Use of size exclusion chromatography and DMF as the mobile phase. Fuel, 66(11), 1472-1480.

Mullins, O. C. (1995). Sulfur and nitrogen molecular structures in asphaltenes and related materials quantified by XANES spectroscopy. In Asphaltenes (pp. 53-96). Springer US.

Mullins, O. C. (2008). Review of the molecular structure and aggregation of asphaltenes and petroleomics. Spe Journal, 13(01), 48-57.

Mullins, O. C. (2010). The modified Yen model. Energy and Fuels, 24(4), 2179-2207.

Mullins, O. C. (2011). The asphaltenes. Annual Review of Analytical Chemistry, 4, 393-418.

Murgich, J., and Strausz, O. P. (2001). Molecular mechanics of aggregates of asphaltenes and resins of the Athabasca oil. Petroleum Science and Technology, 19(1-2), 231-243.

Murgich, J., Rodríguez, J., and Aray, Y. (1996). Molecular recognition and molecular mechanics of micelles of some model asphaltenes and resins. Energy and Fuels, 10(1), 68-76.

Nahid Siddiqui, M. (2003). Infrared study of hydrogen bond types in asphaltenes. Petroleum science and technology, 21(9-10), 1601-1615.

Nali, M., and A. Manclossi. "Size Exclusion Chromatography and Vapor Pressure Osmometry In The Determination Of Asphaltene Molecular Weight." Fuel science and technology international 13, no. 10 (1995): 1051-1264.

Nellensteyn, F.J. (1933). World Petroleum Congress (3rd Ed.).

Oberlin, A. (1989). High-resolution TEM studies of carbonization and graphitization. Chemistry and physics of carbon, 22, 1-143.

Overfield, R.E., Sheu, E.Y., Sinha, S.K., and Liang, K.S. (1988). SANS study of asphaltenes aggregation. Am. Chem. Soc., Div. Petrol. Chem. – Prepr. 33 (2): 308–313.

Overfield, R.E., Sheu, E.Y., Sinha, S.K., and Liang, K.S. (1989). SANS study of asphaltene aggregation. Fuel Sci. Tech. Int. 7 (5–6): 611–624.

Pasadakis, N., Varotsis, N., and Kallithrakas, N. (2001). The influence of pressure on the asphaltenes content and composition in oils. Petroleum science and technology, 19(9-10), 1219-1227.

Patt, S. L., and Shoolery, J. N. (1982). Attached proton test for carbon-13 NMR. Journal of Magnetic Resonance (1969), 46(3), 535-539.

Paul Maruska, H., and Rao, B. M. (1987). The role of polar species in the aggregation of asphaltenes. Fuel science and technology international, 5(2), 119-168.

Paul-Dauphin, S., Karaca, F., Morgan, T. J., Millan-Agorio, M., Herod, A. A., and Kandiyoti, R. (2007). Probing size exclusion mechanisms of complex hydrocarbon mixtures: the effect of altering eluent compositions. Energy and Fuels, 21(6), 3484-3489.

Pauli, A. T., Branthaver, J. F., Robertson, R. E., Grimes, W., & Eggleston, C. M. (2001). Atomic force microscopy investigation of SHRP asphalts: Heavy oil and resid compatibility and stability. Preprints-American Chemical Society. Division of Petroleum Chemistry, 46(2), 104-110.

Peng, P. A., Morales-Izquierdo, A., Hogg, A., & Strausz, O. P. (1997). Molecular structure of Athabasca asphaltene: sulfide, ether, and ester linkages. Energy & Fuels, 11(6), 1171-1187.

Peramanu, S., Pruden, B. B., and Rahimi, P. (1999). Molecular weight and specific gravity distributions for Athabasca and Cold Lake bitumens and their saturate, aromatic, resin, and asphaltene fractions. Industrial and engineering chemistry research, 38(8), 3121-3130.

Pereira, J. C., López, I., Salas, R., Silva, F., Fernández, C., Urbina, C., and López, J. C. (2007). Resins: the molecules responsible for the stability/instability phenomena of asphaltenes. Energy and fuels, 21(3), 1317-1321.

Pérez-Hernández, R., Mendoza-Anaya, D., Mondragon-Galicia, G., Espinosa, M. E., Rodrıguez-Lugo, V., Lozada, M., and Arenas-Alatorre, J. (2003). Microstructural study of asphaltene precipitated with methylene chloride and n-hexane☆. Fuel, 82(8), 977-982.

Pfeiffer, J. P., and Saal, R. N. J. (1940). Asphaltic bitumen as colloid system. The Journal of Physical Chemistry, 44(2), 139-149.

Pierre, C., Barré, L., Pina, A., and Moan, M. (2004). Composition and heavy oil rheology. Oil and Gas Science and Technology, 59(5), 489-501.

Pillon, L. Z. (2001). Effect of experimental conditions and solvents on the precipitation and composition of asphaltenes. Petroleum science and technology, 19(5-6), 673-683.

Pillon, L. Z. (2001). Effect of experimental conditions and solvents on the precipitation and composition of asphaltenes. Petroleum science and technology, 19(5-6), 673-683.

Pina, A., Mougin, P., and Béhar, E. (2006). Characterisation of asphaltenes and modelling of flocculation–state of the art. Oil and Gas Science and Technology-Revue de l'IFP, 61(3), 319-343.

Pineda, L. A., Trejo, F., and Ancheyta, J. (2007). Correlation between properties of asphaltenes and precipitation conditions. Petroleum science and technology, 25(1-2), 105-119.

Plumail, J. C., Jacquin, Y., Martino, G., and Toulhoat, H. (1983). Effect of the pore size distribution on the activities of alumina supported Co-Mo catalysts in the hydrotreatment of boscan crude. Am. Chem. Soc., Div. Pet. Chem., Prepr.;(United States), 28(CONF-830303-).

Ralston, C. Y., Mitra-Kirtley, S., and Mullins, O. C. (1996). Small population of one to three fused-aromatic ring moieties in asphaltenes. Energy and fuels, 10(3), 623-630.

Ramos, A. C. S., Delgado, C. C., Mohamed, R. S., Almeida, V. R., and Loh, W. (1997, January). Reversibility and inhibition of asphaltene precipitation in Brazilian crude oils. In Latin American and Caribbean Petroleum Engineering Conference. Society of Petroleum Engineers.

Rassamdana, H., Dabir, B., Nematy, M., Farhani, M., and Sahimi, M. (1996). Asphalt flocculation and deposition: I. The onset of precipitation. AIChE Journal, 42(1), 10-22.

Rassamdana, H., Farhani, M., Dabir, B., Mozaffarian, M., and Sahimi, M. (1999). Asphalt flocculation and deposition. V. Phase behavior in miscible and immiscible injections. Energy and fuels, 13(1), 176-187.

Ravey, J. C., Ducouret, G., and Espinat, D. (1988). Asphaltene macrostructure by small angle neutron scattering. Fuel, 67(11), 1560-1567.

Reerink, H., and Lijzenga, J. (1975). Gel-permeation chromatography calibration curve for asphaltenes and bituminous resins. Analytical Chemistry, 47(13), 2160-2167.

Reference

Reynolds, J. G. (1990). Trace metals in heavy crude oils and tar sand bitumens (No. UCRL-JC-104539; CONF-901181--2). Lawrence Livermore National Lab., CA (USA).

Reynolds, J. G., and Biggs, W. R. (1987). Analysis of residuum desulfurization by size exclusion chromatography with element specific detection. American Chemical Society, Division of Petroleum Chemistry, Preprints;(USA), 32(CONF-8704349--).

Ritchie, R. G. S., Roche, R. S., and Steedman, W. (1979). Pyrolysis of Athabasca tar sands: analysis of the condensible products from asphaltene. Fuel, 58(7), 523-530.

Rogel, E. (2000). Simulation of interactions in asphaltene aggregates. Energy and Fuels, 14(3), 566-574.

Rogel, E., and Carbognani, L. (2003). Density estimation of asphaltenes using molecular dynamics simulations. Energy and fuels, 17(2), 378-386.

Rogel, E., Leon, O., Espidel, Y., and Gonzalez, Y. (2001). Asphaltene stability in crude oils. SPE Production and Facilities, 16(02), 84-88.

Rose, K. D., and Francisco, M. A. (1987). Characterization of acidic heteroatoms in heavy petroleum fractions by phase-transfer methylation and NMR spectroscopy. Energy and fuels, 1(3), 233-239.

Rose, K. D., and Francisco, M. A. (1988). A two-step chemistry for highlighting heteroatom species in petroleum materials using carbon-13 NMR spectroscopy. Journal of the American Chemical Society, 110(2), 637-638.

Roux, J. N., Broseta, D., and Demé, B. (2001). SANS study of asphaltene aggregation: concentration and solvent quality effects. Langmuir, 17(16), 5085-5092.

Ruland, W. (1967). X- Ray Studies on Preferred Orientation in Carbon Fibers. Journal of Applied Physics, 38(9), 3585-3589.

Sánchez Berna, A. C., Moran, V. C., Romero Guzmán, E. T., and Yacaman, M. J. (2006). Asphaltene aggregation from vacuum residue and its content of inorganic particles. Petroleum science and technology, 24(9), 1055-1066.

Savvidis, T. G., Fenistein, D., Barré, L., and Béhar, E. (2001). Aggregated structure of flocculated asphaltenes. AIChE journal, 47(1), 206-211.

Schabron, J. F., and Speight, J. G. (1997, April). Correlation between carbon residue and molecular weight. In Abstracts of Papers of the American Chemical Society (Vol. 213, pp. 45-Fuel). 1155 16th St, NW, Washington, Dc 20036: Amer Chemical Soc.

Schmitter, J. M., Ignatiadis, I., Dorbon, M., Arpino, P., Guiochon, G., Toulhoat, H., and Hue, A. (1984). Identification of nitrogen bases in a coker gas oil and influence of catalytic hydrotreat ment on their composition. Fuel, 63(4), 557-564.

Schwager, I., Farmanian, P. A., Kwan, J. T., Weinberg, V. A., and Yen, T. F. (1983). Characterization of the microstructure and macrostructure of coal-derived asphaltenes by nuclear magnetic resonance spectrometry and X-ray diffraction. Analytical chemistry, 55(1), 42-45.

Seidl, P. R., Chrisman, E. C. A. N., Silva, R. C., De Menezes, S. M. C., and Teixeira, M. A. G. (2004). Critical variables for the characterization of asphaltenes extracted from vacuum residues. Petroleum science and technology, 22(7-8), 961-971.

Seki, H., and Kumata, F. (2000). Structural change of petroleum asphaltenes and resins by hydrodemetallization. Energy and fuels, 14(5), 980-985.

Sharma, A., Groenzin, H., Tomita, A., and Mullins, O. C. (2002). Probing order in asphaltenes and aromatic ring systems by HRTEM. Energy and Fuels, 16(2), 490-496.

Sharma, A., Kyotani, T., and Tomita, A. (2000). Comparison of structural parameters of PF carbon from XRD and HRTEM techniques. Carbon, 38(14), 1977-1984.

Sharma, B. K., Sharma, C. D., Bhagat, S. D., and Erhan, S. Z. (2007). Maltenes and asphaltenes of petroleum vacuum residues: physico-chemical characterization. Petroleum science and technology, 25(1-2), 93-104.

Sheremata, J. M., Gray, M. R., Dettman, H. D., and McCaffrey, W. C. (2004). Quantitative molecular representation and sequential optimization of Athabasca asphaltenes. Energy and Fuels, 18(5), 1377-1384.

Sheu, E. Y. (2002). Petroleum asphaltene properties, characterization, and issues. Energy and Fuels, 16(1), 74-82.

Sheu, E. Y. (2002). Petroleum asphaltene properties, characterization, and issues. Energy and Fuels, 16(1), 74-82.

Sheu, E. Y., Liang, K. S., Sinha, S. K., and Overfield, R. E. (1992). Polydispersity analysis of asphaltene solutions in toluene. Journal of Colloid and Interface Science, 153(2), 399-410.

Sheu, E. Y., Maureen, M., Storm, D. A., and DeCanio, S. J. (1992). Aggregation and kinetics of asphaltenes in organic solvents. Fuel, 71(3), 299-302.

Sheu, E. Y., Storm, D. A., and Maureen, M. (1991). Asphaltenes in polar solvents. Journal of non-crystalline solids, 131, 341-347.

Shiraishi, M., Kobayashi, K., and Toyoda, S. (1972). Thermal expansion of interlayer spacing and thermal vibrational displacement of carbon atoms in petroleum coke. Journal of Materials Science, 7(11), 1229-1232.

Shirokoff, J. W., Siddiqui, M. N., and Ali, M. F. (1997). Characterization of the structure of Saudi crude asphaltenes by X-ray diffraction. Energy and Fuels, 11(3), 561-565.

Siddiqui, M. N., Ali, M. F., and Shirokoff, J. (2002). Use of X-ray diffraction in assessing the aging pattern of asphalt fractions. Fuel, 81(1), 51-58.

Sirota, E. B. (2005). Physical structure of asphaltenes. Energy and fuels, 19(4), 1290-1296.

Speight, J. G. (1986). Polynuclear aromatic systems in petroleum. Am. Chem. Soc., Div. Pet. Chem., Gen. Pap., Prepr.;(United States), 31(CONF-860911-).

Speight, J. G. (1987). Initial reactions in the coking of residua. American Chemical Society, Division of Petroleum Chemistry, Preprints;(USA), 32(CONF-8704349--).

Speight, J. G. (1994). Chemical and physical studies of petroleum asphaltenes. Developments in petroleum science, 40, 7-65.

Speight, J. G. (1999). The chemistry and technology of petroleum. CRC press.

Speight, J. G. (2001). Handbook of petroleum analysis John Wiley and Sons. Inc., New York.

Speight, J. G. (2004). Petroleum Asphaltenes-Part 1: Asphaltenes, resins and the structure of petroleum. Oil and gas science and technology, 59(5), 467-477.

Speight, J. G. (2014). The chemistry and technology of petroleum. CRC press.

Speight, J. G., and Moschopedis, S. E. (1981). Chemistry of asphaltenes. Advances in Chemistry series. MJ Comstock series editor. Washington DC, 1, 195.

Speight, J. G., Long, R. B., and Trowbridge, T. D. (1984). Factors influencing the separation of asphaltenes from heavy petroleum feedstocks. Fuel, 63(5), 616-620.

Speight, J.G. (1999). The Chemistry and Technology of Petroleum, 3rd ed., Marcel Dekker, New York, 412–467.

Spiecker, P. M., Gawrys, K. L., and Kilpatrick, P. K. (2003). Aggregation and solubility behavior of asphaltenes and their subfractions. Journal of colloid and interface science, 267(1), 178-193.

Storm, D. A., and Sheu, E. Y. (1995). Characterization of colloidal asphaltenic particles in heavy oil. Fuel, 74(8), 1140-1145.

Storm, D. A., Sheu, E. Y., and DeTar, M. M. (1993). Macrostructure of asphaltenes in vacuum residue by small-angle X-ray scattering. Fuel, 72(7), 977-981.

Strausz, O. P., Mojelsky, T. W., Faraji, F., Lown, E. M., and Peng, P. A. (1999). Additional structural details on Athabasca asphaltene and their ramifications. Energy and Fuels, 13(2), 207-227.

Strausz, O. P., Mojelsky, T. W., Lown, E. M., Kowalewski, I., and Behar, F. (1999). Structural features of Boscan and Duri asphaltenes. Energy and Fuels, 13(2), 228-247.

Strausz, O. P., Peng, P. A., and Murgich, J. (2002). About the colloidal nature of asphaltenes and the MW of covalent monomeric units. Energy and fuels, 16(4), 809-822.

Suelves, I., Islas, C. A., Millan, M., Galmes, C., Carter, J. F., Herod, A. A., and Kandiyoti, R. (2003). Chromatographic separations enabling the structural characterisation of heavy petroleum residues. Fuel, 82(1), 1-14.

Takanohashi, T., Iino, M., and Nakamura, K. (1998). Simulation of interaction of coal associates with solvents using the molecular dynamics calculation. Energy and fuels, 12(6), 1168-1173.

Takeshige, W. (2001). Hydrodynamic shape and size of Khafji asphaltene in benzene. Journal of colloid and interface science, 234(2), 261-268.

Tanaka, R., Hunt, J. E., Winans, R. E., Thiyagarajan, P., Sato, S., and Takanohashi, T. (2003). Aggregates structure analysis of petroleum asphaltenes with small-angle neutron scattering. Energy and fuels, 17(1), 127-134.

Tanaka, R., Sato, E., Hunt, J. E., Winans, R. E., Sato, S., and Takanohashi, T. (2004). Characterization of asphaltene aggregates using X-ray diffraction and small-angle X-ray scattering. Energy and Fuels, 18(4), 1118-1125.

Thiyagarajan, P., Hunt, J. E., Winans, R. E., Anderson, K. B., and Miller, J. T. (1995). Temperature-dependent structural changes of asphaltenes in 1-methylnaphthalene. Energy and Fuels, 9(5), 829-833.

Trejo, F., Ancheyta, J., and Rana, M. S. (2009). Structural characterization of asphaltenes obtained from hydroprocessed crude oils by SEM and TEM. Energy and Fuels, 23(1), 429-439.

Trejo, F., Ancheyta, J., Morgan, T. J., Herod, A. A., and Kandiyoti, R. (2007). Characterization of asphaltenes from hydrotreated products by SEC, LDMS, MALDI, NMR, and XRD. Energy and Fuels, 21(4), 2121-2128.

Warren, B. E. (1941). X-ray diffraction in random layer lattices. Physical Review, 59(9), 693.

Whitson, C. H. (1983). Characterizing hydrocarbon plus fractions. Society of Petroleum Engineers Journal, 23(04), 683-694.

Wiehe, I. A. (1992). A solvent-resid phase diagram for tracking resid conversion. Industrial and engineering chemistry research, 31(2), 530-536.

Wiehe, I. A. (2007). In defense of vapor pressure osmometry for measuring molecular weight. Journal of dispersion science and technology, 28(3), 431-435.

Wilt, B. K., Welch, W. T., and Rankin, J. G. (1998). Determination of asphaltenes in petroleum crude oils by Fourier transform infrared spectroscopy. Energy and fuels, 12(5), 1008-1012.

Xu, Y., Koga, Y., and Strausz, O. P. (1995). Characterization of Athabasca asphaltenes by small-angle X-ray scattering. Fuel, 74(7), 960-964.

Yang, M. G., and Eser, S. (1999). Fractionation and molecular analysis of a vacuum residue asphaltenes. Fuel Chem Am Chem Soc, 44(4), 762-768.

Yarborough, L. (1979). Application of a generalized equation of state to petroleum reservoir fluids.

Yarranton, H. W., and Masliyah, J. H. (1996). Molar mass distribution and solubility modeling of asphaltenes. AIChE Journal, 42(12), 3533-3543.

Yarranton, H. W., Alboudwarej, H., and Jakher, R. (2000). Investigation of asphaltene association with vapor pressure osmometry and interfacial tension measurements. Industrial and engineering chemistry research, 39(8), 2916-2924.

Yen, T. F. (1979). Structural difference between petroleum and coal-derived asphaltenes. Am. Chem. Soc., Div. Pet. Chem., Prepr.;(United States), 24(CONF-790917-(Vol. 24)(No. 4)).

Yen, T. F., Erdman, J. G., and Pollack, S. S. (1961). Investigation of the structure of petroleum asphaltenes by X-ray diffraction. Analytical chemistry, 33(11), 1587-1594.

Zajac, G. W., Gallas, J. M., and Alvarado- Swaisgood, A. E. (1994). Tunneling microscopy verification of an x- ray scattering- derived molecular model of tyrosine- based

melanin. Journal of Vacuum Science and Technology B: Microelectronics and Nanometer Structures Processing, Measurement, and Phenomena, 12(3), 1512-1516.

Zajac, G. W., Sethi, N. K., and Joseph, J. T. (1994). Molecular Imaging Of Petroleum Asphaltenes By Scanning-Tunneling-Microscopy-Verification Of Structure From C-13 And Proton Nuclear-Magnetic-Resonance Data. Scanning Microscopy, 8(3), 463-470.

Zajac, G. W., Sethi, N. K., and Joseph, J. T. (1997). Maya Petroleum Asphaltene Imaging by Scanning Tunneling Microscopy: Verification of Structure From^ 1^ 3C and Proton Nuclear Magnetic Resonance. In PREPRINTS OF SYMPOSIA-DIVISION OF FUEL CHEMISTRY AMERICAN CHEMICAL SOCIETY (Vol. 42, pp. 423-426).

Zhao, S., Kotlyar, L. S., Woods, J. R., Sparks, B. D., Hardacre, K., and Chung, K. H. (2001). Molecular transformation of Athabasca bitumen end-cuts during coking and hydrocracking. Fuel, 80(8), 1155-1163.

Appendex

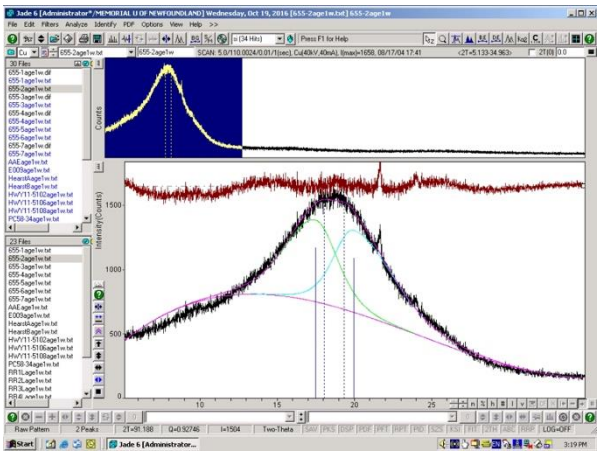

Figure 0-1: Profile Fitting for Sample 655-2 (3rd Order Background, Exp 0.75).

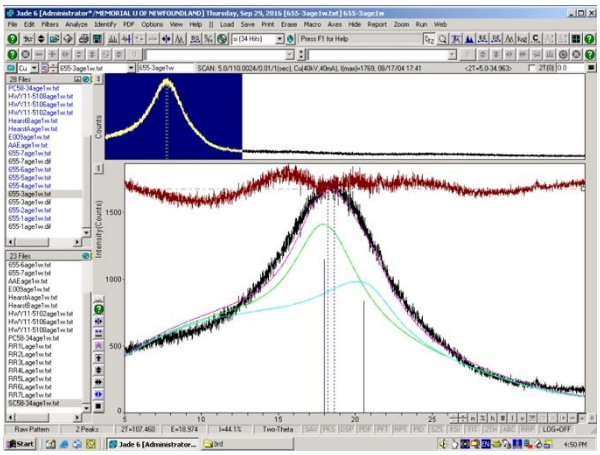

Figure 0-2: Profile Fitting for Sample 655-3 (3rd Order Background, Exp 0.75).

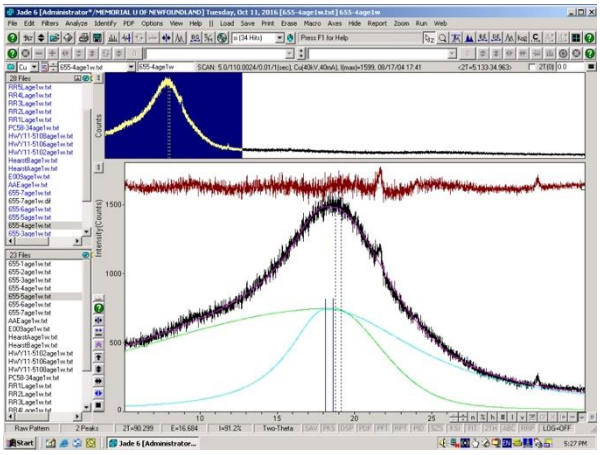

Figure 0-3: Profile Fitting for Sample 655-4 (Fixed Background, Lor 0.2).

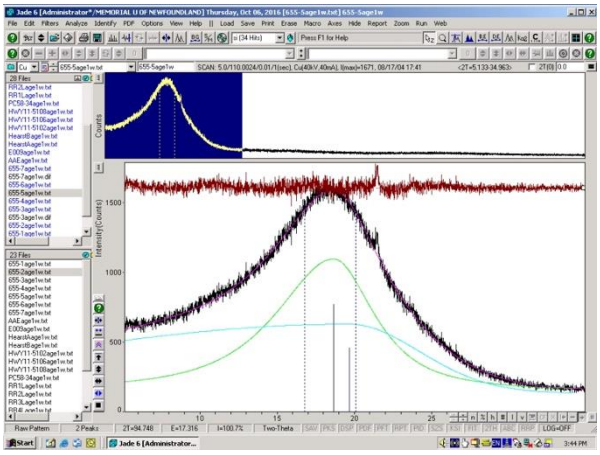

Figure 0-4: Profile Fitting for Sample 655-5 (Level Background, Lor 0.6).

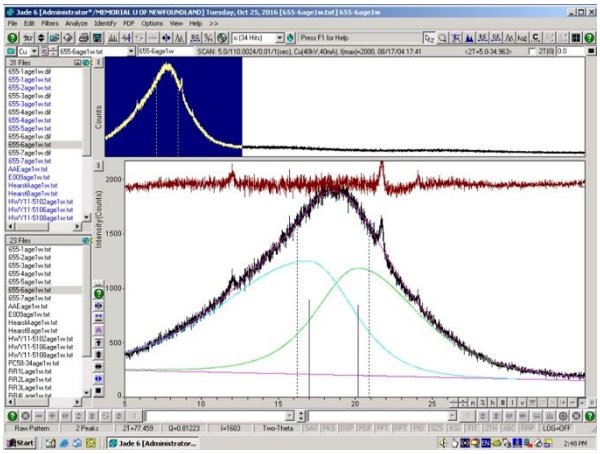

Figure 0-5: Profile Fitting for Sample 655-6 (Linear Background, Exp 1.75).

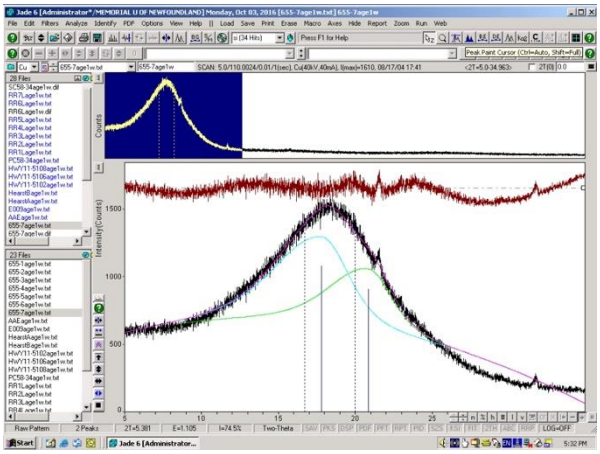

Figure 0-6: Profile Fitting for Sample 655-7 (Parabolic Background, Exp 0.75).

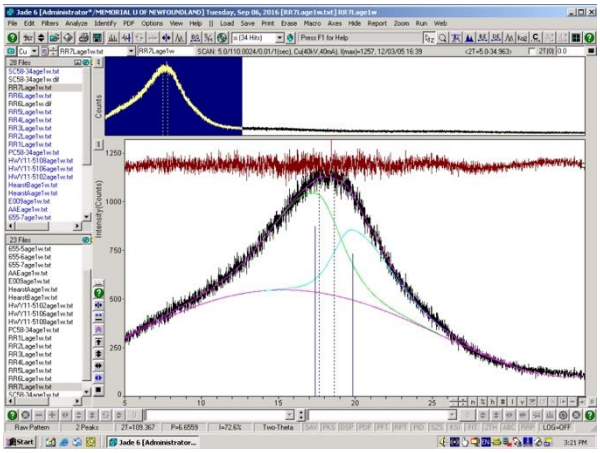

Figure 0-7: Profile Fitting for Sample RR7L (4th Order Background, Exp 1.25).

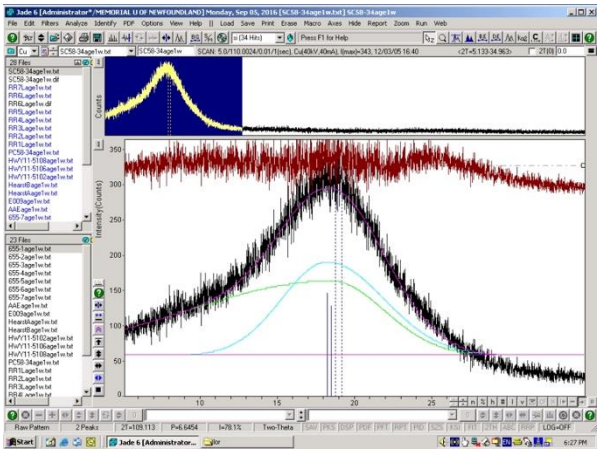

Figure 0-8: Profile Fitting for Sample SC58-34 (Level Background, Lor O.6).

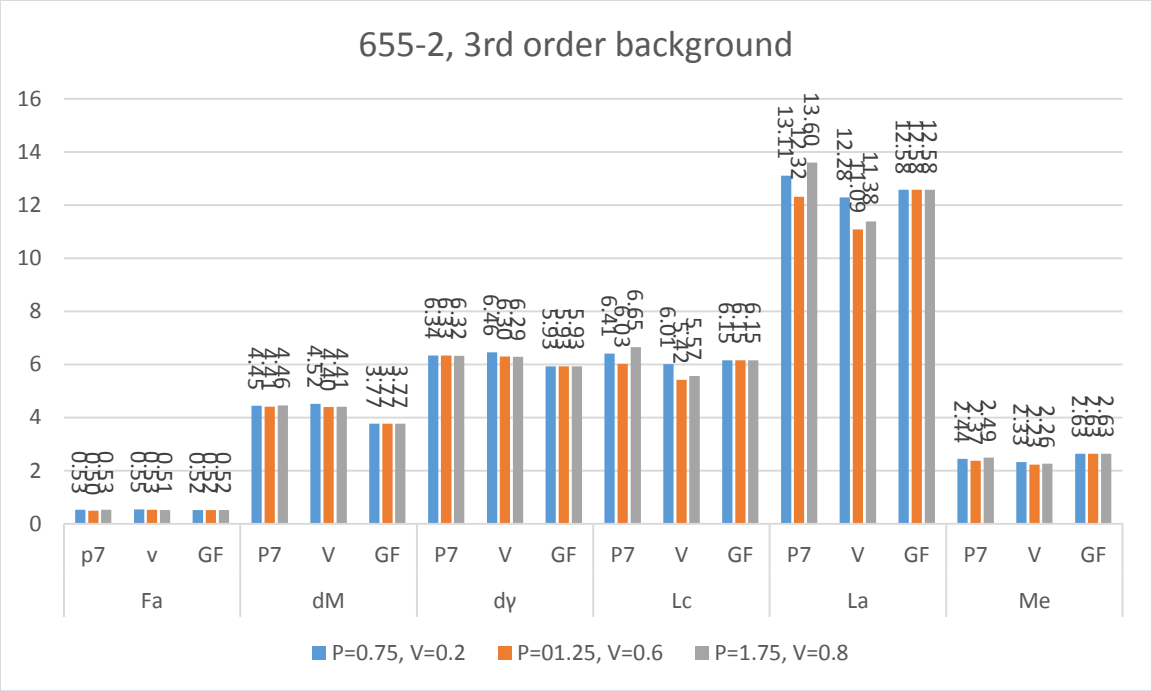

Figure 0-9: Aromaticity and Crystallite Parameters for Sample 655-2 Calculated Using Pearson VII, Pseudo-Voigt and GFF with 3d-Order Background.

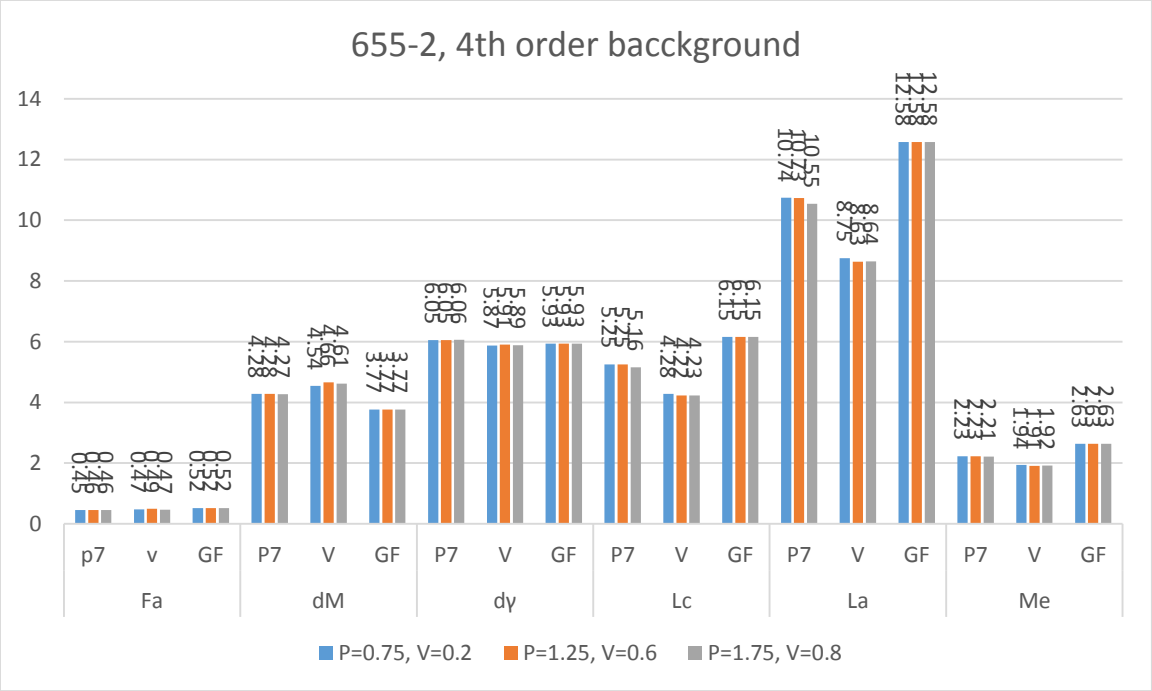

Figure 0-10: Aromaticity and Crystallite Parameters for Sample 655-2 Calculated Using Pearson VII, Pseudo-Voigt and GFF with 4th-Order Background.

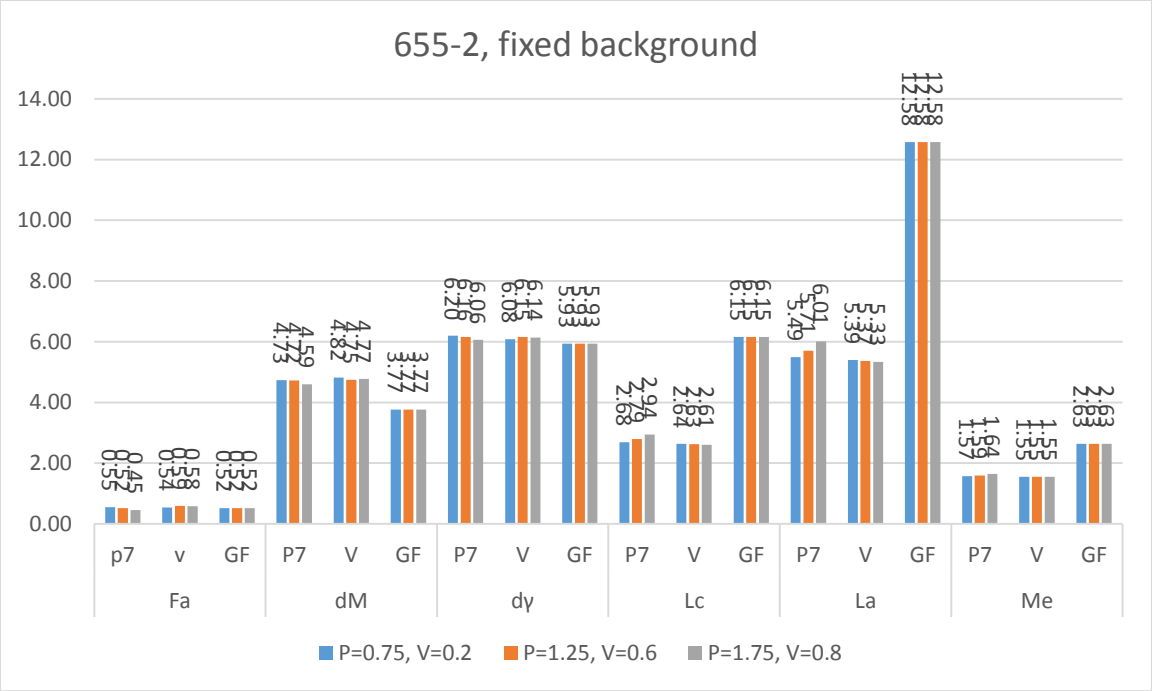

Figure 0-11: Aromaticity and Crystallite Parameters for Sample 655-2 Calculated Using Pearson VII, Pseudo-Voigt and GFF with Fixed Background.

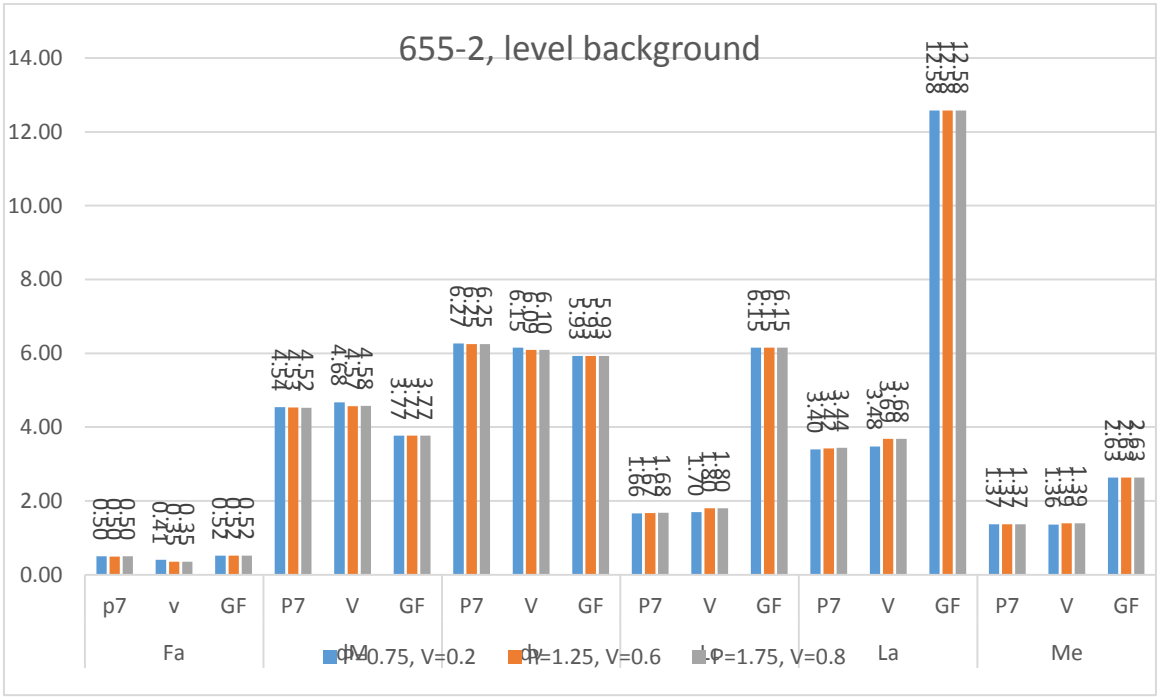

Figure 0-12: Aromaticity and Crystallite Parameters for Sample 655-2 Calculated Using Pearson VII, Pseudo-Voigt and GFF with Level Background.

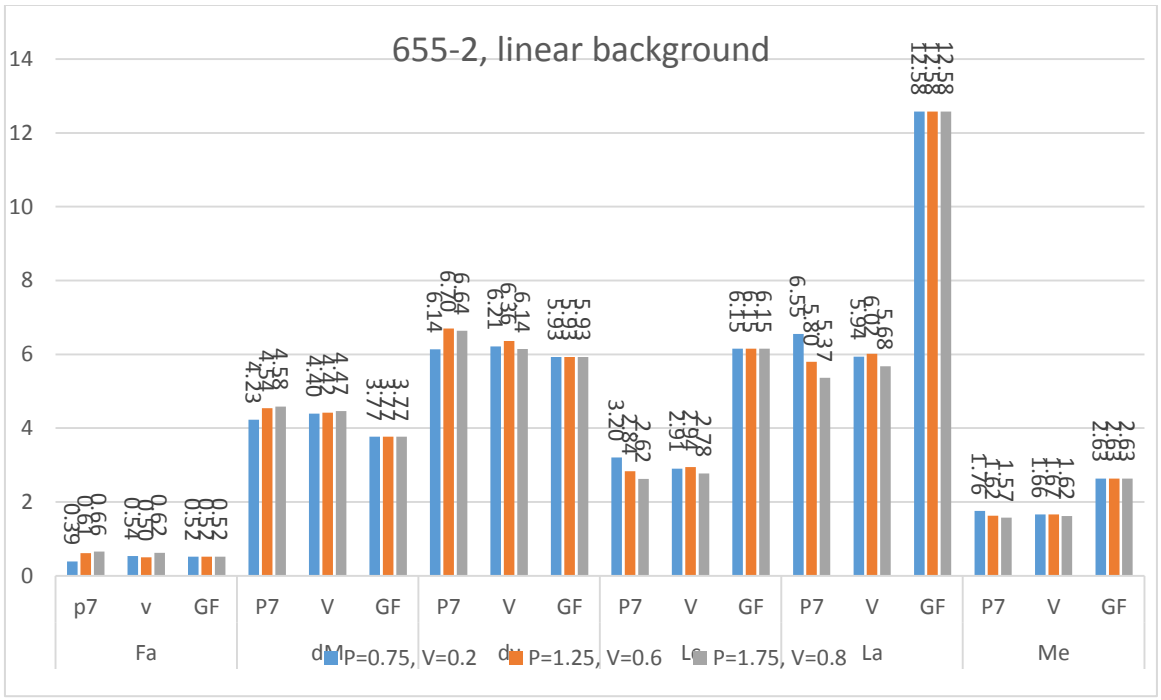

Figure 0-13: Aromaticity and Crystallite Parameters for Sample 655-2 Calculated Using Pearson VII, Pseudo-Voigt and GFF with Linear Background.

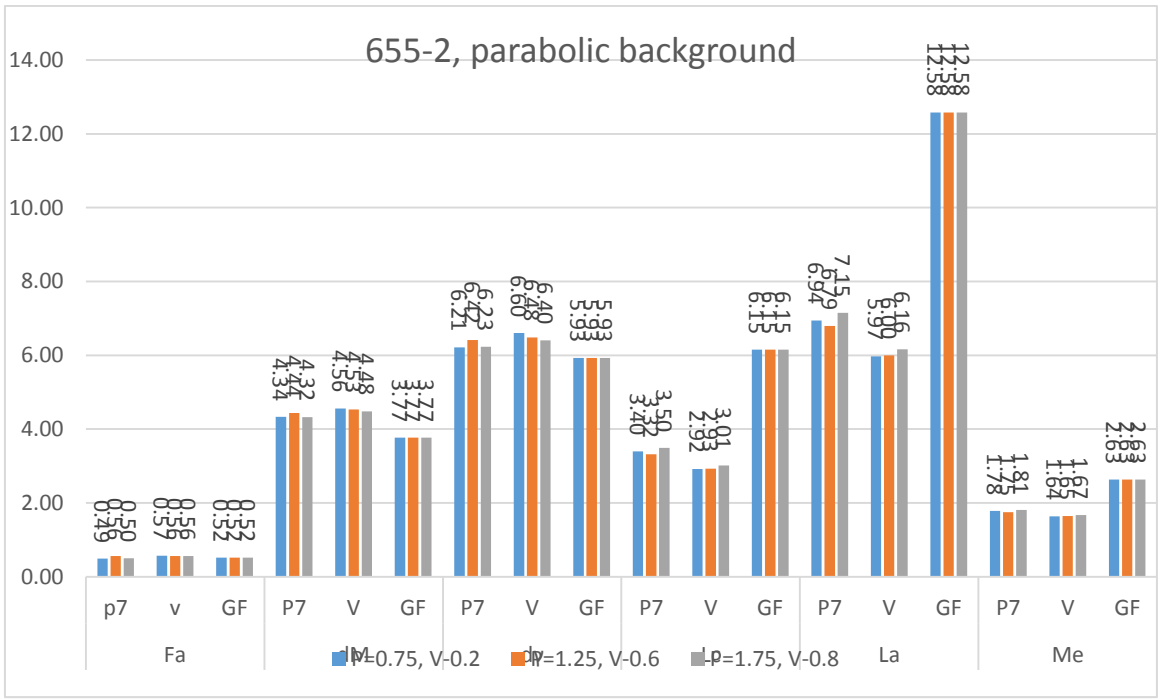

Figure 0-14: Aromaticity and Crystallite Parameters for Sample 655-2 Calculated Using Pearson VII, Pseudo-Voigt and GFF with Parabolic Background.

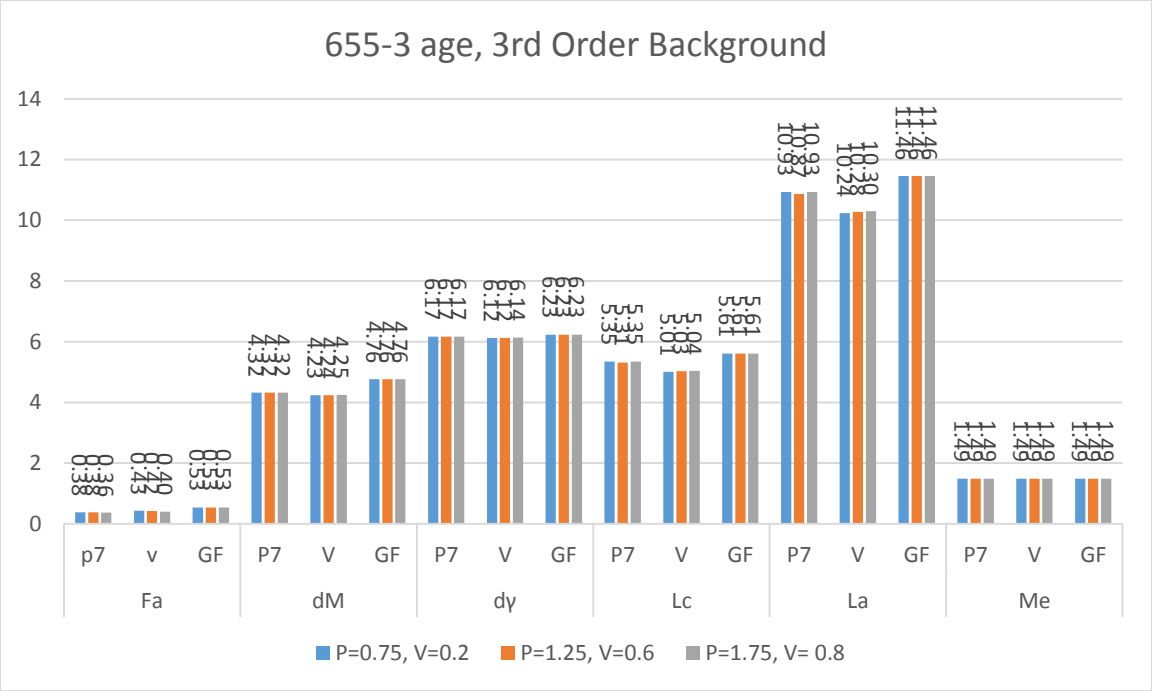

Figure 0-15: Aromaticity and Crystallite Parameters for Sample 655-3 Calculated Using Pearson VII, Pseudo-Voigt and GFF with 3d-Order Background.

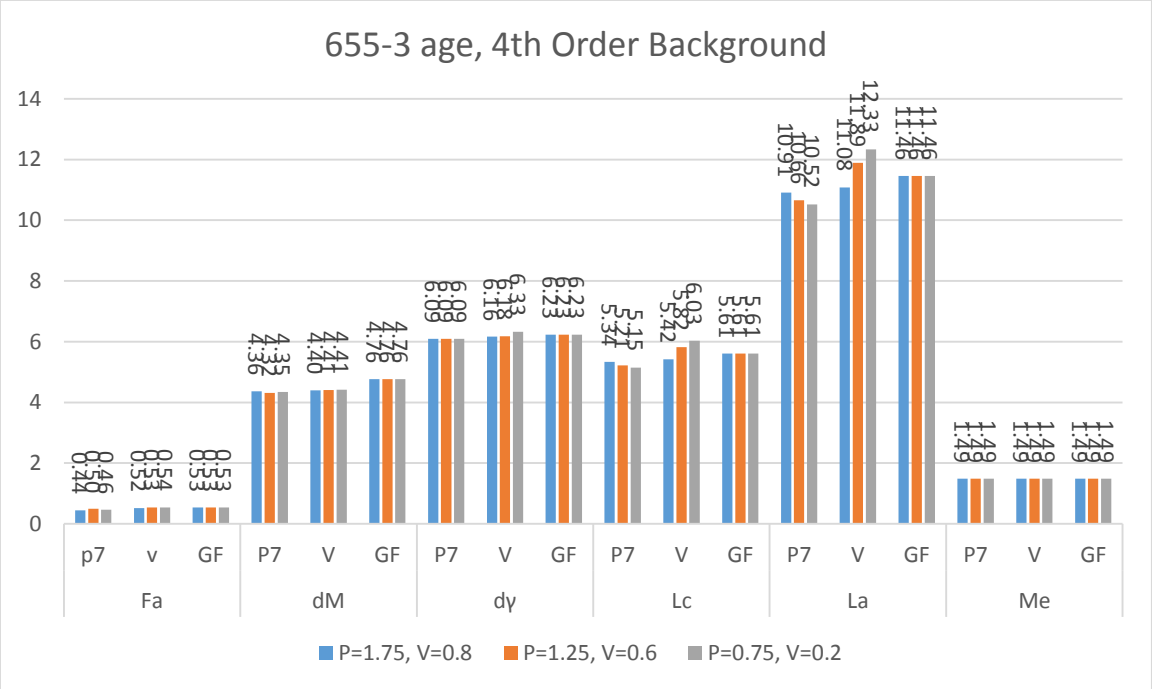

Figure 0-16: Aromaticity and Crystallite Parameters for Sample 655-3 Calculated Using Pearson VII, Pseudo-Voigt and GFF with 4th-Order Background.

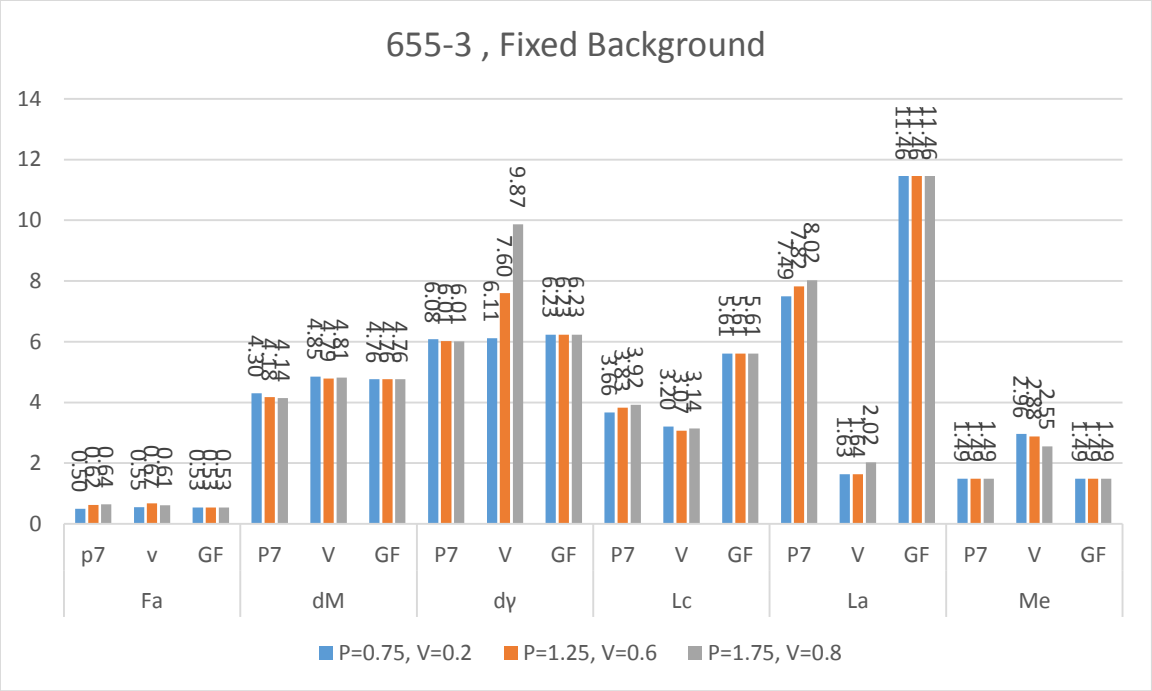

Figure 0-17: Aromaticity and Crystallite Parameters for Sample 655-3 Calculated Using Pearson VII, Pseudo-Voigt and GFF with Fixed Background.

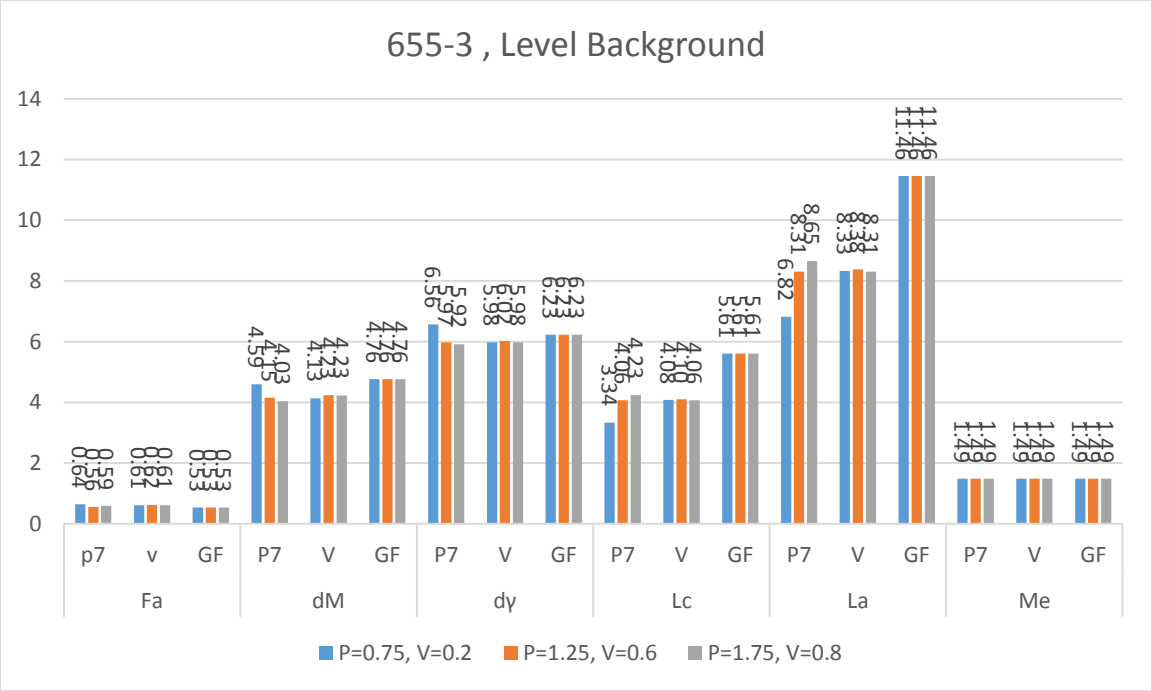

Figure 0-18: Aromaticity and Crystallite Parameters for Sample 655-3 Calculated Using Pearson VII, Pseudo-Voigt and GFF with Level Background.

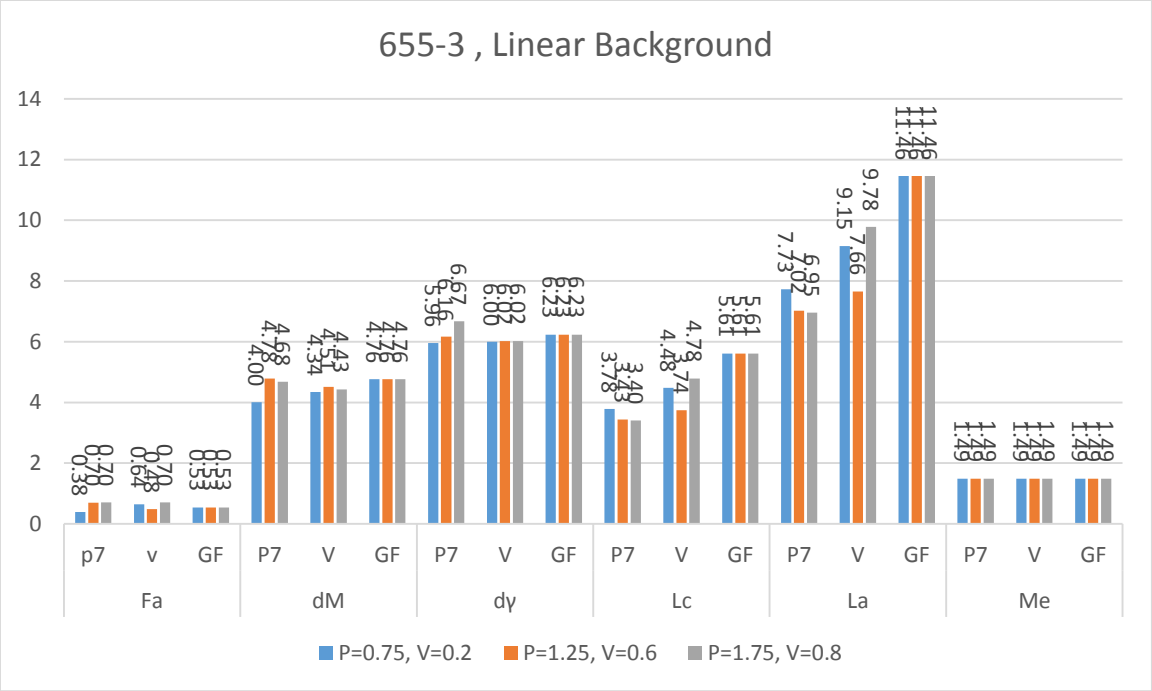

Figure 0-19: Aromaticity and Crystallite Parameters for Sample 655-3 Calculated Using Pearson VII, Pseudo-Voigt and GFF with Linear Background.

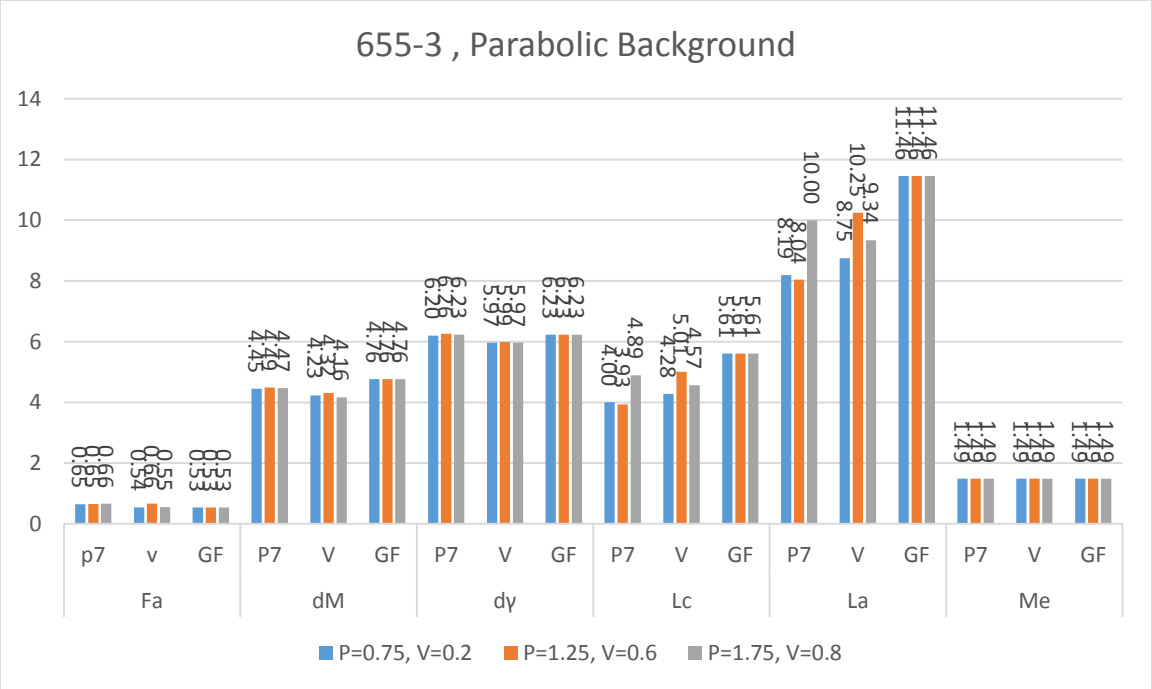

Figure 0-20: Aromaticity and Crystallite Parameters for Sample 655-3 Calculated Using Pearson VII, Pseudo-Voigt and GFF with Parabolic Background.

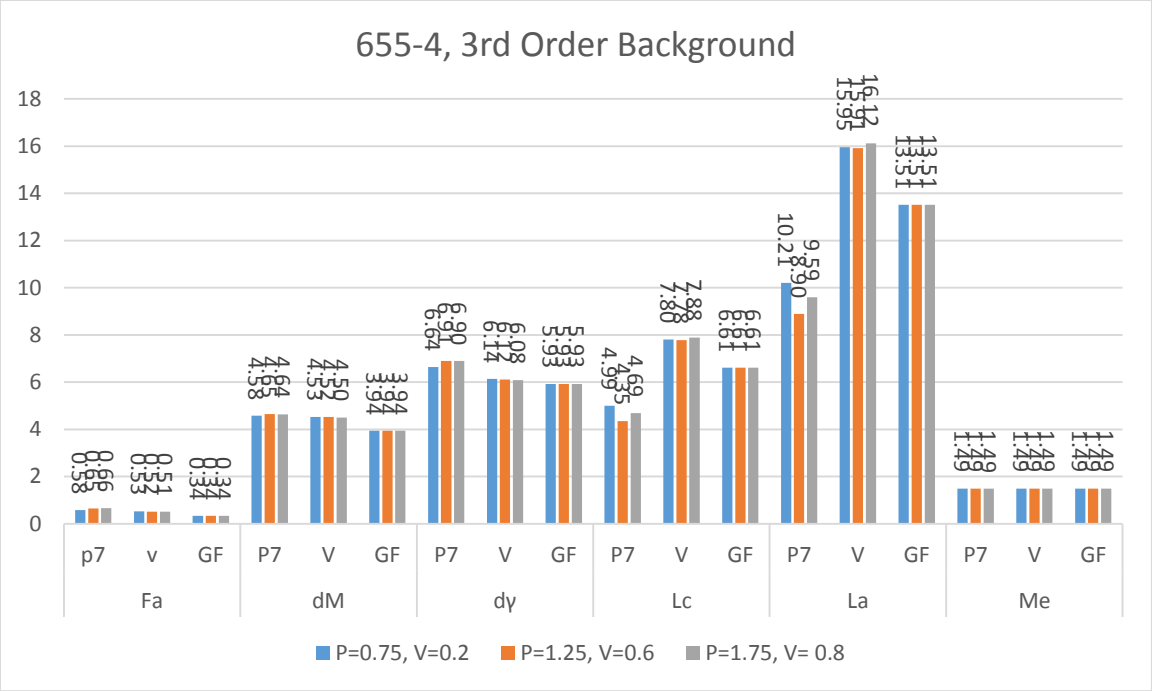

Figure 0-21: Aromaticity and Crystallite Parameters for Sample 655-4 Calculated Using Pearson VII, Pseudo-Voigt and GFF with 3d-Order Background.

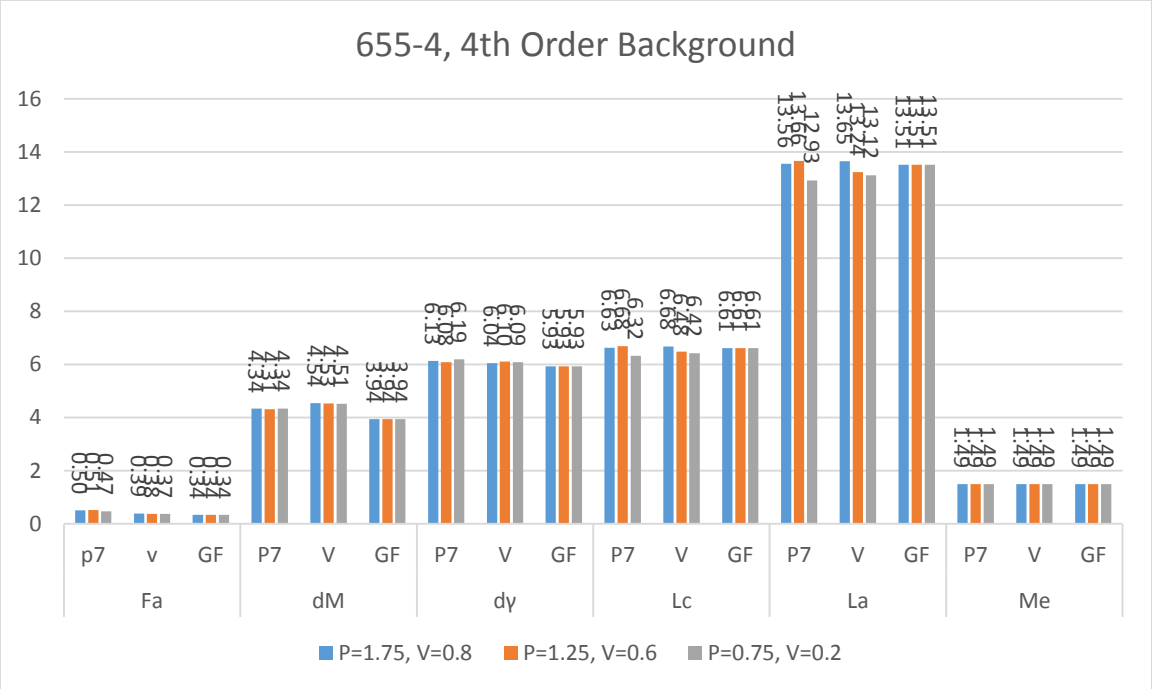

Figure 0-22: Aromaticity and Crystallite Parameters for Sample 655-4 Calculated Using Pearson VII, Pseudo-Voigt and GFF with 4th-Order Background.

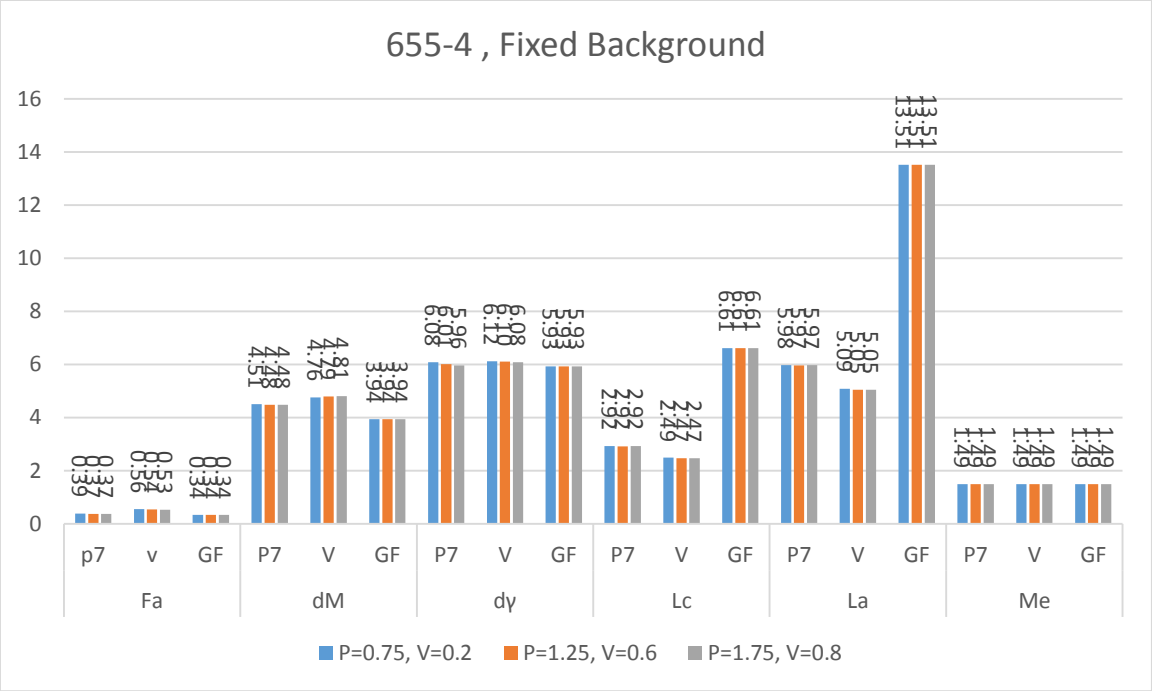

Figure 0-23: Aromaticity and Crystallite Parameters for Sample 655-4 Calculated Using Pearson VII, Pseudo-Voigt and GFF with Fixed Background.

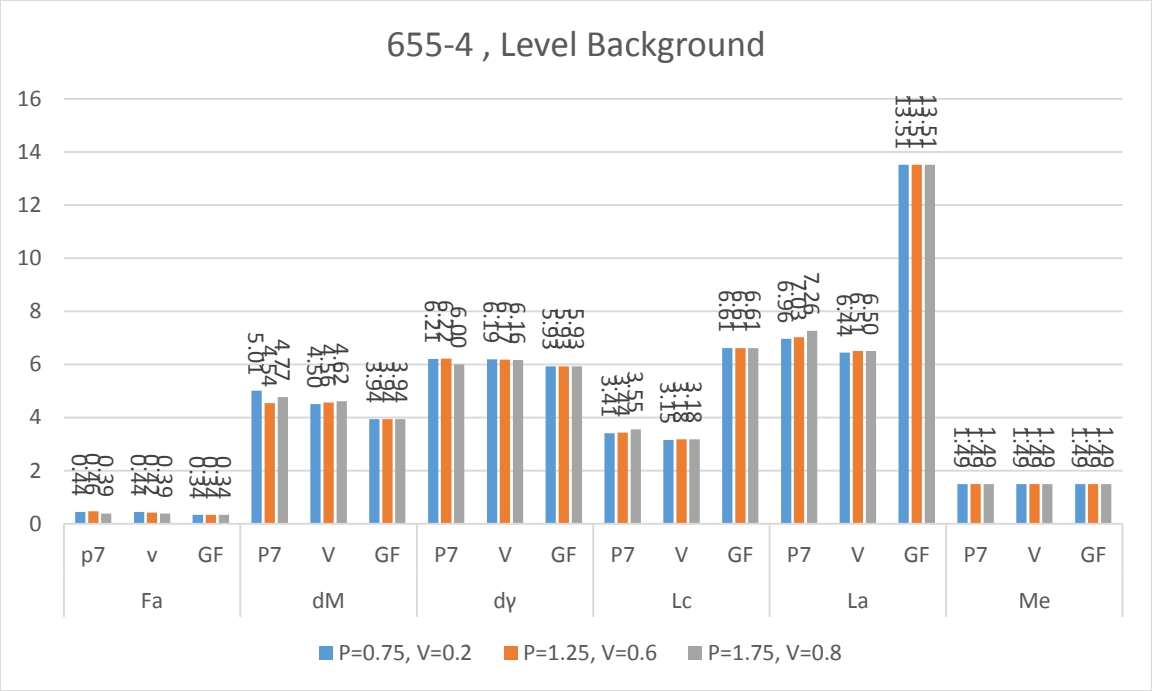

Figure 0-24: Aromaticity and Crystallite Parameters for Sample 655-4 Calculated Using Pearson VII, Pseudo-Voigt and GFF with Level Background.

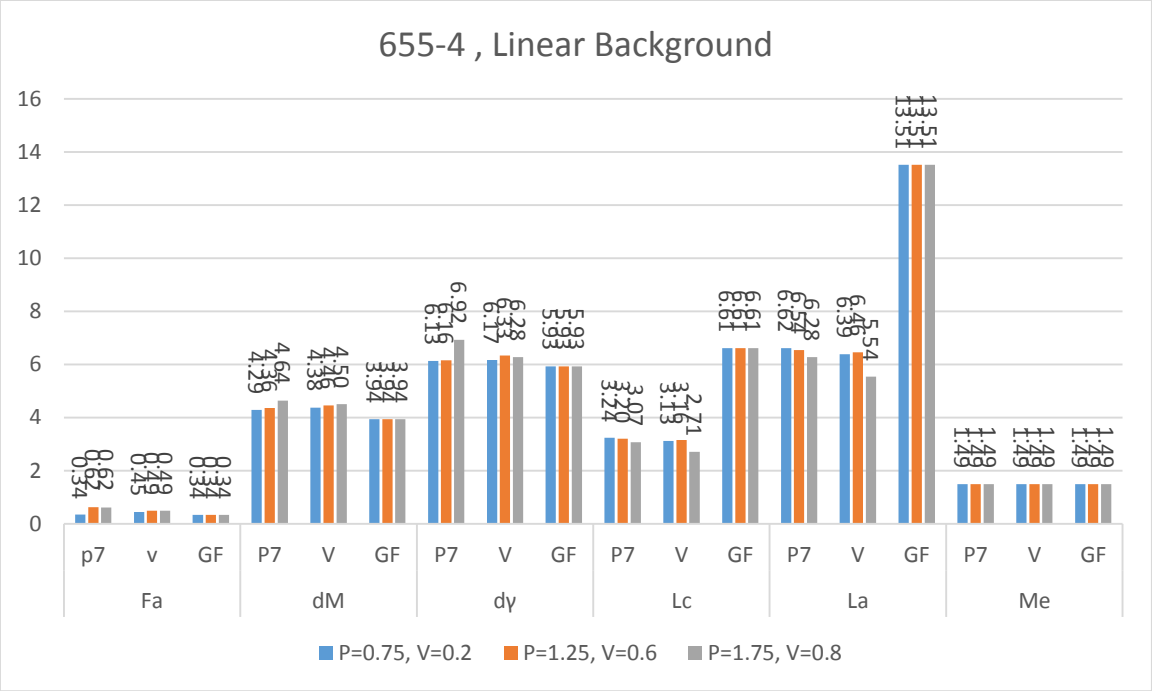

Figure 0-25: Aromaticity and Crystallite Parameters for Sample 655-4 Calculated Using Pearson VII, Pseudo-Voigt and GFF with Linear Background.

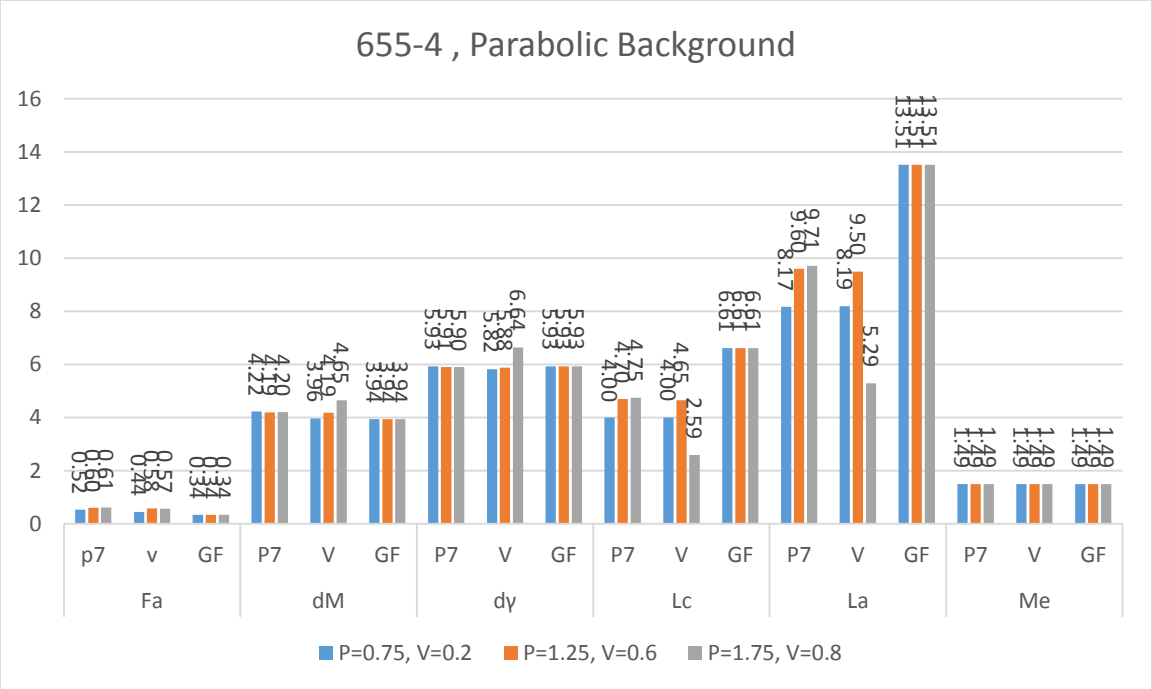

Figure 0-26: Aromaticity and Crystallite Parameters for Sample 655-4 Calculated Using Pearson VII, Pseudo-Voigt and GFF with Parabolic Background.

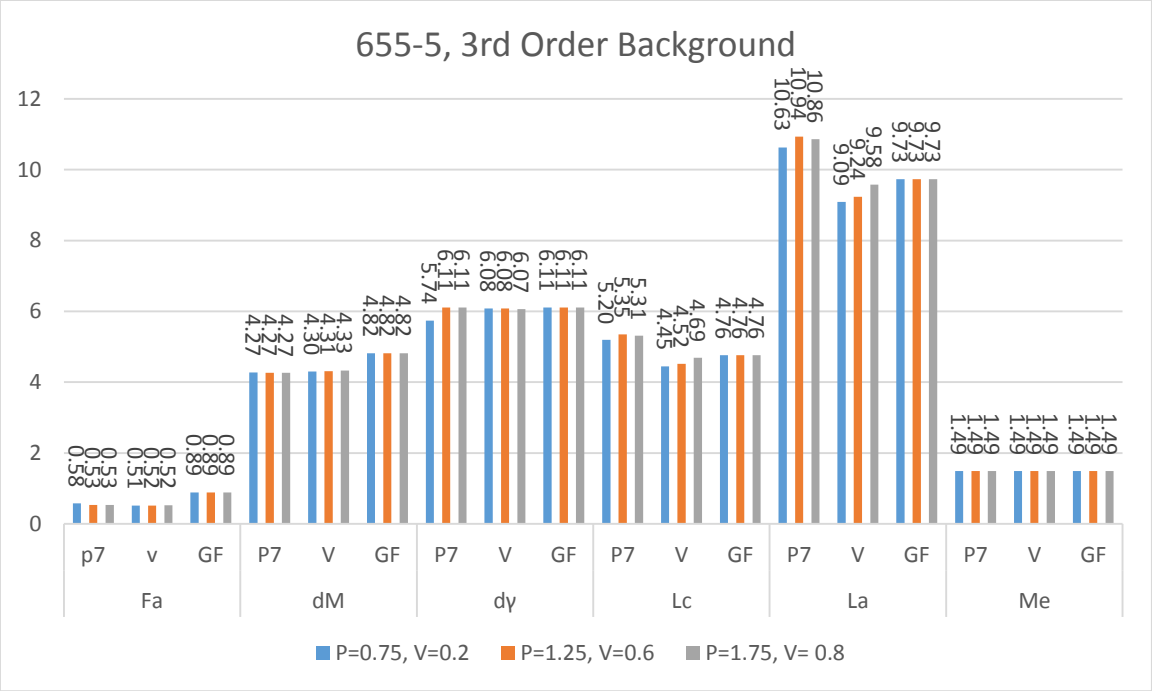

Figure 0-27: Aromaticity and Crystallite Parameters for Sample 655-5 Calculated Using Pearson VII, Pseudo-Voigt and GFF with 3d-Order Background.

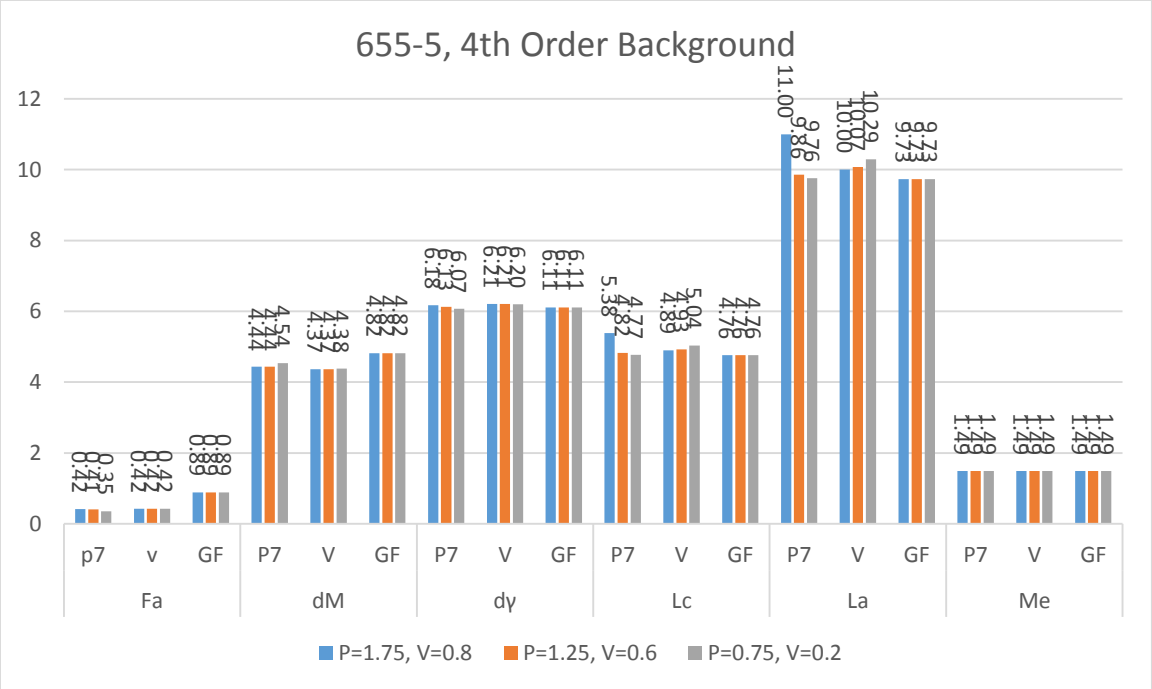

Figure 0-28: Aromaticity and Crystallite Parameters for Sample 655-5 Calculated Using Pearson VII, Pseudo-Voigt and GFF with 4th-Order Background.

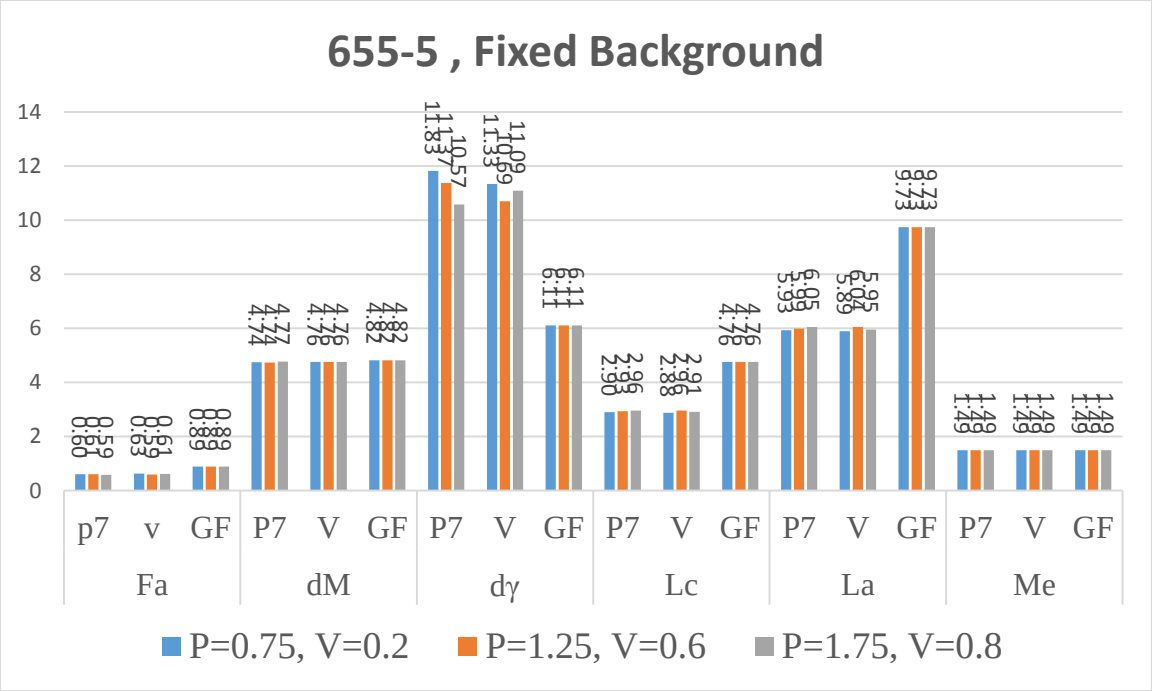

Figure 0-29: Aromaticity and Crystallite Parameters for Sample 655-5 Calculated Using Pearson VII, Pseudo-Voigt and GFF with Fixed Background.

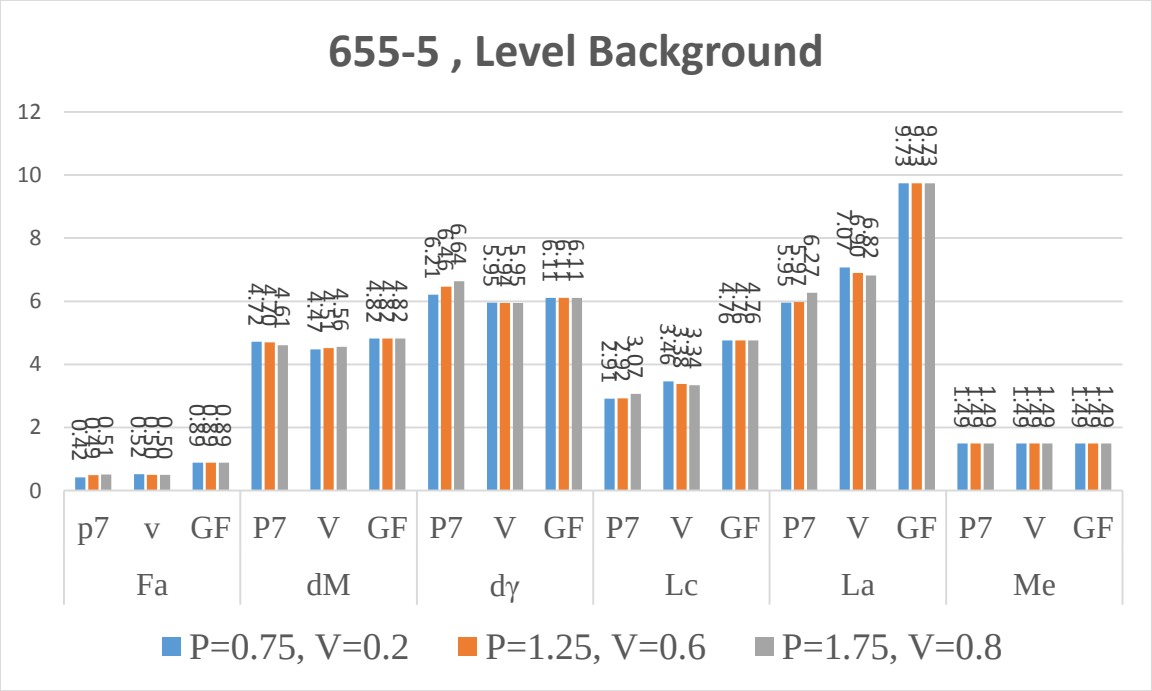

Figure 0-30: Aromaticity and Crystallite Parameters for Sample 655-5 Calculated Using Pearson VII, Pseudo-Voigt and GFF with Level Background.

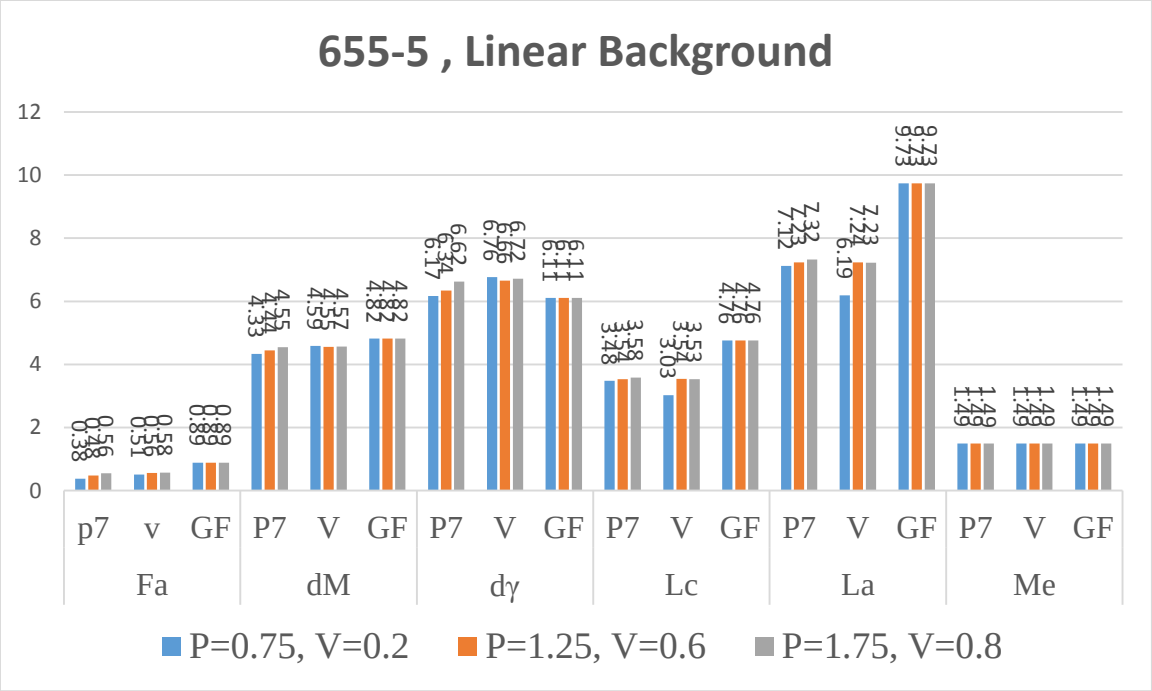

Figure 0-31: Aromaticity and Crystallite Parameters for Sample 655-5 Calculated Using Pearson VII, Pseudo-Voigt and GFF with Linear Background.

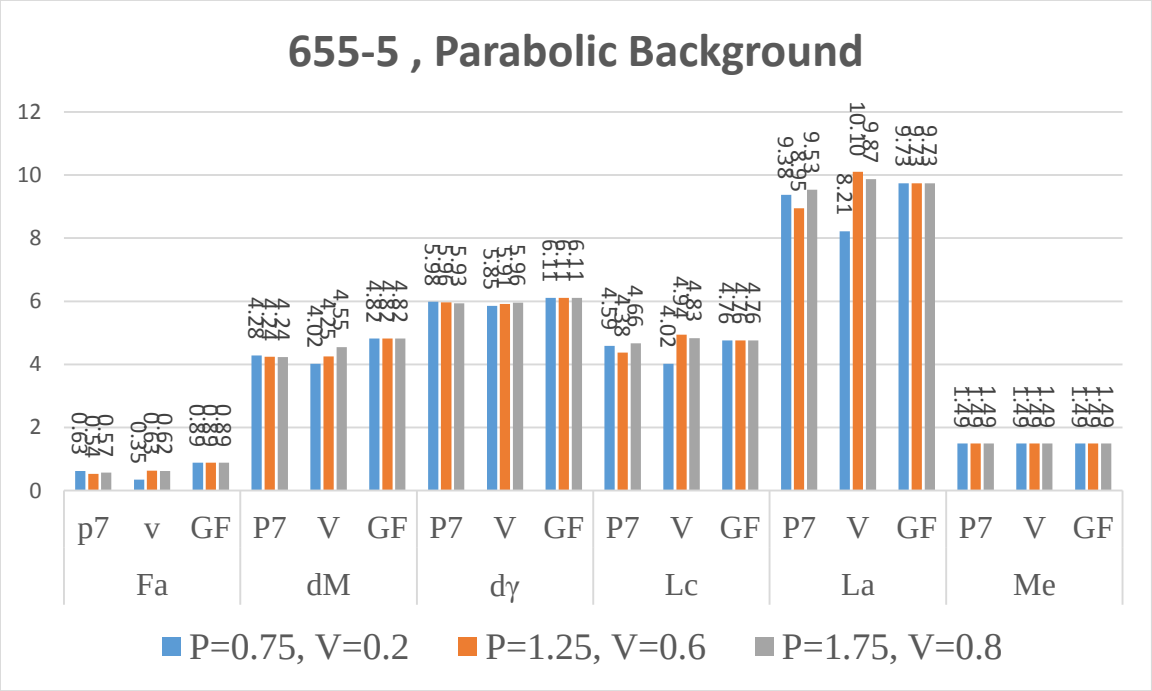

Figure 0-32: Aromaticity and Crystallite Parameters for Sample 655-5 Calculated Using Pearson VII, Pseudo-Voigt and GFF with Parabolic Background.

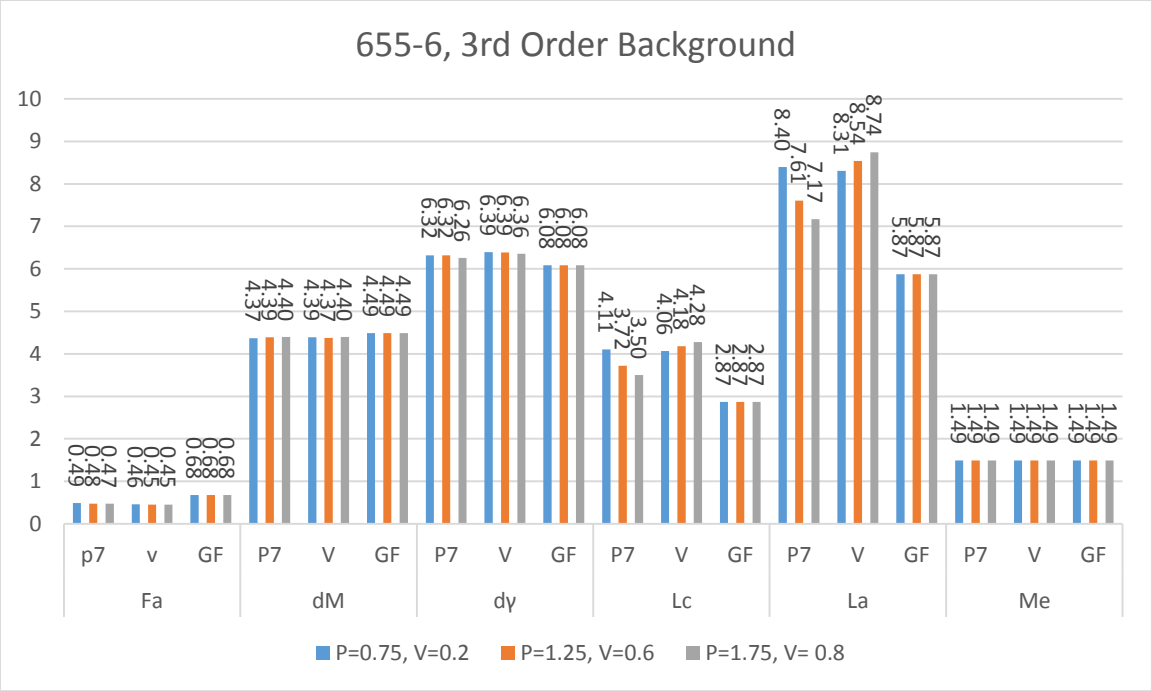

Figure 0-33: Aromaticity and Crystallite Parameters for Sample 655-6 Calculated Using Pearson VII, Pseudo-Voigt and GFF with 3d-Order Background.

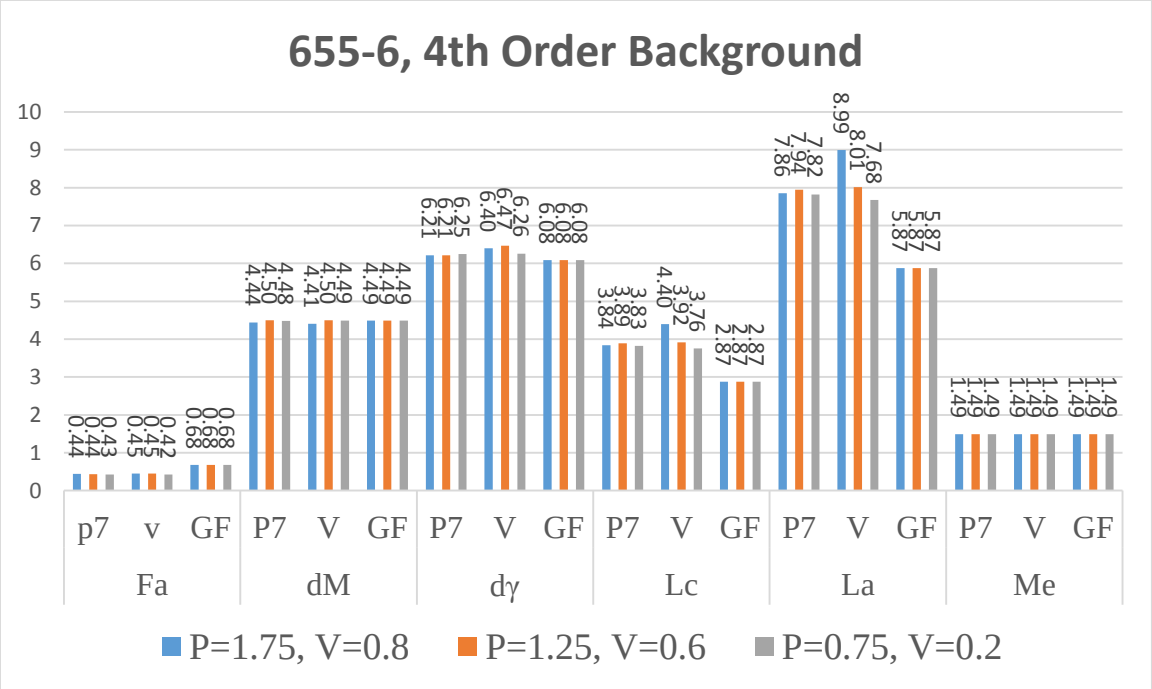

Figure 0-34: Aromaticity and Crystallite Parameters for Sample 655-6 Calculated Using Pearson VII, Pseudo-Voigt and GFF with 4th-Order Background.

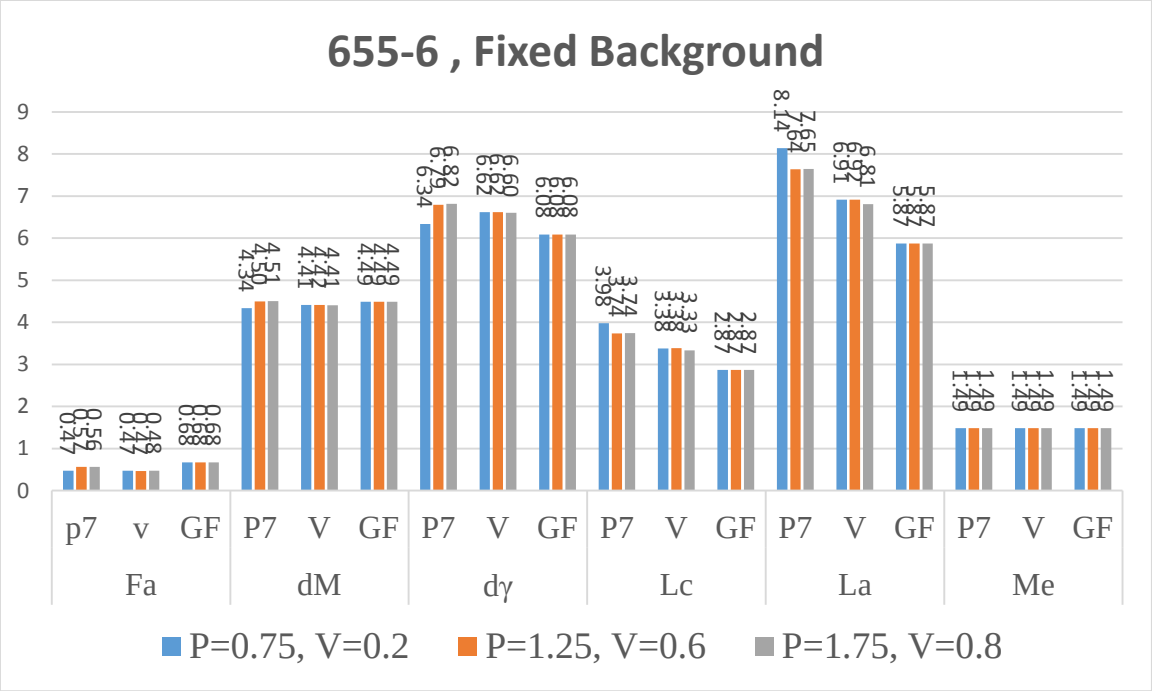

Figure 0-35: Aromaticity and Crystallite Parameters for Sample 655-6 Calculated Using Pearson VII, Pseudo-Voigt and GFF with Fixed Background.

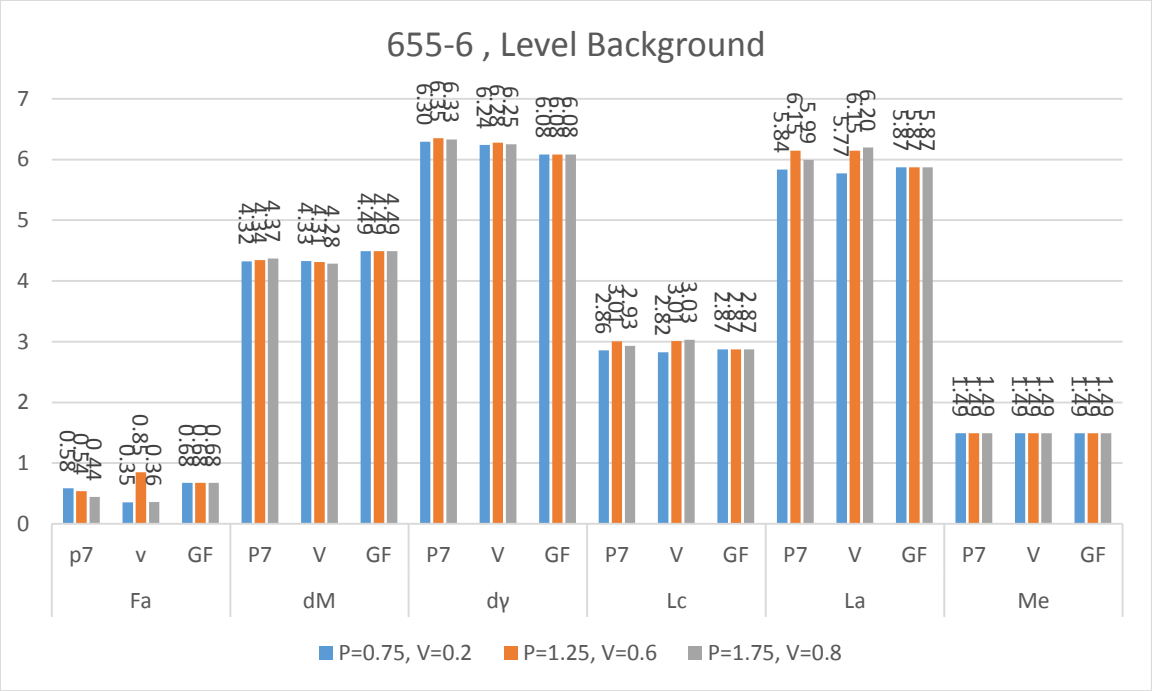

Figure 0-36: Aromaticity and Crystallite Parameters for Sample 655-6 Calculated Using Pearson VII, Pseudo-Voigt and GFF with Level Background.

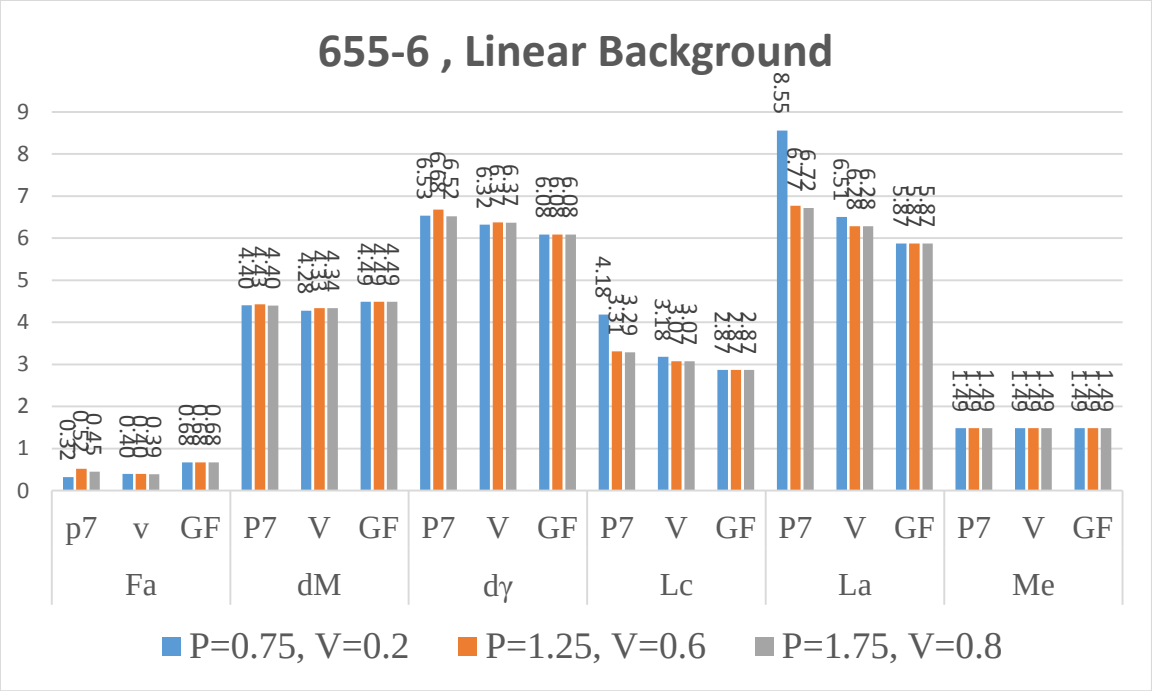

Figure 0-37: Aromaticity and Crystallite Parameters for Sample 655-6 Calculated Using Pearson VII, Pseudo-Voigt and GFF with Linear Background.

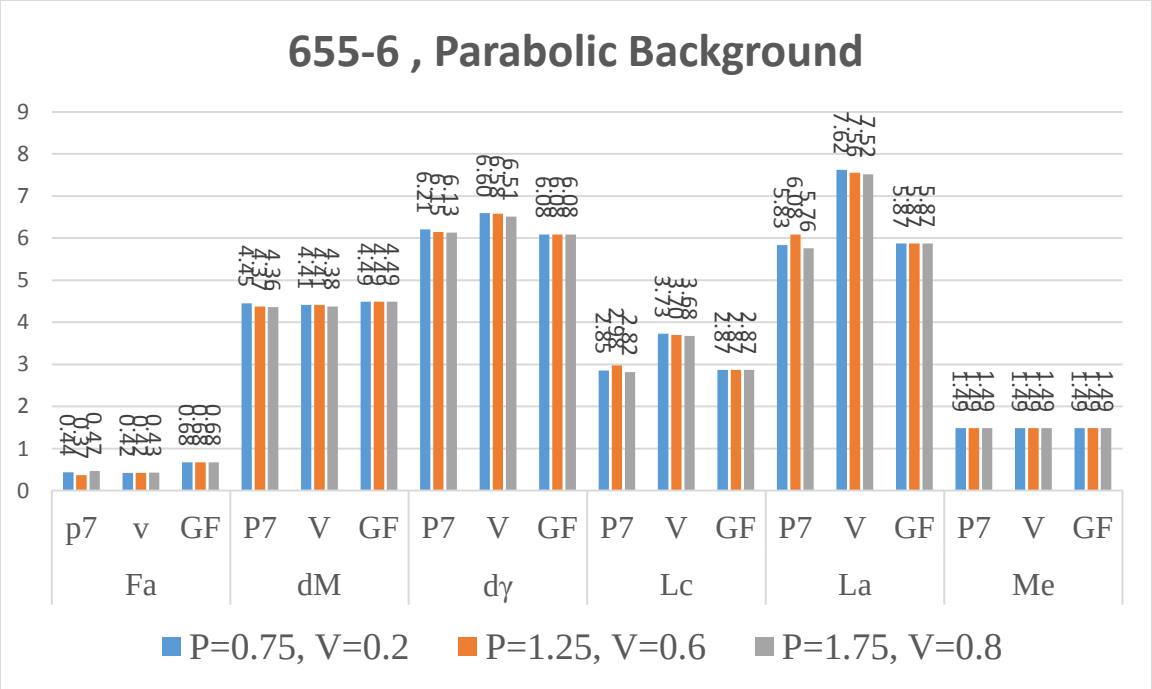

Figure 0-38: Aromaticity and Crystallite Parameters for Sample 655-6 Calculated Using Pearson VII, Pseudo-Voigt and GFF with Parabolic Background.

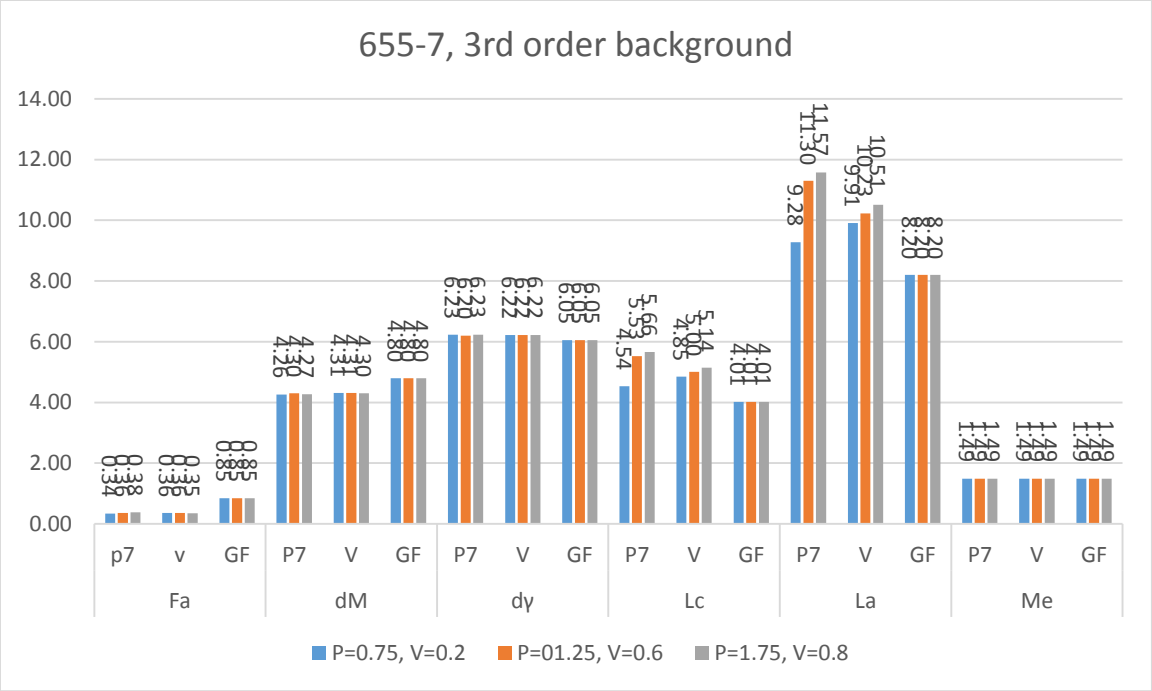

Figure 0-39: Aromaticity and Crystallite Parameters for Sample 655-7 Calculated Using Pearson VII, Pseudo-Voigt and GFF with 3d-Order Background.

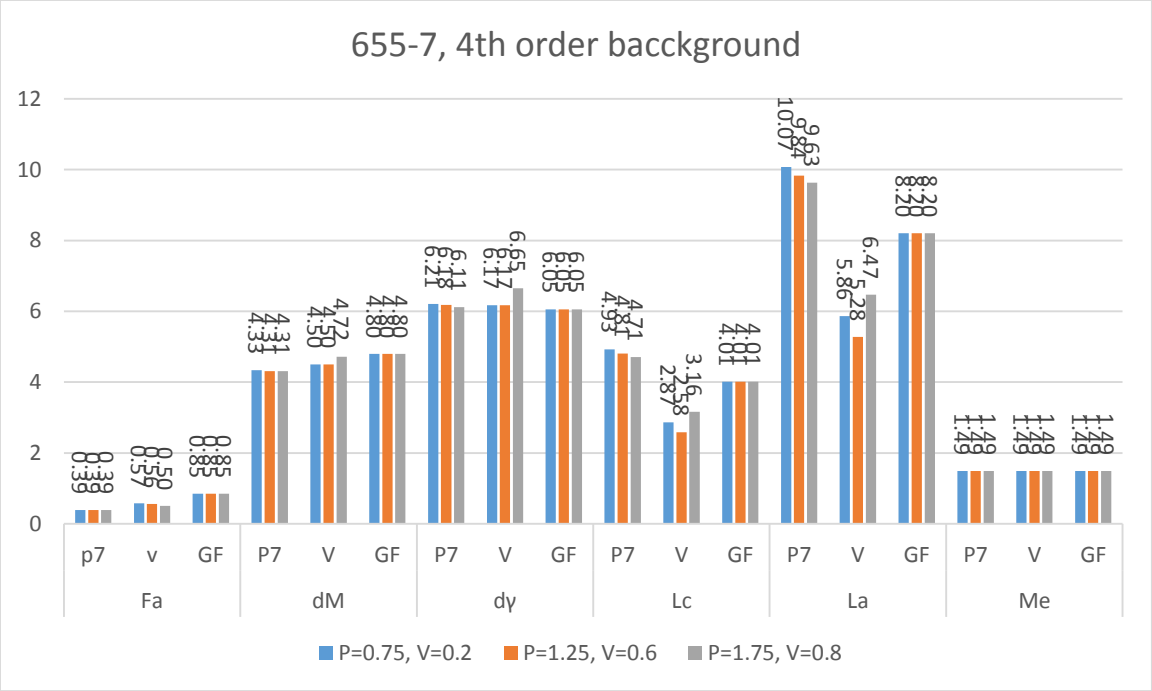

Figure 0-40: Aromaticity and Crystallite Parameters for Sample 655-7 Calculated Using Pearson VII, Pseudo-Voigt and GFF with 4th-Order Background.

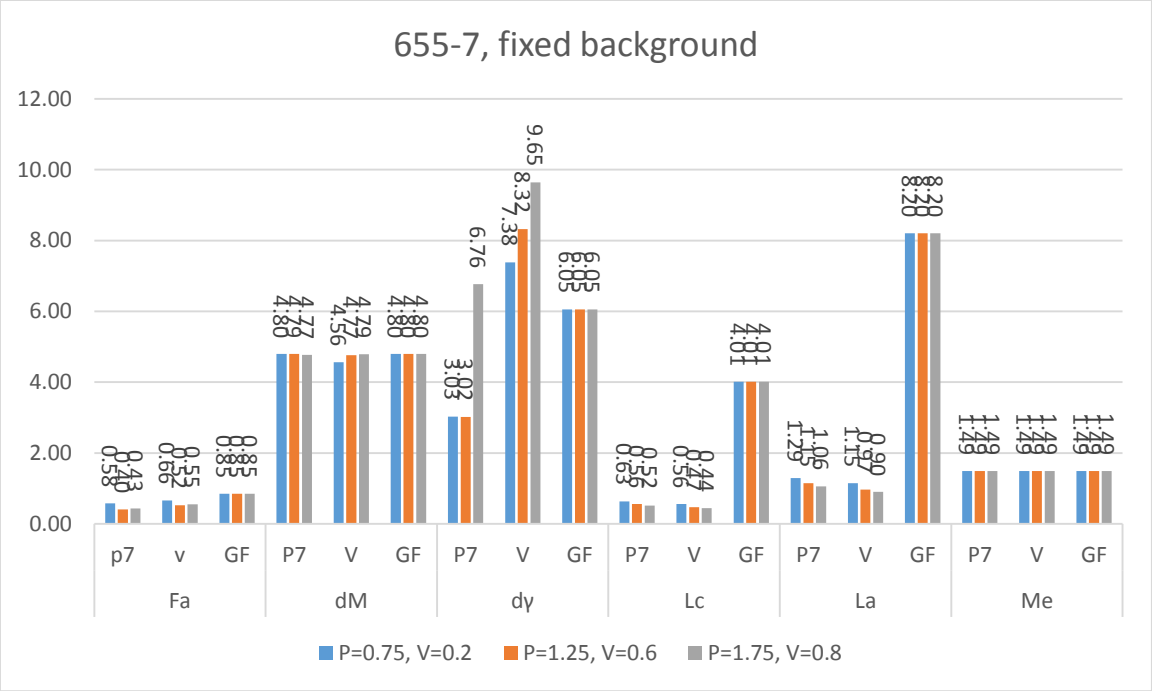

Figure 0-41: Aromaticity and Crystallite Parameters for Sample 655-7 Calculated Using Pearson VII, Pseudo-Voigt and GFF with Fixed Background.

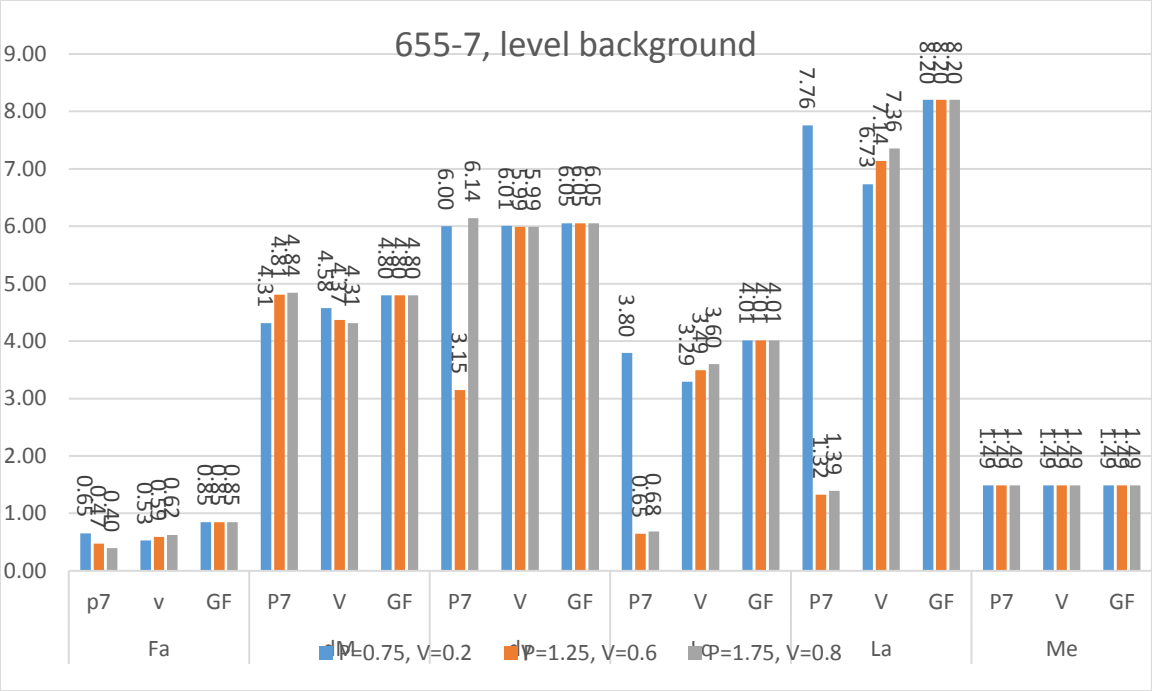

Figure 0-42: Aromaticity and Crystallite Parameters for Sample 655-7 Calculated Using Pearson VII, Pseudo-Voigt and GFF with Level Background.

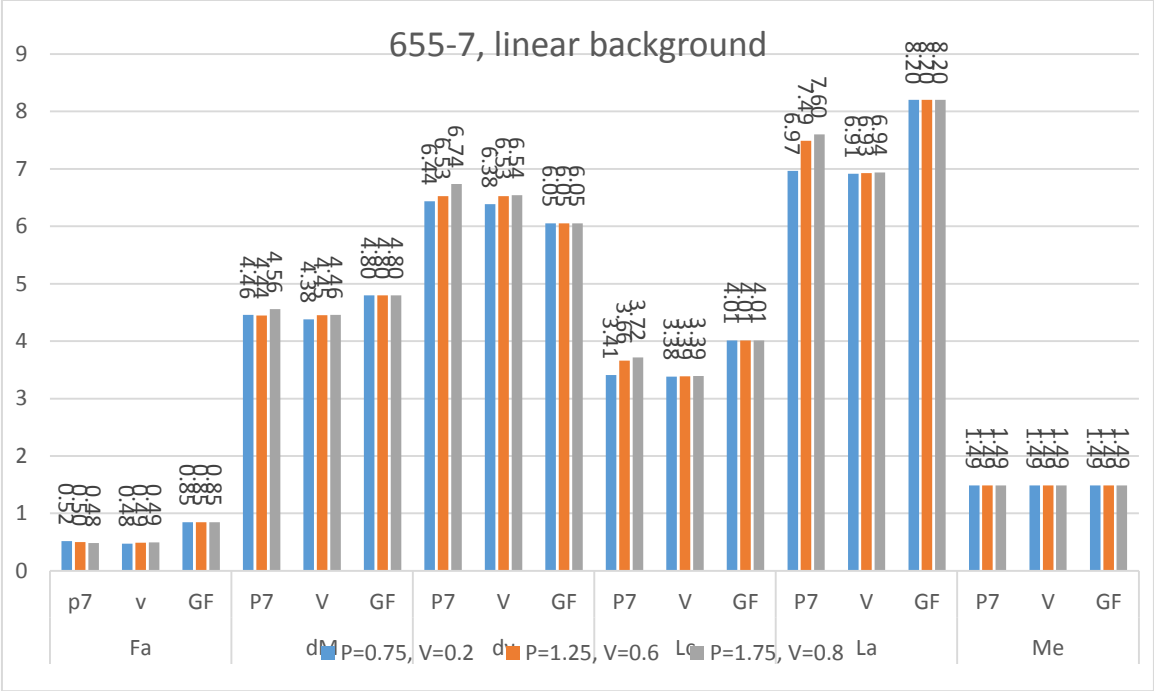

Figure 0-43: Aromaticity and Crystallite Parameters for Sample 655-7 Calculated Using Pearson VII, Pseudo-Voigt and GFF with Linear Background.

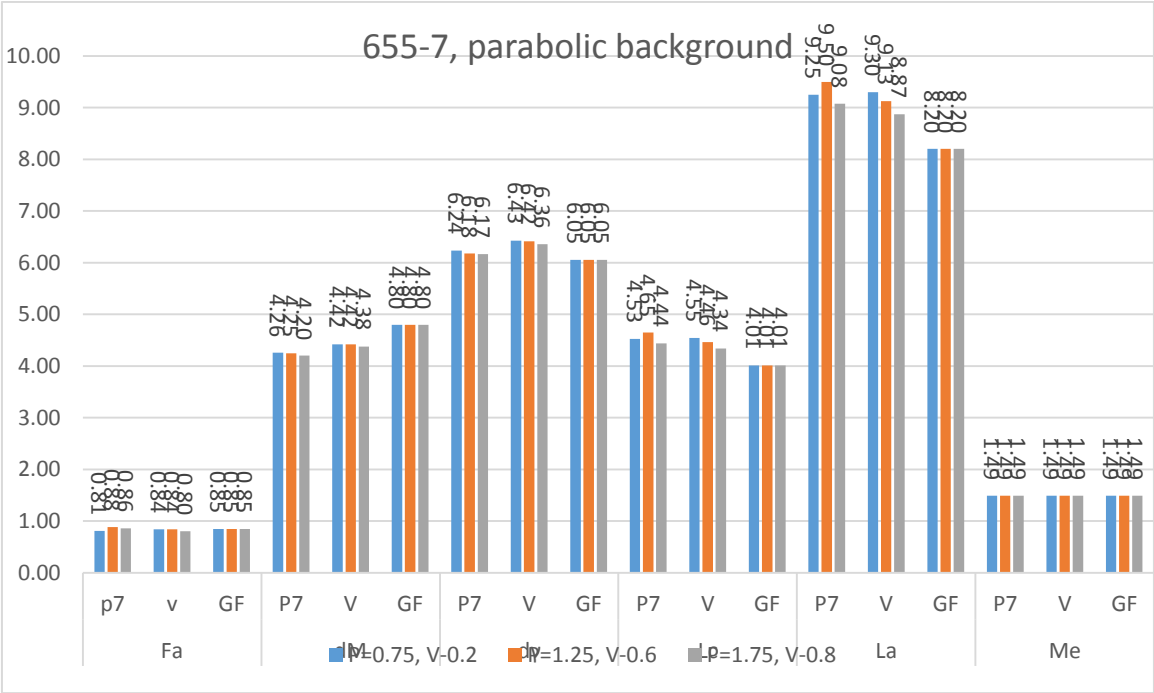

Figure 0-44: Aromaticity and Crystallite Parameters for Sample 655-7 Calculated Using Pearson VII, Pseudo-Voigt and GFF with Parabolic Background.

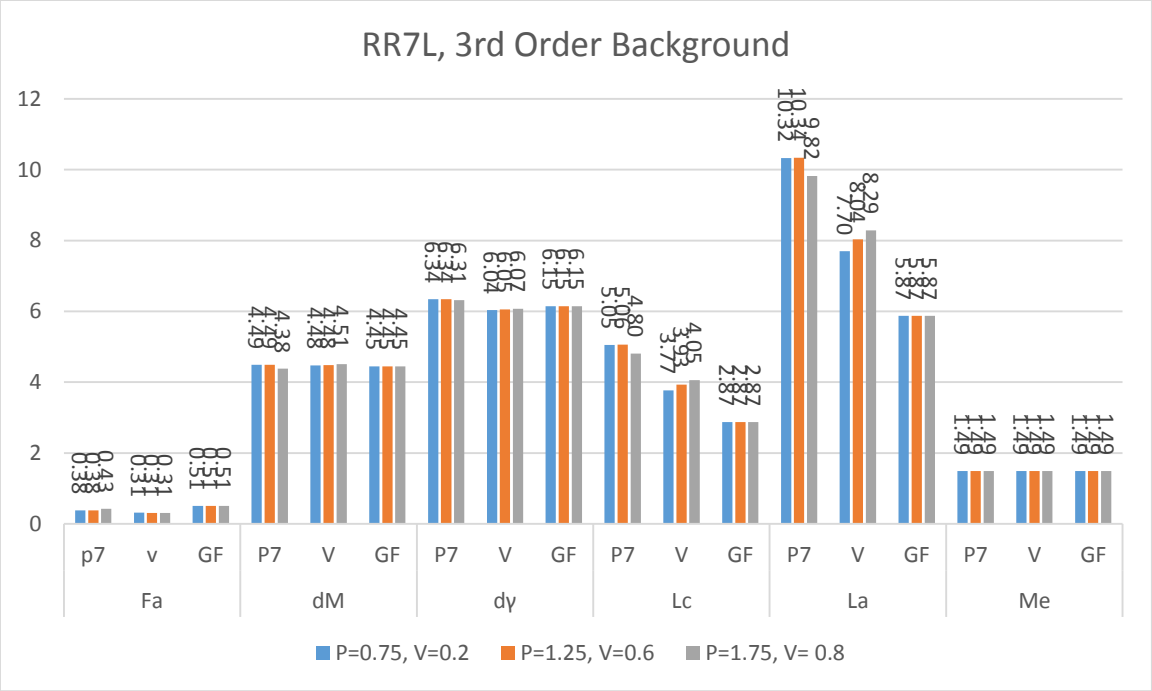

Figure 0-45: Aromaticity and Crystallite Parameters for Sample RR7L Calculated Using Pearson VII, Pseudo-Voigt and GFF with 3d-Order Background.

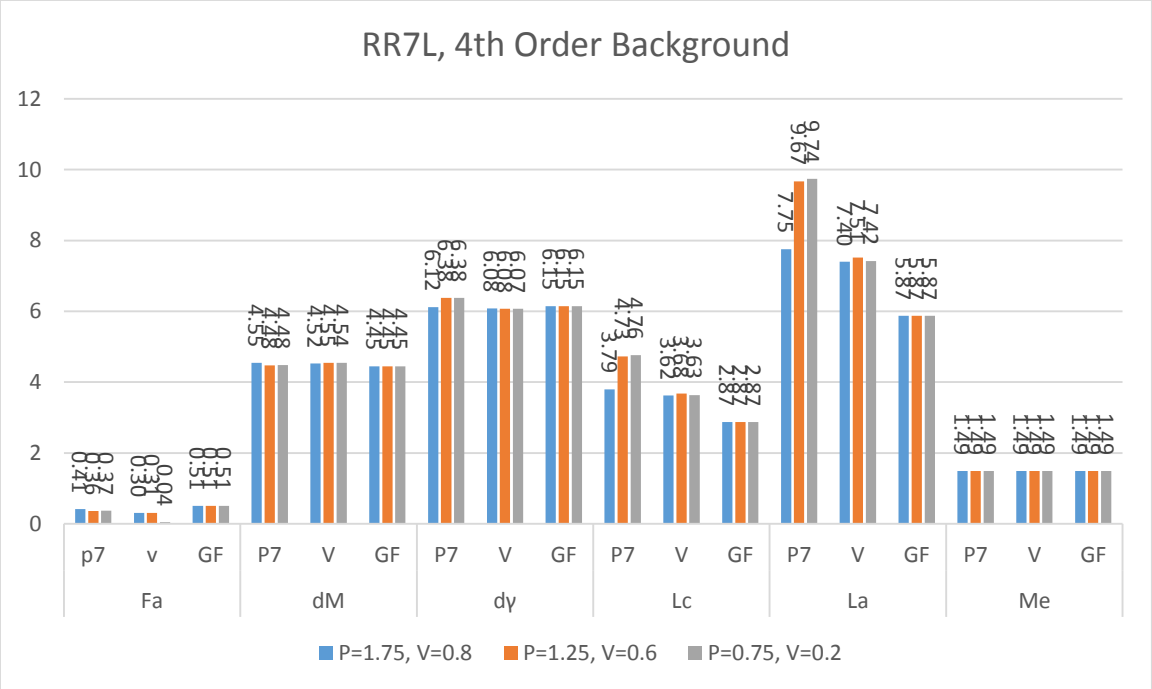

Figure 0-46: Aromaticity and Crystallite Parameters for Sample RR7L Calculated Using Pearson VII, Pseudo-Voigt and GFF with 4th-Order Background.

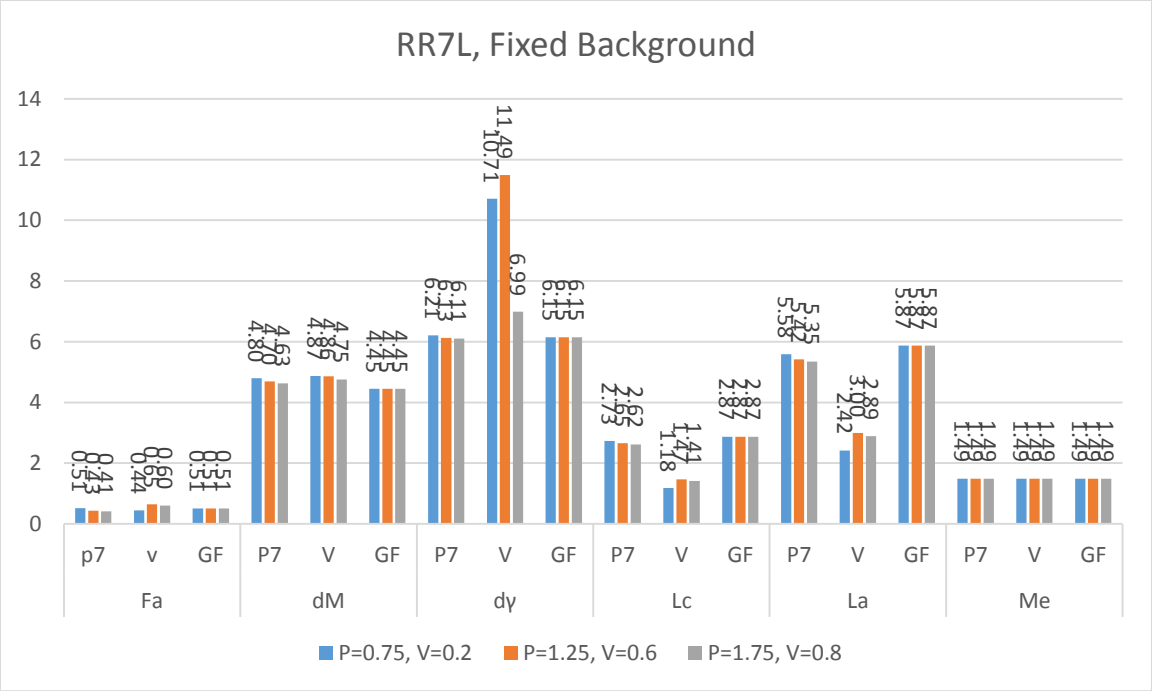

Figure 0-47: Aromaticity and Crystallite Parameters for Sample RR7L Calculated Using Pearson VII, Pseudo-Voigt and GFF with Fixed Background.

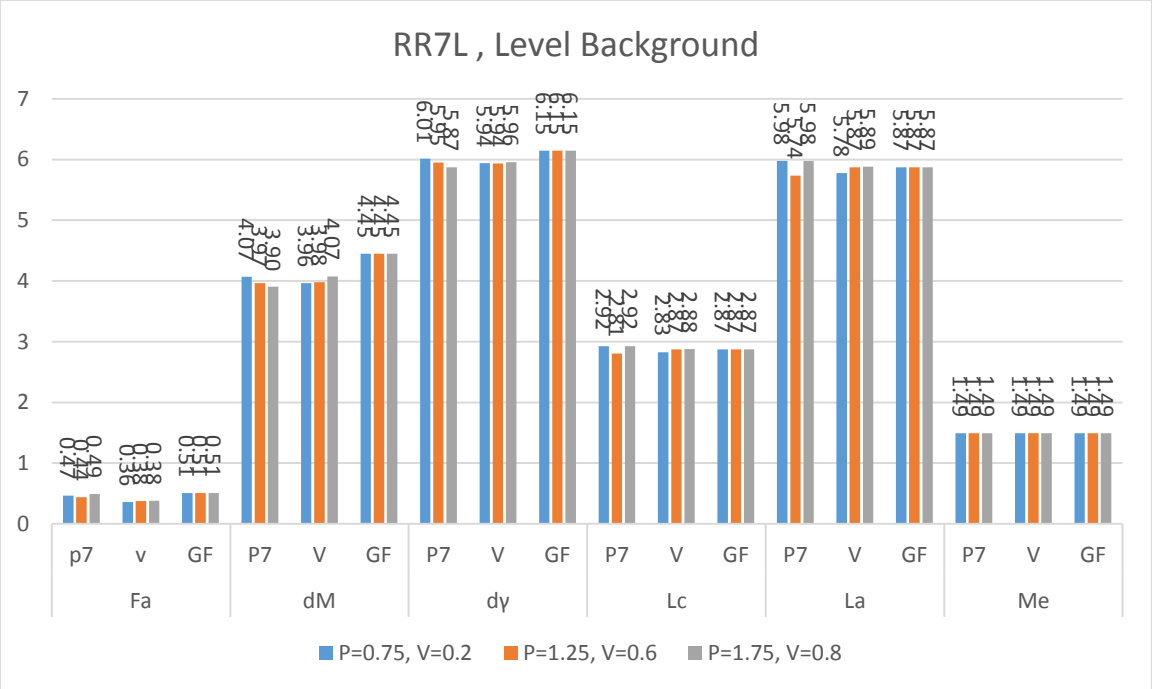

Figure 0-48: Aromaticity and Crystallite Parameters for Sample RR7L Calculated Using Pearson VII, Pseudo-Voigt and GFF with Level Background.

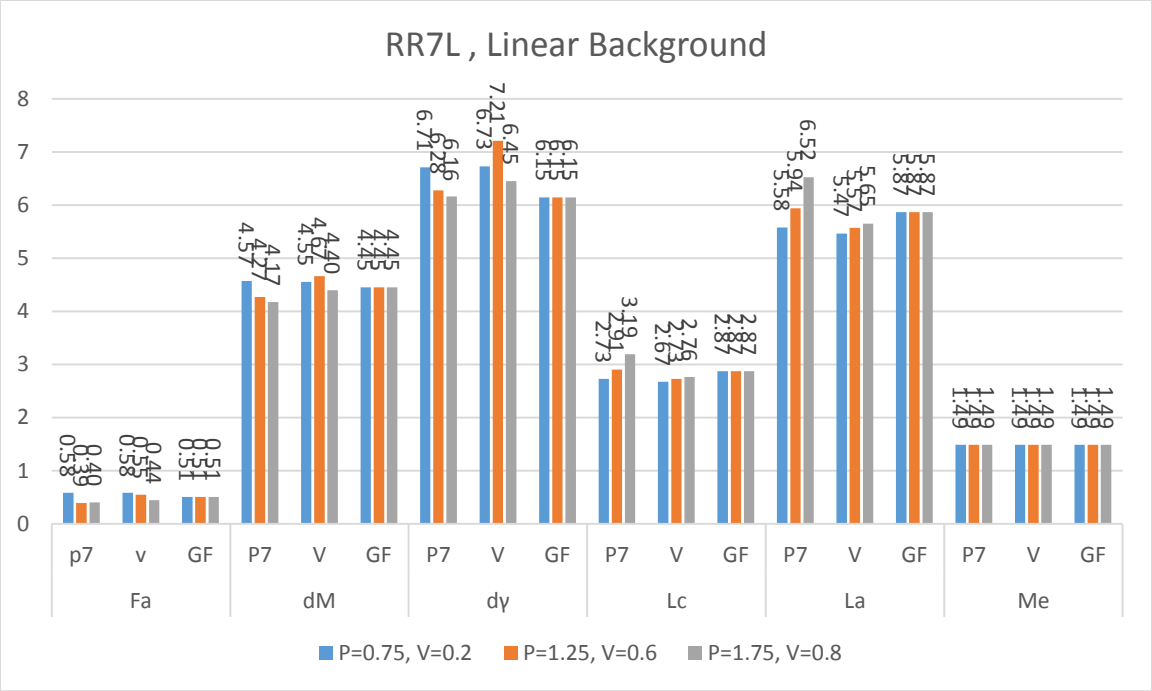

Figure 0-49: Aromaticity and Crystallite Parameters for Sample RR7L Calculated Using Pearson VII, Pseudo-Voigt and GFF with Linear Background.

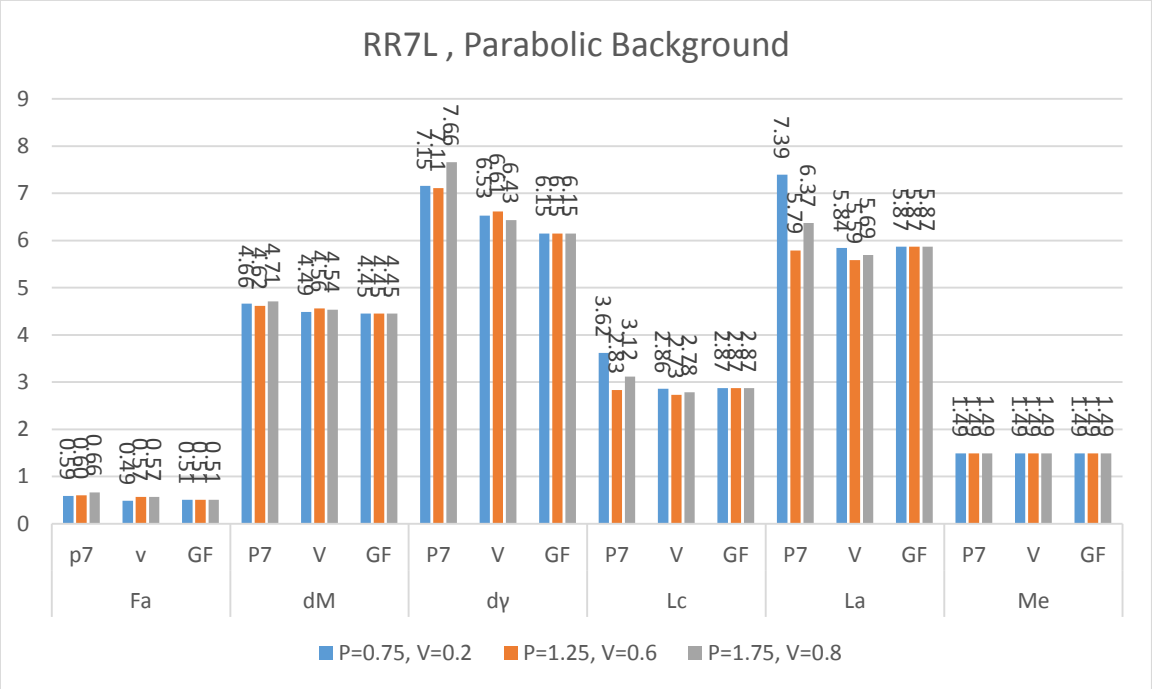

Figure 0-50: Aromaticity and Crystallite Parameters for Sample RR7L Calculated Using Pearson VII, Pseudo-Voigt and GFF with Parabolic Background.

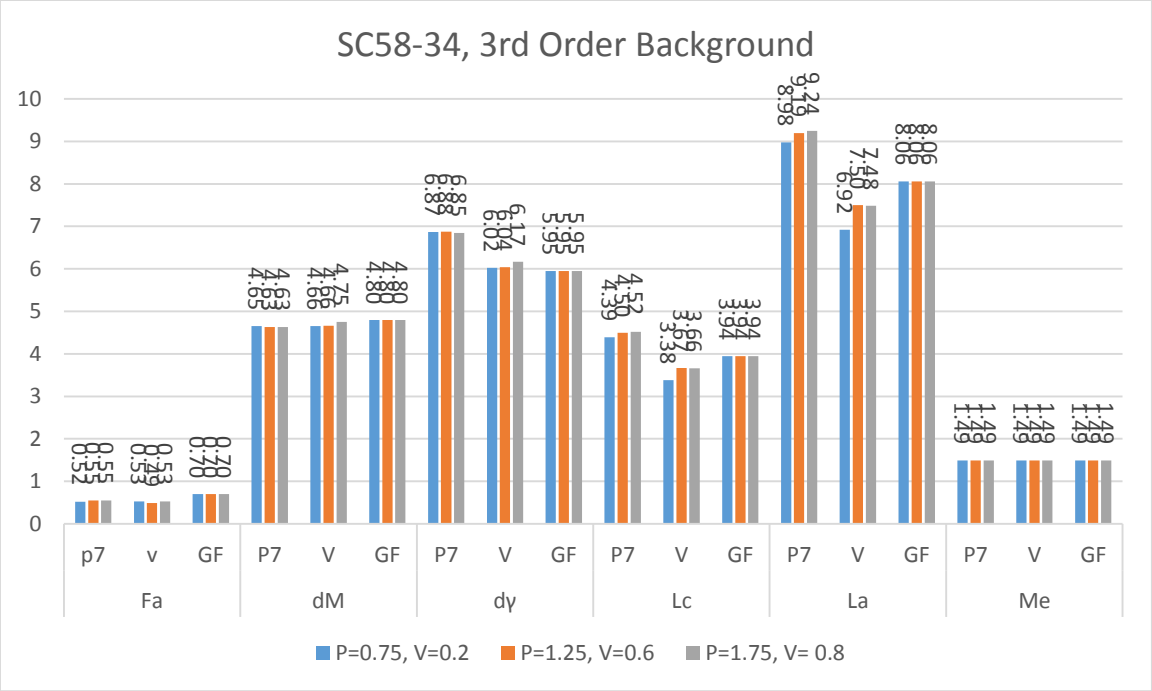

Figure 0-51: Aromaticity and Crystallite Parameters for Sample SC58-34 Calculated Using Pearson VII, Pseudo-Voigt and GFF with 3d-Order Background.

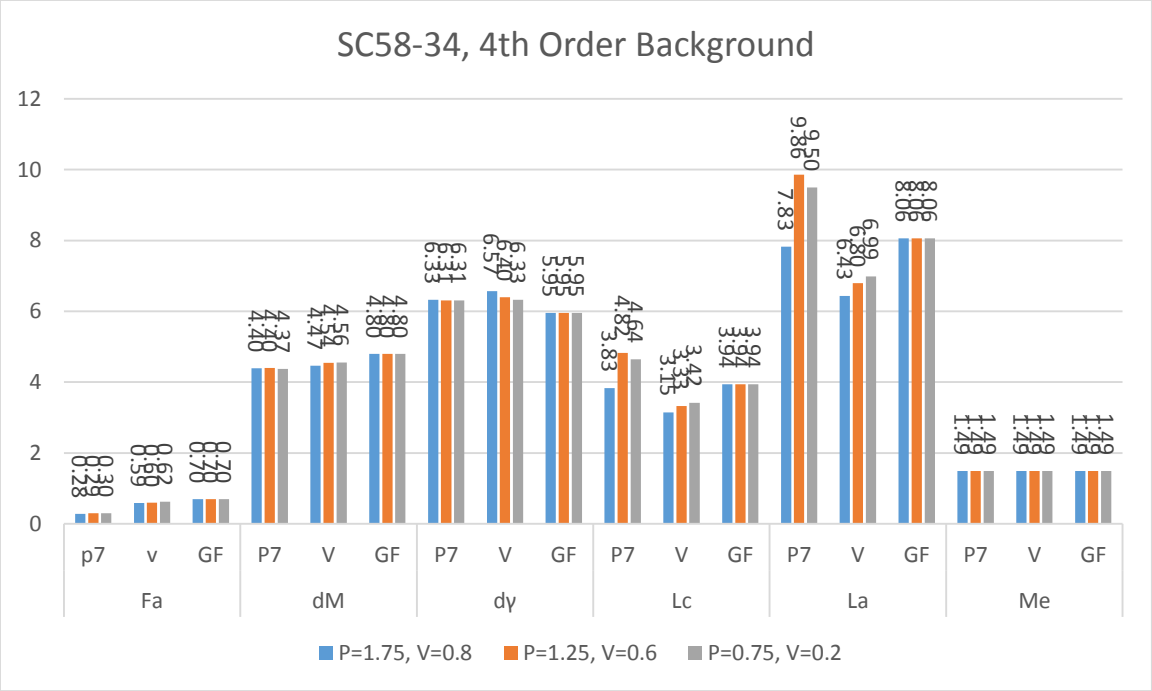

Figure 0-52: Aromaticity and Crystallite Parameters for Sample SC58-34 Calculated Using Pearson VII, Pseudo-Voigt and GFF with 4th-Order Background.

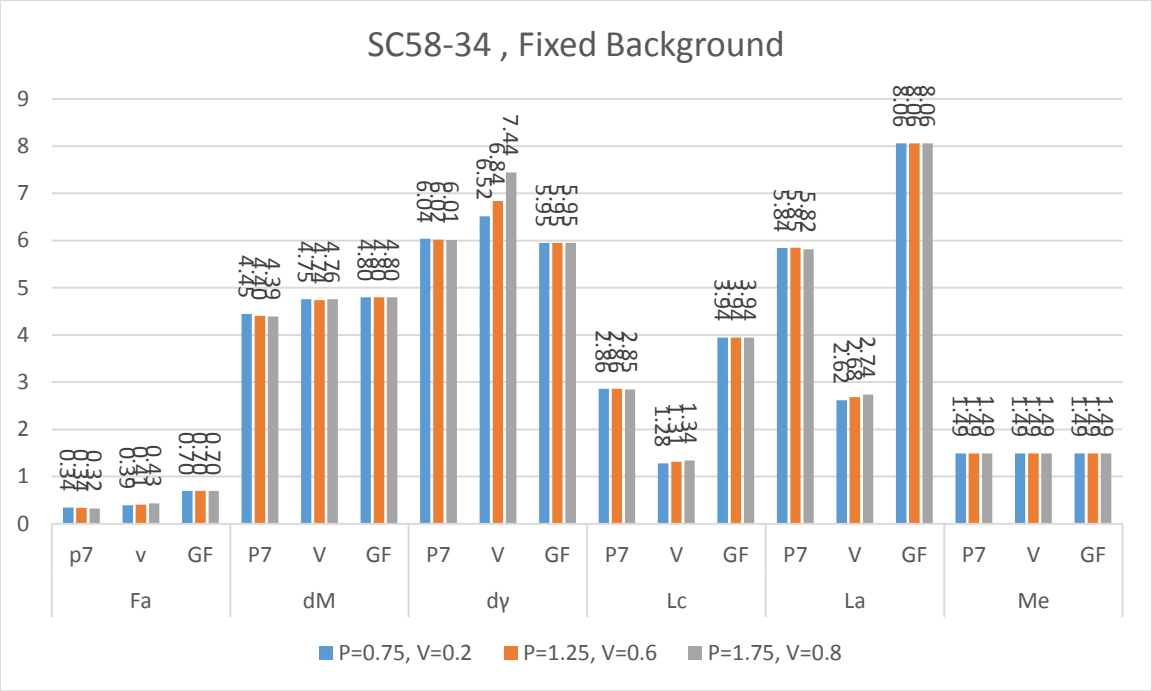

Figure 0-53: Aromaticity and Crystallite Parameters for Sample SC58-34 Calculated Using Pearson VII, Pseudo-Voigt and GFF with Fixed Background.

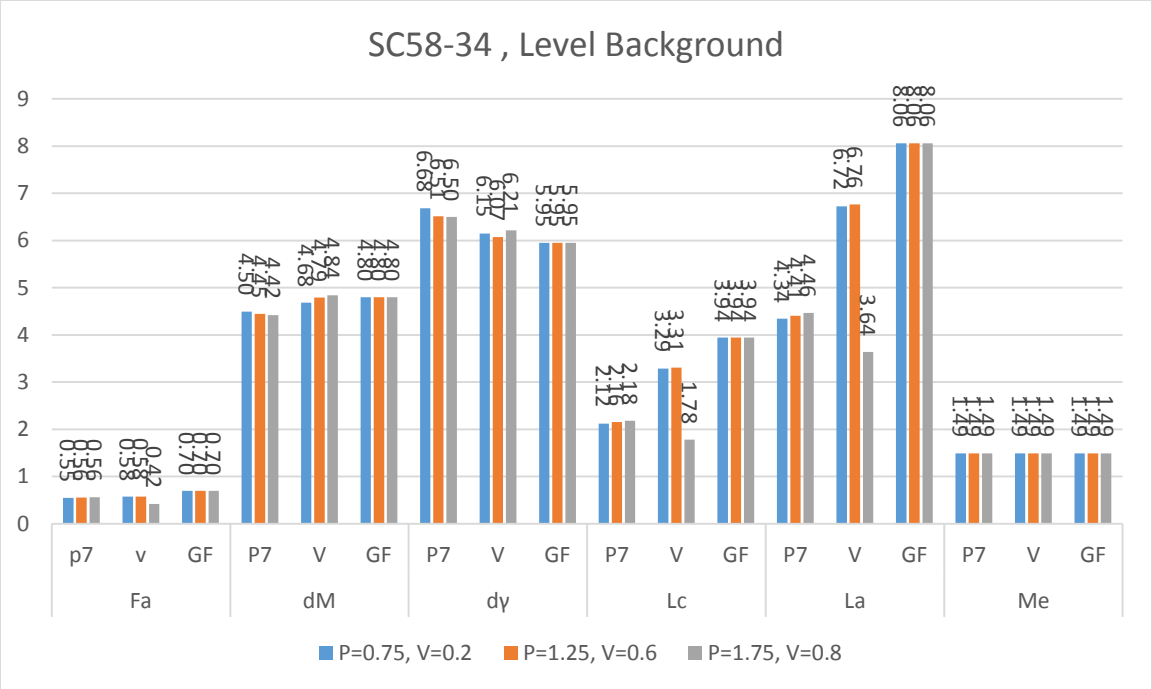

Figure 0-54: Aromaticity and Crystallite Parameters for Sample SC58-34 Calculated Using Pearson VII, Pseudo-Voigt and GFF with Level Background.

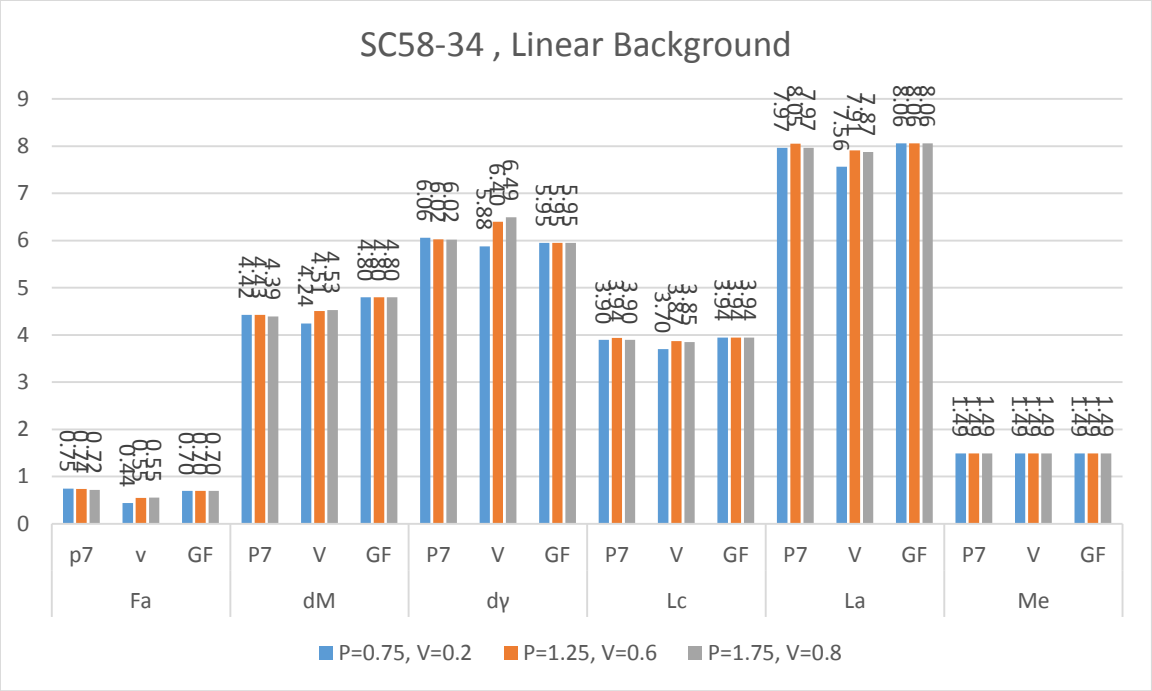

Figure 0-55: Aromaticity and Crystallite Parameters for Sample SC58-34 Calculated Using Pearson VII, Pseudo-Voigt and GFF with Linear Background.

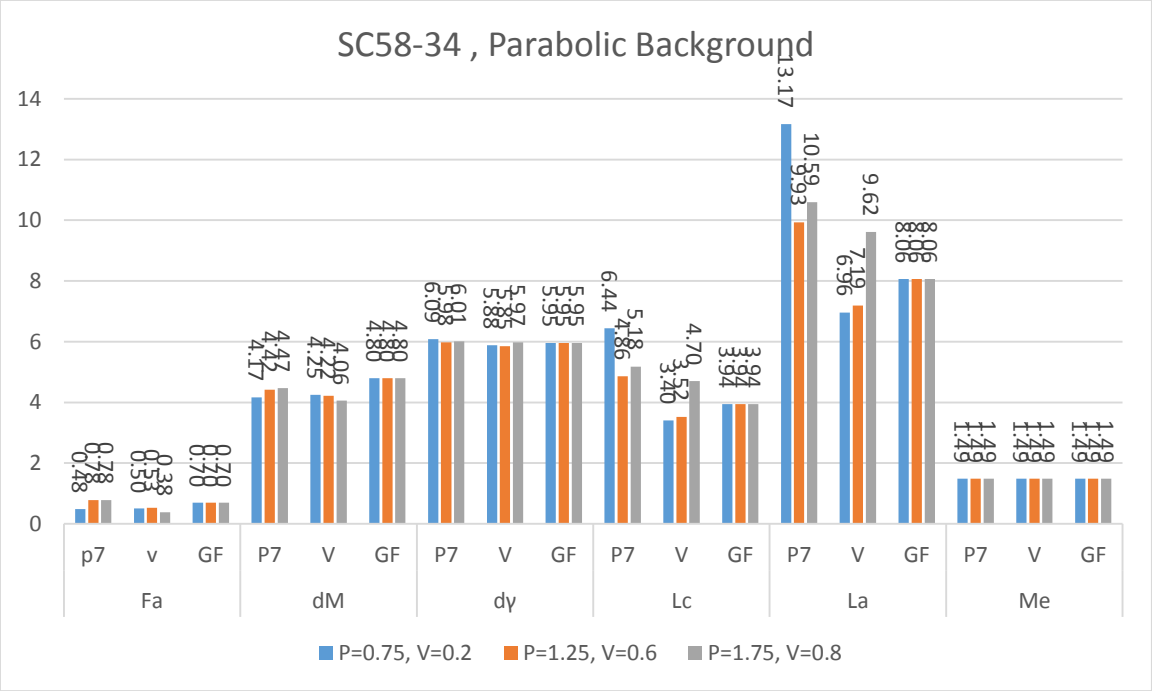

Figure 0-56: Aromaticity and Crystallite Parameters for Sample SC58-34 Calculated Using Pearson VII, Pseudo-Voigt and GFF with Parabolic Background.

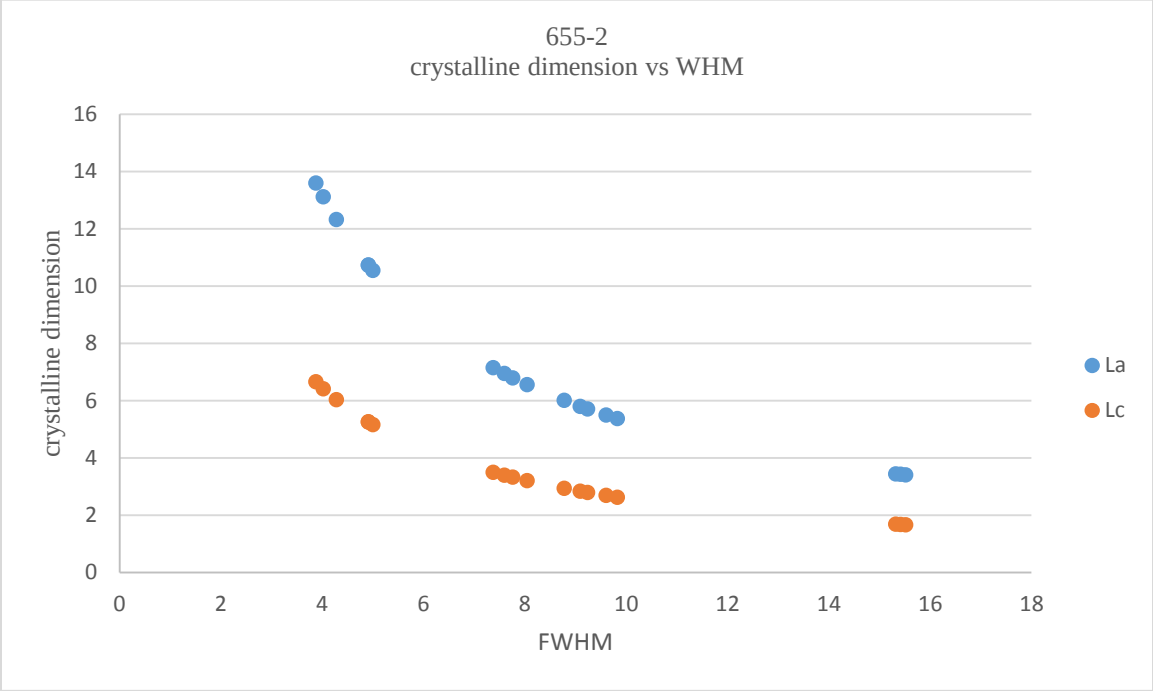

Figure 0-57: Crystalline Dimension Vs FWHM for Sample 655-2.

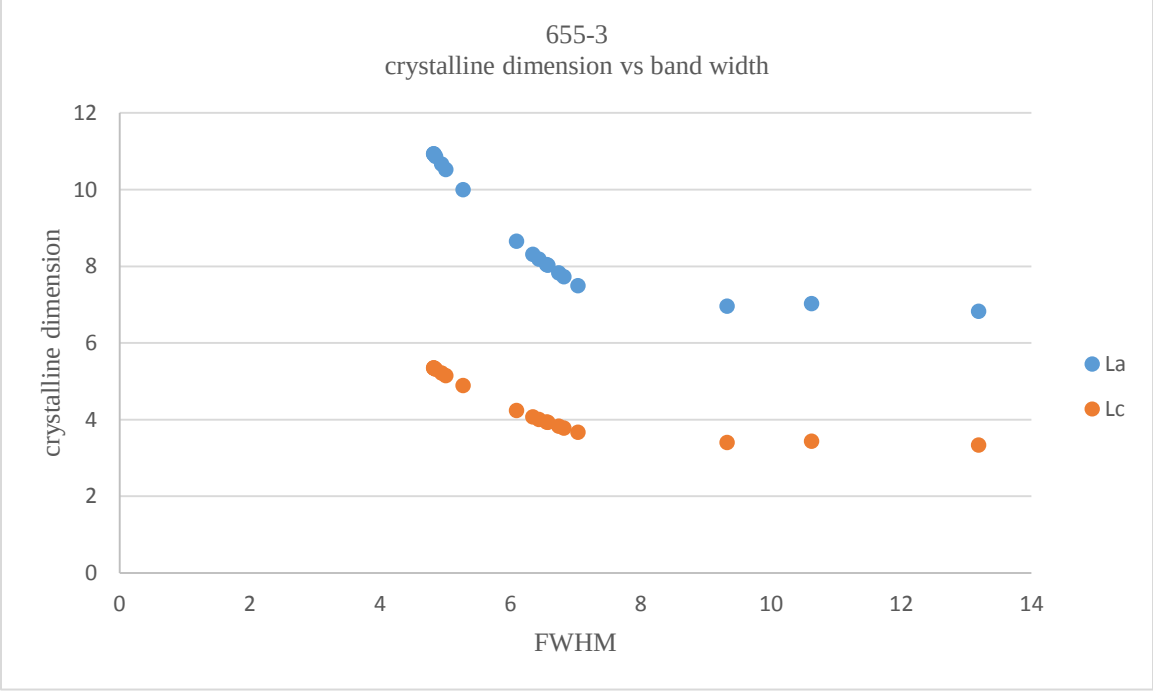

Figure 0-58: Crystalline Dimension Vs FWHM for Sample 655-3.

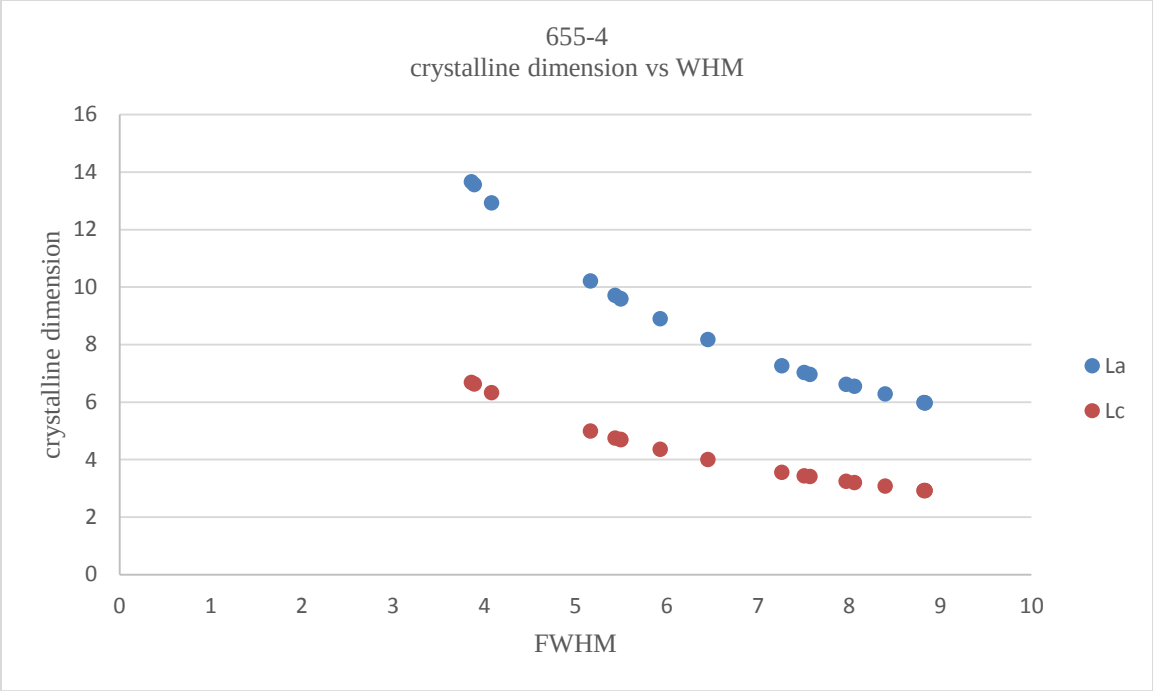

Figure 0-59: Crystalline Dimension Vs FWHM for Sample 655-4.

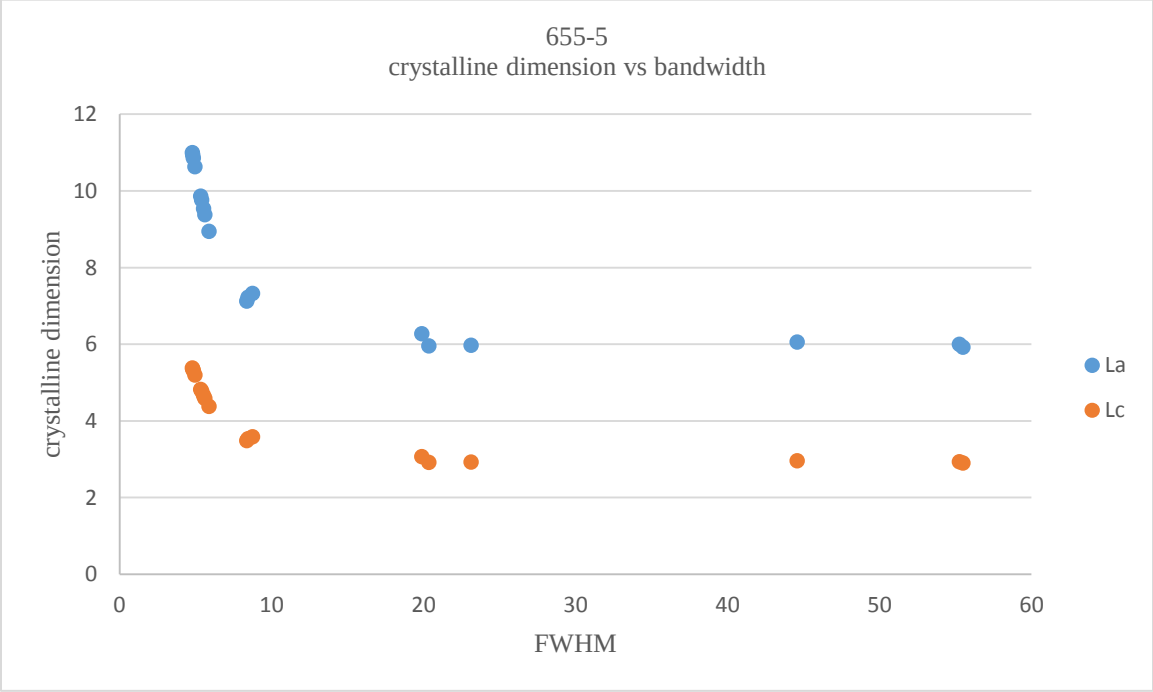

Figure 0-60: Crystalline Dimension Vs FWHM for Sample 655-5.

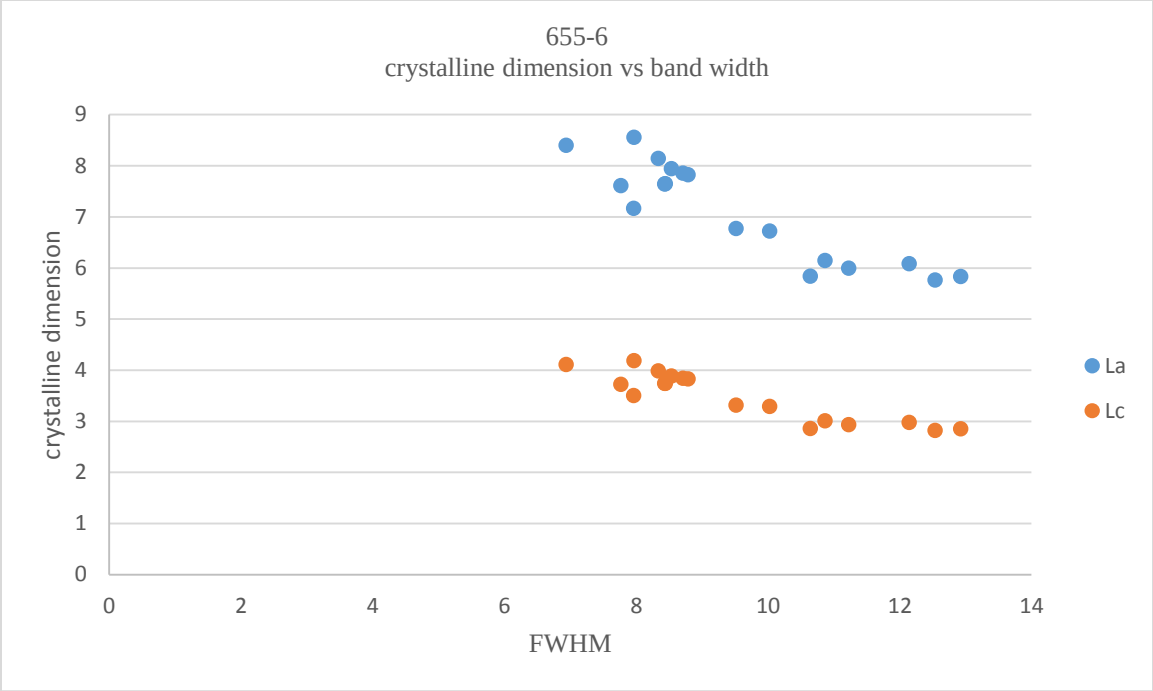

Figure 0-61: Crystalline Dimension Vs FWHM for Sample 655-6.

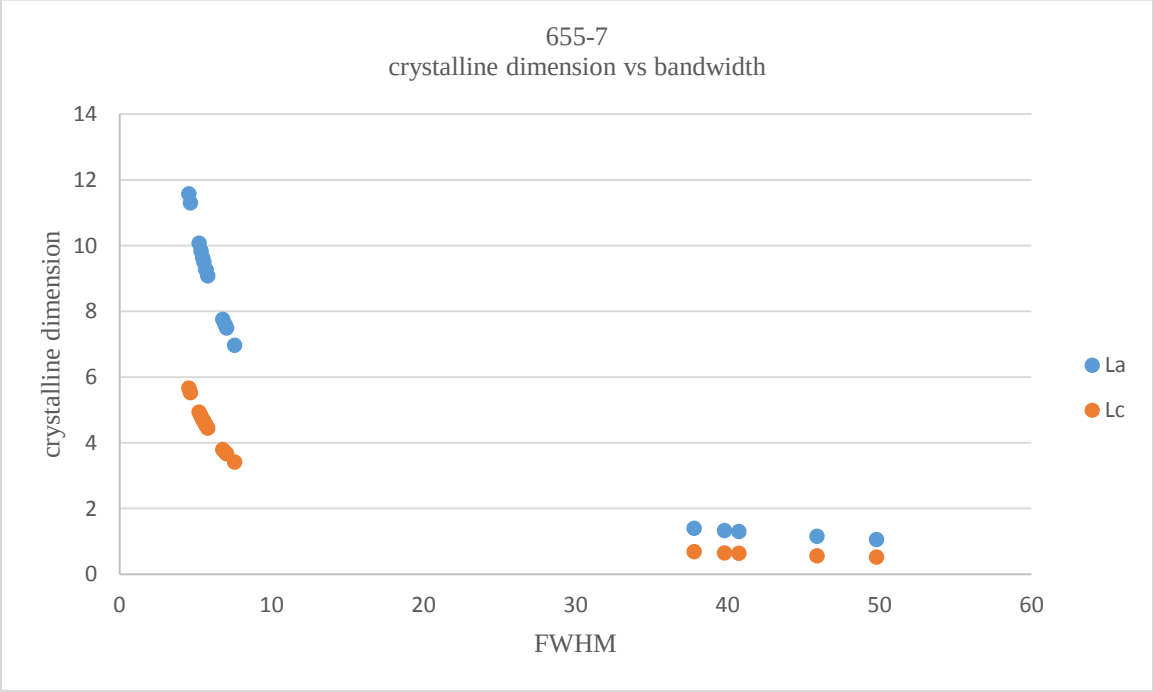

Figure 0-62: Crystalline Dimension Vs FWHM for Sample 655-7.

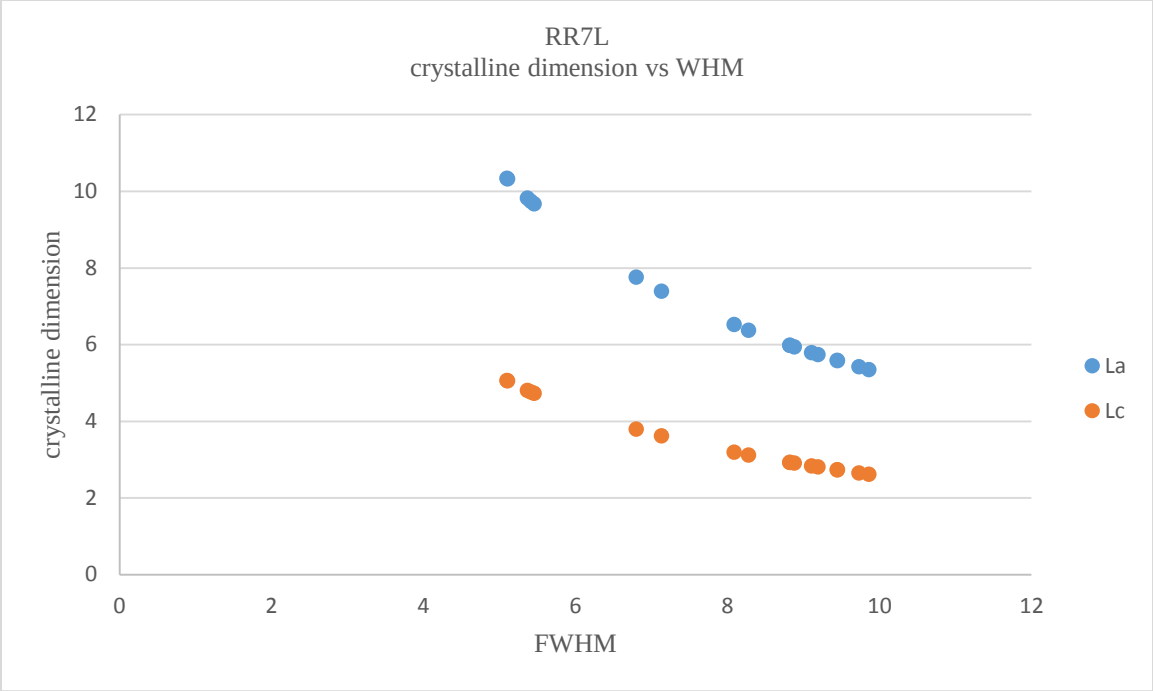

Figure 0-63: Crystalline Dimension Vs FWHM for Sample RR7L.

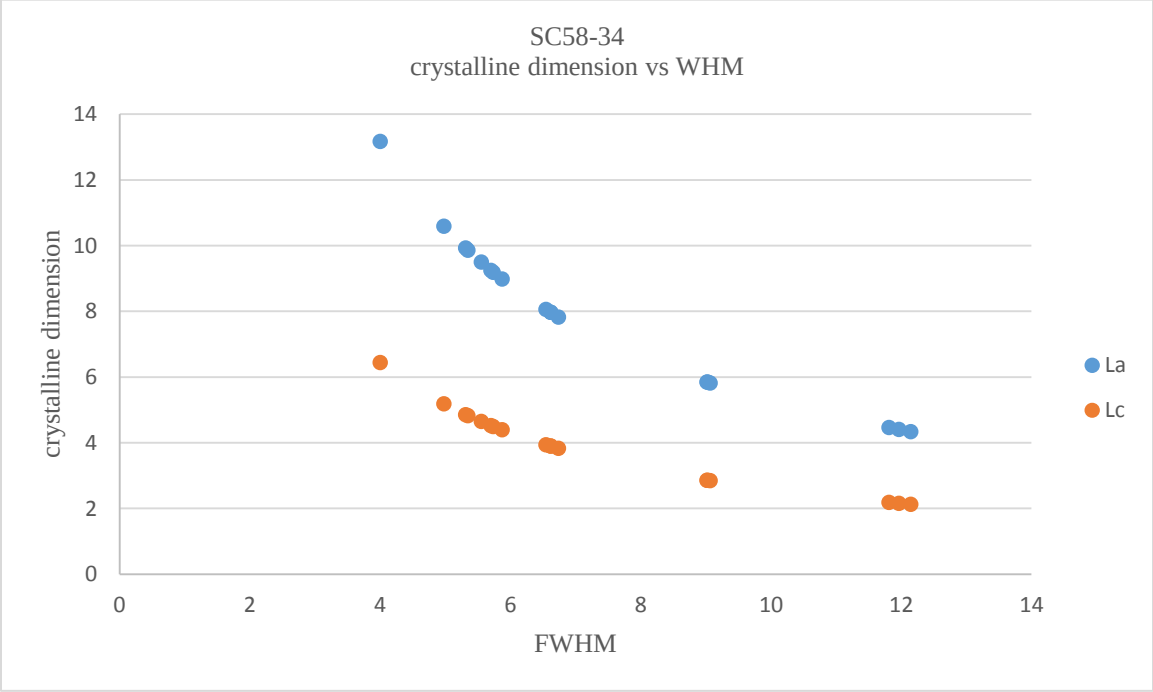

Figure 0-64: Crystalline Dimension Vs FWHM for Sample SC58-34.

Mathematica Code

655-6 age1w Sample:

```
ClearAll;
Remove["Global`*"];

data = Import[
   "C:\\Users\\IBRAHIM\\Desktop\\Mathimatica\\Hekma\\Data\\655-6age1w.txt", "Table"];


FullDataLenght = Length[data]
```

10 502

```
FullData = Table[data[[i]] , {i, 2, FullDataLenght}];

RangedData = Table[data[[i]], {i, 2, FullDataLenght / 3, 10}];
RangedDataLenght = Length[RangedData]
```

350

```
FullDataPlot =
 ListPlot[FullData, PlotRange → All, AxesOrigin → {0, 0}, PlotStyle → {Thick, Red}]
```

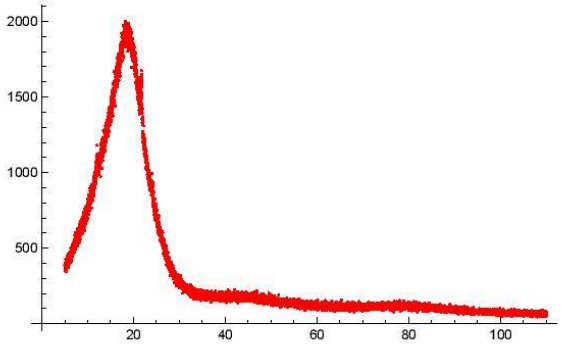

```
RangedDataPlot =
 ListPlot[RangedData, PlotRange → All, AxesOrigin → {0, 0}, PlotStyle → {Thick, Red}]
```

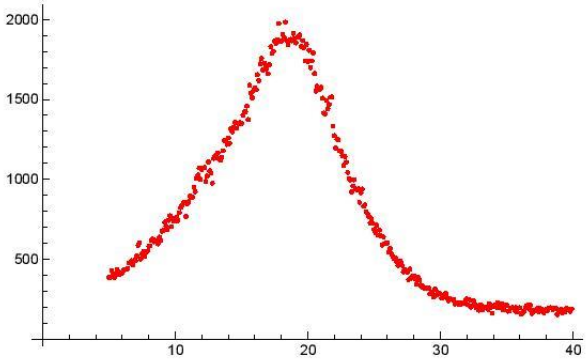

■ -Fit Curve Using Generalized Fermi Function(GFF)

```
(*Manipulate[Plot[A1/(e^(-a1(s-c1))+e^(b1(s-c1)))+A2/(e^(-a2(s-c2))+e^(b2(s-c2)))+d,{s,5,35}],{A1,0,500},{a1,0,1},
 {b1,0,1},{c1,0,50},{A2,0,500},{a2,0,1},{b2,0,1},{c2,0,50}, {d,0,50}]*)
```

```
GFF = FindFit[RangedData, A1/(e^(-a1 (s-c1)) + e^(b1 (s-c1))) + A2/(e^(-a2 (s-c2)) + e^(b2 (s-c2))) + a1 - d s, {{A1, 450},
   {a1, 0.2}, {b1, 0.4}, {c1, 18}, {A2, 250}, {a2, 0.15}, {b2, 0.4}, {c2, 28}, {d, 30}}, s]
```

... FindFit: The step size in the search has become less than the tolerance prescribed by the PrecisionGoal option, but the gradient is larger than the tolerance specified by the AccuracyGoal option. There is a possibility that the method has stalled at a point that is not a local minimum.

```
{A1 → 1984.96, a1 → -0.326257, b1 → -0.129, c1 → 21.8166,
 A2 → 1160.13, a2 → -0.77959, b2 → -0.140694, c2 → 20.0857, d → -4.59476}
```

⋮

⋮

```
FitCurve = Plot[ReplaceAll[A1/(e^(-a1 (s-c1)) + e^(b1 (s-c1))) + A2/(e^(-a2 (s-c2)) + e^(b2 (s-c2))) + a1 - d s, GFF],
  {s, 5, 35}, PlotRange → All, PlotStyle → {Thick, Green}]
```

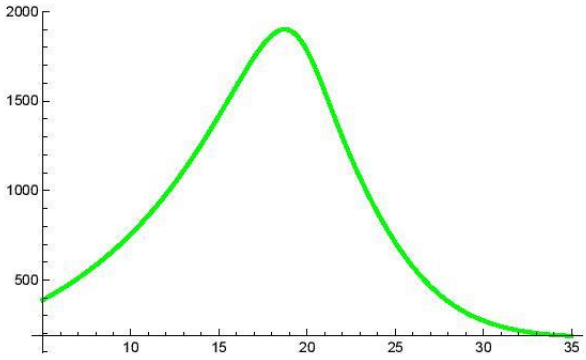


```
Show[RangedDataPlot, FitCurve]
```

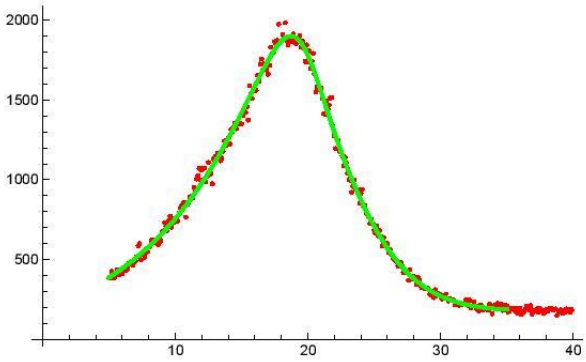


```
Show[FullDataPlot, FitCurve]
```

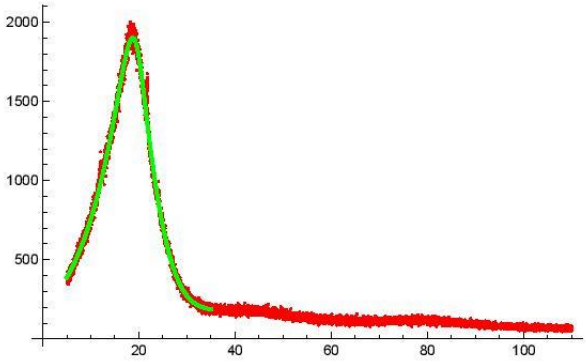

```
PeaksFit1 = Plot[{ReplaceAll[A1/(e^(-a1 (s-c1)) + e^(b1 (s-c1))), GFF],
   ReplaceAll[A2/(e^(-a2 (s-c2)) + e^(b2 (s-c2))), GFF], ReplaceAll[a1 - d s, GFF]}, {s, 5, 35},
  PlotRange → All, PlotStyle → {{Thick, Blue}, {Thick, Yellow}, {Thick, Brown}}]
```

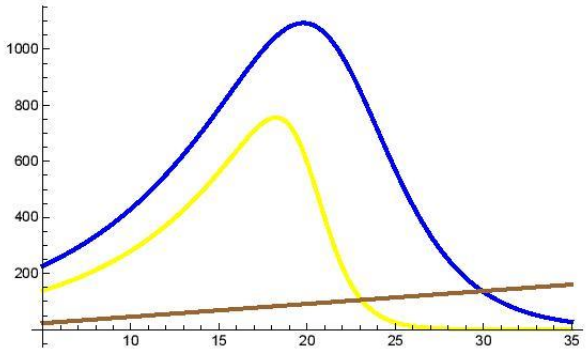


```
FinalGFF =
 FindFit[RangedData, A1/(e^(-a1 (s-c1)) + e^(b1 (s-c1))) + A2/(e^(-a2 (s-c2)) + e^(b2 (s-c2))) + a1 - d s, {{A1, 450},
   {a1, 0.2}, {b1, 0.4}, {c1, 18}, {A2, 250}, {a2, 0.15}, {b2, 0.4}, {c2, 28}, {d, 30}}, s]
```

... FindFit: The step size in the search has become less than the tolerance prescribed by the PrecisionGoal option, but the gradient is larger than the tolerance specified by the AccuracyGoal option. There is a possibility that the method has stalled at a point that is not a local minimum.

```
{A1 → 1984.96, a1 → -0.326257, b1 → -0.129, c1 → 21.8166,
 A2 → 1160.13, a2 → -0.77959, b2 → -0.140694, c2 → 20.0857, d → -4.59476}
```

```
FitCurveFinal =
 Plot[ReplaceAll[A1/(e^(-a1 (s-c1)) + e^(b1 (s-c1))) + A2/(e^(-a2 (s-c2)) + e^(b2 (s-c2))) + a1 - d s, FinalGFF],
  {s, 5, 35}, PlotRange → All, PlotStyle → {Thick, Green}]
```

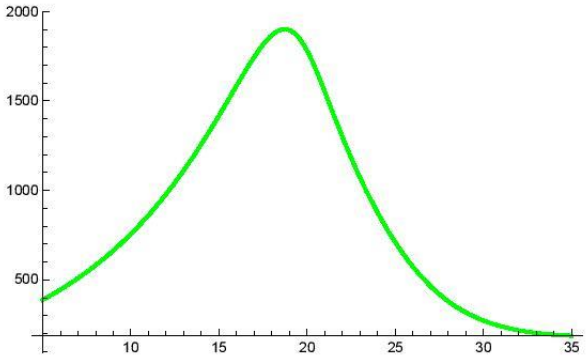

```
Show[RangedDataPlot, FitCurveFinal]
```

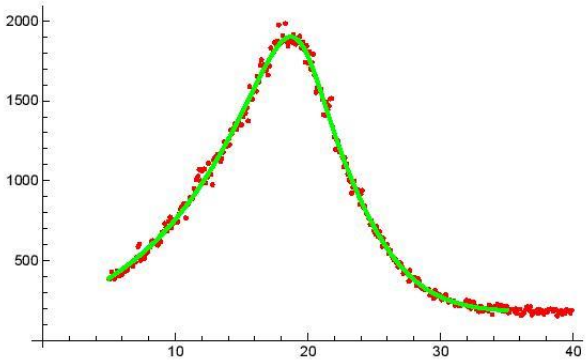


```
PeaksFit = Plot[{ReplaceAll[A1/(e^(-a1 (s-c1)) + e^(b1 (s-c1))), FinalGFF],
  ReplaceAll[A2/(e^(-a2 (s-c2)) + e^(b2 (s-c2)))^2, FinalGFF], ReplaceAll[{a1 - d s}, FinalGFF]},
 {s, 5, 35}, PlotRange → All, PlotStyle → {{Thick, Blue}, {Thick, Yellow}, {Thick, Brown}}]
```

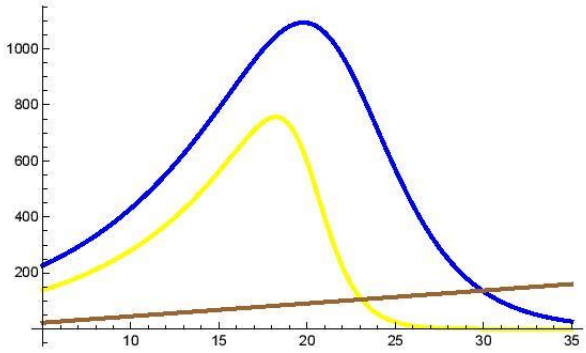


```
Show[RangedDataPlot, FitCurveFinal, PeaksFit]
```

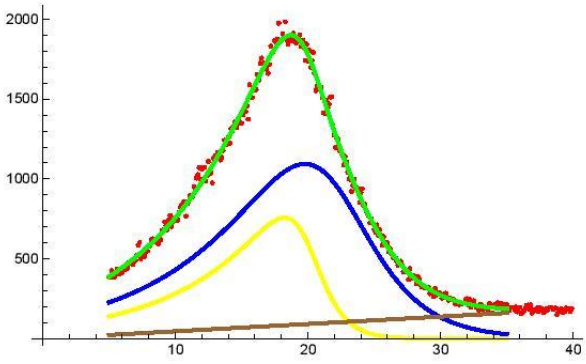

```
nlm = NonlinearModelFit[RangedData,
  A1/(e^(-a1 (s-c1)) + e^(b1 (s-c1))) + A2/(e^(-a2 (s-c2)) + e^(b2 (s-c2))) + a1 - d s, {{A1, 450}, {a1, 0.2},
  {b1, 0.4}, {c1, 18}, {A2, 250}, {a2, 0.15}, {b2, 0.4}, {c2, 28}, {d, 30}}, s]
```

... NonlinearModelFit: The step size in the search has become less than the tolerance prescribed by the PrecisionGoal option, but the gradient is larger than the tolerance specified by the AccuracyGoal option. There is a possibility that the method has stalled at a point that is not a local minimum.

```
FittedModel[
```

$$-0.326257+\frac{1984.96}{e^{-0.129\,(-21.8166+s)}+e^{0.326257\,(\ll 1\gg)}}+\frac{1160.13}{e^{-0.140694\,(\ll 1\gg)}+e^{\ll 19\gg\,(\ll 1\gg)}}+4.59476\,s$$

```
]
```

```
Show[Plot[nlm[s], {s, 5, 35}, PlotRange → All, PlotStyle → Red],
 ListPlot[RangedData, PlotMarkers → {Style[◆, Black], 5}]]
```

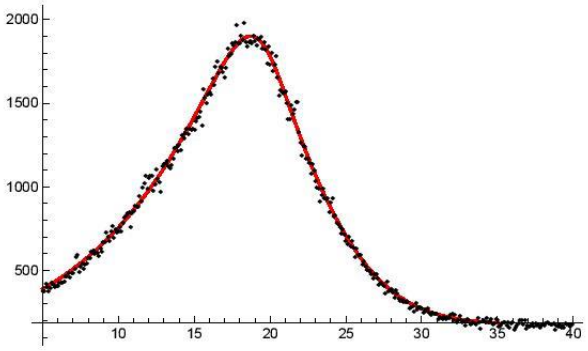


```
Normal[nlm]
```

$$-0.326257+\frac{1984.96}{e^{-0.129\,(-21.8166+s)}+e^{0.326257\,(-21.8166+s)}}+\frac{1160.13}{e^{-0.140694\,(-20.0857+s)}+e^{0.77959\,(-20.0857+s)}}+4.59476\,s$$

```
bestfitParm = nlm["BestFitParameters"]
```

```
{A1 → 1984.96, a1 → -0.326257, b1 → -0.129, c1 → 21.8166,
 A2 → 1160.13, a2 → -0.77959, b2 → -0.140694, c2 → 20.0857, d → -4.59476}
```

```
nlm["ParameterConfidenceIntervalTable", ConfidenceLevel → 0.99]
```

	Estimate	Standard Error	Confidence Interval
A1	1984.96	762.159	{10.7255, 3959.2}
a1	−0.326257	0.0121025	{−0.357607, −0.294908}
b1	−0.129	0.132996	{−0.473503, 0.215504}
c1	21.8166	1.21404	{18.6719, 24.9614}
A2	1160.13	835.136	{−1003.14, 3323.4}
a2	−0.77959	0.197947	{−1.29234, −0.266842}
b2	−0.140694	0.250927	{−0.790677, 0.509289}
c2	20.0857	0.781183	{18.0622, 22.1092}
d	−4.59476	0.148183	{−4.97861, −4.21092}

```
nlm["ParameterTable"]
```

	Estimate	Standard Error	t-Statistic	P-Value
A1	1984.96	762.159	2.6044	0.00960634
a1	−0.326257	0.0121025	−26.9578	1.58752×10^{-86}
b1	−0.129	0.132996	−0.96995	0.332759
c1	21.8166	1.21404	17.9702	2.83971×10^{-51}
A2	1160.13	835.136	1.38915	0.165693
a2	−0.77959	0.197947	−3.93837	0.000099498
b2	−0.140694	0.250927	−0.560697	0.575372
c2	20.0857	0.781183	25.7119	8.02145×10^{-82}
d	−4.59476	0.148183	−31.0074	2.93817×10^{-101}

```
resi = nlm["FitResiduals"];
ListPlot[resi, Filling → Axis]
```

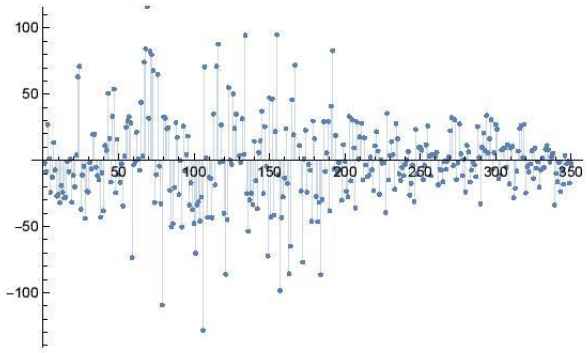


```
resiData = Table[{FullData[[i, 1]], resi[[i]]}, {i, 1, RangedDataLenght}];
```

```
resiplot = ListPlot[resiData, PlotRange → All, PlotStyle → {Thick, Gray}]
```

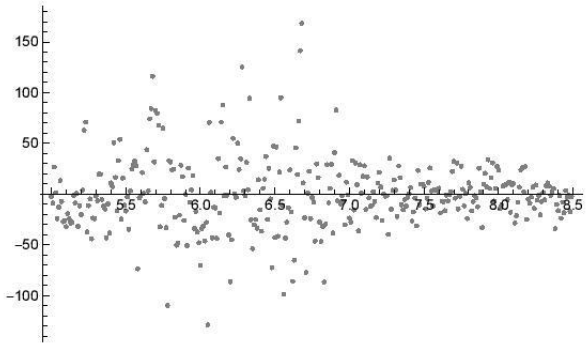

■ -Finding FHWM:

```
bestfitParm = nlm["BestFitParameters"]
```

```
{A1 → 1984.96, a1 → -0.326257, b1 → -0.129, c1 → 21.8166,
 A2 → 1160.13, a2 → -0.77959, b2 → -0.140694, c2 → 20.0857, d → -4.59476}
```

```
A1 = A1 /. bestfitParm; a1 = a1 /. bestfitParm; b1 = b1 /. bestfitParm; c1 = c1 /. bestfitParm;
A2 = A2 /. bestfitParm; a2 = a2 /. bestfitParm; b2 = b2 /. bestfitParm; c2 = c2 /. bestfitParm;
d = d /. bestfitParm;
```

```
ypeak = nlm[s] /. First@Quiet[FindRoot[D[nlm[s], s] == 0, {s, 20}]]
```

```
1900.93
```

$$\text{TwoTheta} = \text{FindMaximum}\left[\frac{A1}{e^{-a1\,(s-c1)} + e^{b1\,(s-c1)}} + \frac{A2}{\left(e^{-a2\,(s-c2)} + e^{b2\,(s-c2)}\right)} + a1 - d\,s,\ \{s, 20\}\right]$$

```
{1900.93, {s → 18.7195}}
```

```
hmw = ypeak + ((A1 /. bestfitParm) - ypeak) / 2
```

```
1942.94
```

```
right = FindRoot[nlm[s] == hmw, {s, 20}]
```

... FindRoot: The line search decreased the step size to within tolerance specified by AccuracyGoal and PrecisionGoal but was unable to find a sufficient decrease in the merit function. You may need more than MachinePrecision digits of working precision to meet these tolerances.

```
{s → 18.7195}
```

```
xr = s /. right
```

```
18.7195
```

```
left = FindRoot[nlm[s] == hmw, {s, 5}]
```

... FindRoot: The line search decreased the step size to within tolerance specified by AccuracyGoal and PrecisionGoal but was unable to find a sufficient decrease in the merit function. You may need more than MachinePrecision digits of working precision to meet these tolerances.

```
{s → 18.7195}
```

```
xl = s /. left
```

```
18.7195
```

```
FWHM = xr - xl
```

$$1.69228 \times 10^{-7}$$

```
Show[Plot[nlm[s], {s, 5, 35}, PlotRange → All, PlotStyle → Red,
  Epilog → {Green, PointSize[0.02], Point[{#, nlm@#} & /@ {xl, xr}]},
  GridLines → {{xl, xr}, {A1 /. bestfitParm, hmw, ypeak}},
  GridLinesStyle → Directive[Gray, Dashed]],
 ListPlot[{nlm /. FinalGFF}, PlotMarkers → {Style[◆, Black], 5}]]
```

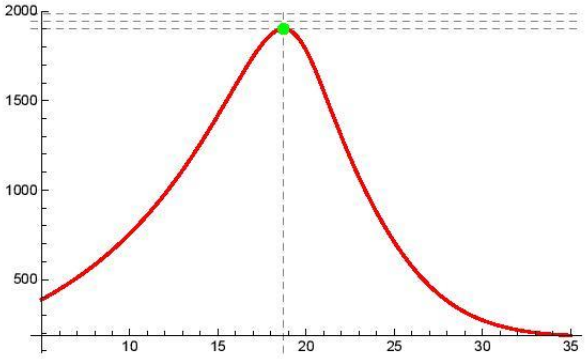

■ -Finding FWHM FOR FIRST COMPONENT:

```
ypeak1 = A1/(e^(-a1 (s-c1)) + e^(b1 (s-c1))) /. First@Quiet[FindRoot[D[A1/(e^(-a1 (s-c1)) + e^(b1 (s-c1))), {s, 1}] == 0, {s, 20}]]
```

```
1093.63
```

```
TwoTheta1 = FindMaximum [A1/(e^(-a1 (s-c1)) + e^(b1 (s-c1))), s]
```

```
{1093.63, {s → 19.7785}}
```

```
hmw1 = ypeak1 + (a1 - ypeak1) / 2
```

```
546.653
```

```
{xl1, xr1} = s /. NSolve[A1 / (e^(-a1 (s-c1)) + e^(b1 (s-c1))) == hmw1, s, Reals]
```

```
{11.9047, 25.1654}
```

```
FWHM1 = xr1 - xl1
```

```
13.2606
```

```
Show[Plot[A1 / (e^(-a1 (s-c1)) + e^(b1 (s-c1))), {s, 5, 35},
  PlotRange → All, PlotStyle → Blue, Epilog → {Green, PointSize[0.02]},
  GridLines → {{xl1, xr1}, {a1, hmw1, ypeak1}}, GridLinesStyle → Directive[Gray, Dashed]],
 ListPlot[{Plot[ReplaceAll[A1 / (e^(-a1 (s-c1)) + e^(b1 (s-c1))), FinalGFF], {s, 5, 35}]},
  PlotMarkers → {Style[◆, Black], 5}]]
```

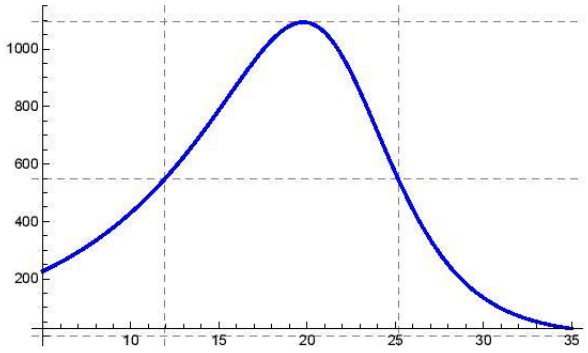

■ -Finding FWHM FOR 2nd COMPONENT:

```
ypeak2 =
 A2 / (e^(-a2 (s-c2)) + e^(b2 (s-c2))) /. First@Quiet[FindRoot[D[A2 / (e^(-a2 (s-c2)) + e^(b2 (s-c2))), s] == 0, {s, 18}]]
```

```
756.432
```

```
TwoTheta2 = FindMaximum[A2 / (e^(-a2 (s-c2)) + e^(b2 (s-c2))), {s, 5}]
```

```
{756.432, {s → 18.2252}}
```

```
hmw2 = ypeak2 + (a2 - ypeak2) / 2
```

```
377.826
```

```
{xl2, xr2} = s /. NSolve[A2 / (e^(-a2 (s-c2)) + e^(b2 (s-c2))) == hmw2, s, Reals]
```

```
{12.1166, 21.099}
```

```
FWHM2 = xr2 - xl2
```

```
8.98242
```

```
Show[Plot[A2/(e^(-a2 (s-c2)) + e^(b2 (s-c2))), {s, 5, 35},
  PlotRange → All, PlotStyle → Blue, Epilog → {Green, PointSize[0.02]},
  GridLines → {{xl2, xr2}, {a2, hmw2, ypeak2}}, GridLinesStyle → Directive[Gray, Dashed]],
 ListPlot[{Plot[ReplaceAll[A2/(e^(-a2 (s-c2)) + e^(b2 (s-c2))), FinalGFF], {s, 5, 35}]},
  PlotMarkers → {Style[◆, Black], 5}]]
```

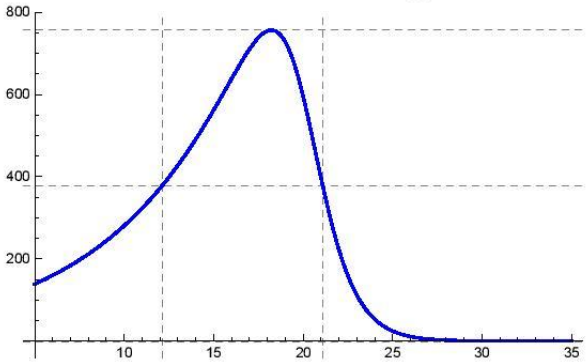

■ -Finding CURVE AREA:

$$\text{Atotal} = \int_5^{35} \left\{ \frac{A1}{e^{-a1\,(s-c1)} + e^{b1\,(s-c1)}} + \frac{A2}{\left(e^{-a2\,(s-c2)} + e^{b2\,(s-c2)}\right)} + a1 - d\,s \right\} ds$$

```
{26115.6}
```

$$A_{\gamma} = \int_5^{35} \frac{A1}{e^{-a1\,(s-c1)} + e^{b1\,(s-c1)}}\, ds$$

```
15784.3
```

$$Ag = \int_5^{35} \frac{A2}{\left(e^{-a2\,(s-c2)} + e^{b2\,(s-c2)}\right)}\, ds$$

```
7584.19
```

```
Grid[{{$Atotal, $Aɣ, $Ag, $FWHM, $FWHM1, $FWHM2, $TwoTheta, $TwoTheta1, $TwoTheta2},
  {Atotal, Aɣ, Ag, FWHM, FWHM1, FWHM2, TwoTheta, TwoTheta1, TwoTheta2}}, Frame → All]
```

$Atotal	$Aɣ	$Ag	$FWHM	$FWHM1	$FWHM2	$TwoTheta	$TwoTheta1	$TwoTheta2
{26115.6}	15784.3	7584.19	1.69228×10^{-7}	13.2606	8.98242	{1900.93, {s → 18.71`95}}	{1093.63, {s → 19.77`85}}	{756.432, {s → 18.22`52}}